

A Multi-Scale Approach to Understanding CO₂-Solvent Systems for the Development of CO₂ Capture Technologies

Submitted in partial fulfillment of the requirements for

the degree of

Doctor of Philosophy

Department of Chemical Engineering

Anita S. Lee

B.S., Chemical Engineering, University of Arizona

B.S., Mathematics, University of Arizona

Carnegie Mellon University
Pittsburgh, Pennsylvania

May, 2013

Acknowledgments

This work is the end of a journey that started much longer than 5 years ago. I cannot help but look back at the numerous of individuals that have influenced me as role models, guided me as mentors, and cared and supported me as family.

First and foremost, I would like to thank my parents for their continual support. When it came to something I needed, regardless of how financially difficult it may have been, the answer was always Yes. It was not until I became an adult and started to understand the world did I realize the gravity of their sacrifices as Chinese immigrants working long odd hours to provide and care for their family.

I thank my friends, especially the group of girls I met in college that have truly turned into lifelong sisters. I value their friendship, acceptance of all my quirks, and the hours of endless laughter and joy they have brought to my life. To the friends I have made in Pittsburgh, I thank them for making my time in Pittsburgh some of the best years in my life. I fully expected to navigate the tides of graduate school alone, but instead experienced the exact opposite. I could not have asked for a better group of people to share this experience with. I look forward to sharing in all of their success and the many reunions I know we will have.

To Ethan, you were a kind face on the cold January day when I started at CMU. Thank you for that first smile and everything that it has become. I have learned so much about myself through our relationship and your support and belief in what I can be pushed me over the hurdles of graduate school.

Lastly, I would like to thank my thesis advisor John Kitchin. He has many qualities of a great advisor, but the ones that have impacted me the most his willingness to listen and evolve. The beginnings of my graduate work were

rough and I would have never made it to other side, a place where I both am proud of and enjoy my work, without his support and desire to find a better fit for me. To my previous group-mates, James, Spencer, Nilay, Robin, and Rich, thank-you for listening and helping a young research get off the ground.

The generosity of many has made my academic career possible. Thank you the Flinn Foundation for the continual support of Arizona education. If not for the financial burdens of college relived by the Flinn scholarship and the academic freedom that was encouraged by the Flinn community, I would have never found chemical engineering and that changed my life. Thank you to The National Energy Technology Laboratory for the continual financial support throughout my PhD and the Steinbrenner Institute for their generous support of academic research at CMU through the Steinbrenner Fellowship. Additionally, I thank my thesis committee: John Kitchin (chair), Neil Donahue, Nick Sahinidis, and Ed Rubin for their support, useful conversations, and time that have contributed to the review of this work.

Abstract

CO₂ capture from a coal-fired power plant is a difficult problem that is costly due to the high energy demands of the process. Given the existing and well-understood processes for pre-combustion CO₂ removal through physical absorption and post-combustion flue gas acid gas treating, developing new solvents with lower energy demands has potential to reduce CO₂ capture costs of these processes. In this work, we use analytical and computational techniques to understanding of CO₂-solvent systems at a molecular and process scale. This multi-scale understanding of solvent-CO₂ systems will guide the design of new solvents for low cost CO₂ capture.

At the molecular level, CO₂-solvent interactions were studied to understand the role of the solvent and identify solvent molecular properties that could be used as descriptors and/or tuning parameters of the interactions. A Density Functional Theory study of CO₂-amine solvents for post-combustion capture showed the reaction energy to form bicarbonate and carbamate products were stabilized for amines functionalized with electron donating groups and destabilized with electron withdrawing groups. Additionally, amine electronegativity was determined to be a good descriptor of the amine-bicarbonate reaction energy, which could be tuned with the choice of functional group and degree of amine functionalization. CO₂ interactions with pre-combustion capture physical solvents, hydrophobic CO₂-philic oligomers and 1-alkyl-3-methylimidazolium based ionic liquids, were characterized using Raman spectroscopy. Additionally, a technique to quantify solubility of CO₂ in physical solvents using the Raman spectra was developed and showed CO₂ solubility to correlate with molecular weight of the solvent.

Aspen Plus simulations coupled with a genetic algorithm were used to understand the potential impact of solvent selection on the post-combustion CO₂ capture process by modeling a 90% CO₂ capture process using MEA, DEA, and AMP. This analysis evaluated and equitably compared the process performance of post-combustion capture solvents and showed the trade-offs between lower energy demands and capital cost of the process and by comparison DEA could achieve 90% capture from a coal-fired power plant with lowest capital cost and highest net power output from the plant. A similar analysis could be performed with the pre-combustion capture process to assess and compare the performance those solvents.

Contents

Abstract	iv
List of Tables	viii
List of Figures	ix
1 Introduction	1
1.1 The Need for CO ₂ Capture For Coal Fired Power Plants . . .	1
1.2 Thesis Objectives	3
2 An Overview of the Post-Combustion CO₂ Capture Process Using Amine Solvents	5
2.1 The Post-Combustion CO ₂ Capture Process	5
2.2 Amine-CO ₂ Chemistry	8
3 A Density Functional Theory Study of Amine Molecular and Electronic Structure Connections To Amine-CO₂ Reactivity	10
3.1 Introduction	10
3.2 Materials and Methods	13
3.2.1 Density Functional Theory and Reaction Energy Calculations	15
3.2.2 Theory of DFT Based Chemical Reactivity Descriptors	21
3.3 Results	24
3.4 Conclusion	39
4 What Is the Impact of Solvent Selection? A Multi-objective Analysis of the Post-Combustion CO₂ Capture Process Using MEA, DEA, and AMP	41
4.1 Introduction	41
4.2 Materials and Methods	45
4.2.1 Process Simulation and Optimization Information Flow	45
4.2.2 Aspen Plus Process Models	45
4.2.3 Process Performance Parameters	49
4.2.4 Multi-objective Genetic Algorithm Analysis	50
4.3 Results and Discussion	51
4.3.1 Analysis of the MEA Process	51
4.3.2 The Effect of Solvent Selection	54
4.4 Conclusion	61
5 An Overview of Pre-combustion CO₂ Capture Using Physical Solvents	63
5.1 Process Overview	63
5.2 Advancements of Physical Solvents for Pre-combustion CO ₂ Capture	66

6	Characterization of CO₂-Physical Solvent Systems Using Raman Spectroscopy	68
6.1	Introduction	68
6.2	Materials and Methods	70
6.2.1	Materials	70
6.2.2	Experimental Apparatus for Raman Spectroscopy Measurements of High Pressure Gas-Solvent Systems .	73
6.2.3	Overview of Raman Spectroscopy	76
6.2.4	Experimental Procedure for Raman Spectroscopy Measurements of the Gas and Liquid Phase	78
6.2.5	Data Analysis of the CO ₂ Peak	81
6.3	Results	82
6.3.1	Raman Spectra of Gas Phase CO ₂	82
6.3.2	Raman Spectra of CO ₂ -Oligomer Solvent Systems . . .	83
6.3.3	Raman Spectra of CO ₂ -Solvent-Ionic liquids	87
6.3.4	Analysis of Solvated CO ₂ Spectra	90
6.3.5	Measuring Solubility of CO ₂ in Physical Solvents Using Raman Spectra	95
6.4	Conclusions	102
7	Conclusions	104
7.1	A Molecular Understanding of CO ₂ -Amine Interactions for Post-Combustion Capture From Density Functional Theory . .	105
7.2	Understanding the Impact of Solvent Selection on the Post-Combustion CO ₂ Capture Process	106
7.3	A Molecular Understanding of CO ₂ -Physical Solvent Interactions From Raman Spectroscopy	107
	References	109
	Appendix A Aspen Flow Sheets	121
	Appendix B Raman Spectra of CO₂-Solvent Systems	123
B.1	Oligomers	123
B.2	Ionic Liquids	126

List of Tables

1.1	CO ₂ emissions targets by country as reported in Appendix I and II of the 2010 Copenhagen Accord.(Source: unfccc.int/meetings/copenhagen_dec_2009/items/5264.php) Emission data provided by the World Bank. ¹	1
4.1	Flue gas inlet conditions used for multi-objective post-combustion capture process models.	47
4.2	Equipment and process operating optimization variables . . .	51
4.3	Best solutions meeting individual design objectives using MEA in the post-combustion CO ₂ capture process. Case 1: Maximum power output, Case 2: Minimum capital cost.	54
4.4	Single Aspen Plus process model evaluations of MEA, DEA, and AMP post-combustion CO ₂ capture process using equipment and process design specification of Case 1.	55
6.1	k_H^{cc} values for CO ₂ -philic oligomers and [C _n mim][Tf ₂ N] Ionic Liquids determined from analysis of Raman spectra of CO ₂ -solvent system. Error reported for 95% confidence intervals. .	101

List of Figures

2.1	Block diagram of pulverized coal plant with a post-combustion CO ₂ capture unit. Adapted from Rubin et al. ²	5
2.2	Simplified process flow digram of amine post-combustion CO ₂ capture process.	6
2.3	Simplified process flow diagram of CO ₂ compression process.	7
3.1	Alkylamines considered in DFT study of amine-CO ₂ reactivity.	13
3.2	Alkanolamines considered in DFT study of amine-CO ₂ reactivity.	14
3.3	Trifluoroalkylamines considered in DFT study of amine-CO ₂ reactivity.	14
3.4	Thermodynamic pathway of amine-CO ₂ reaction showing the relationship between the overall reaction and the solvent phase reaction.	16
3.5	Reactions considered in this work along the bicarbonate pathway.	18
3.6	Reaction along the carbamate pathway considered in this study.	19
3.7	Lowest energy conformation search of MEA.	20
3.8	Lowest energy conformation search of tripropanolamine.	20
3.9	Reaction pathway diagrams showing the relative enthalpy (compared to enthalpy of reactants) of product states considered for the bicarbonate (a) and carbamate (b) pathway. Results for NH ₃ are shown in black (—) and results for MEA are shown in red (—).	26
3.10	Reaction energy of amine-bicarbonate complex, Reaction 2 (gray area), and amine-carbamate complex, Reaction 6, formation for primary (1°), secondary (2°), and tertiary (3°) alkylamines (a) and trifluoroalkylamines (b). The reaction energy to form the respective product formation with NH ₃ is denoted by the dashed line.	28
3.11	Reaction energy of amine-bicarbonate, Reaction 2 (shaded in gray), and amine-carbamate, Reaction 6, complex formation for primary (1°), secondary (2°), and tertiary (3°) alkanolamines without effects of intermolecular hydrogen bonding(a) and alkanolamines including intermolecular hydrogen bonding (b). The reaction energy to form the respective product formation for NH ₃ is denoted by the dashed line	30
3.12	Amine-bicarbonate complex reaction energy as a function of the difference in the electronegativity of the amine reactant and carbonic acid.	31

3.13	The amine-bicarbonate complex reaction energy as a function of the difference in the electronegativity of the amine reactant and carbonic acid for the lowest energy amine reactant conformation (gray) and conformations within 0.1 eV of the lowest energy conformation for tripropylamine (blue), tripropanolamine (red), and di-trifluoroethylamines (green).	32
3.14	Electronegativity of primary, secondary, and tertiary amines for the (A) alkylamines, (B) alkanolamines, and (C) trifluoroalkylamines groups calculated using Equation 3.11. . .	34
3.15	Correlation between amine-carbamate reaction energy and carbamic acid reaction energy.	35
3.16	The reaction energy for carbamic acid formation as a function of the localized softness of the amine nitrogen (s_N). The softness of the reacting carbon (s_O) on CO ₂ is 0.09 eV.	36
3.17	Trends in the localized softness on the amine nitrogen primary, secondary, and tertiary amines for (A) alkylamines, (B) alkanolamines, and (C) trifluoroalkylamines groups.	38
3.18	Molecular geometry descriptors of carbamic acid, O-C-O bond angle [°] (top) and N-C bond length [Å] (bottom) for (A) alkylamines, (B) alkanolamines, and (C) trifluoroalkylamines.	39
4.1	Information flow of modeFrontier, Excel, and Aspen Plus applications.	46
4.2	Solutions from genetic algorithm analysis for a post-combustion CO ₂ capture process using MEA solvent. Pareto front solutions are denoted as filled circles.	53
4.3	Solutions from genetic algorithm analysis for the post-combustion CO ₂ capture process using MEA, AMP, and DEA solvents. Pareto front solutions for each amine are denoted with filled symbols.	56
4.4	Reboiler heat duty [MW] versus net power output [MW] for Pareto front solutions from MEA, DEA, and AMP analysis. . .	57
4.5	Capital cost breakdown of Pareto front solutions for absorber, stripper, and CO ₂ compression units for the (A) MEA and (B) DEA CO ₂ capture process.	58
4.6	(A) Relationship between amine working capacity and total reboiler heat duty for Pareto front solutions of MEA, DEA, and AMP analysis. (B) Relationship between amine working capacity and process enthalpy component of reboiler heat duty (Equation 4.2) for Pareto front solution of MEA, DEA, and AMP analysis.	59
4.7	Experimentally measured heats of reaction and reaction rates for amine solvents. Adapted from Chowdhury et al.	60
5.1	Block diagram of IGCC process.	63

5.2	Process flow diagram of pre-combustion CO ₂ capture process using a pressure swing to regenerate the solvent. Adapted from Rubin et al. ²	65
6.1	Molecular structure of oligomer solvents studied in this work. .	71
6.2	Ionic liquid solvents studied in this work.	72
6.3	(A) Overhead view of high-pressure assembly: (1) Gas inlet valve (V1), (2) pressure sensor, (3) pressure release valve/vacuum line connection (V2), (4) solvent exposure valve (V3), (5) capillary. Inset figures show capillary filled with colored sample and fused end of capillary under 10X objective. (B) High pressure assembly positioned on motorized microscope stage.	74
6.4	Energy diagram of Rayleigh and Raman Scattering. Two types of Raman scattering can occur, either stokes or anti-stokes, and depend on the initial energy state of the system. Stokes scattering is the more common of the two, since systems are more likely to be in the ground state prior to excitation.	77
6.5	Raman and IR activity of the 3 vibrational modes of CO ₂ (bending mode is degenerate). Adapted from www.doitpoms.ac.uk/tlplib/raman/active_modes.php	78
6.6	Raman band of S-N-S stretch mode of [emim][Tf ₂ N] from z-position scan of sample in capillary. Inset figure: Absolute band intensity of S-N-S stretch mode as a function of z-position. . .	80
6.7	Raman spectra of CO ₂ gas at 2.5 to 30 bar and 295 K. The Fermi diad peaks are annotated at 1285 cm ⁻¹ (lower band) and 1388 cm ⁻¹ (upper band). The measured intensity, not normalized intensity, is displayed to illustrate the relationship between CO ₂ pressure and intensity.	83
6.8	Raman spectra of Selexol [®] at atmospheric conditions and equilibrium with 5 to 20 bar CO ₂ at 295 K. Arrows markers denote Fermi diad peaks of CO ₂	84
6.9	Raman spectra of PPGDME, MW 430, at atmospheric conditions and equilibrium with 5 to 40 bar CO ₂ at 295 K. . .	86
6.10	Raman spectra of PPGDME, MW 550, at atmospheric conditions and equilibrium with 5 to 40 bar CO ₂ at 295 K. . .	87
6.11	Raman spectra of [emim][Tf ₂ N] at atmospheric conditions and equilibrium with 5 to 40 bar CO ₂ at 295 K.	89
6.12	Raman spectra of Fermi diad peaks of solvated CO ₂ in Selexol [®] in equilibrium with 5 to 40 bar CO ₂ pressure. The arrow markers denote the position of the Fermi diad peaks in the 5 bar spectra. The position of the Fermi diad peaks of gas phase CO ₂ are indicated by the dashed lines.	91
6.13	Upper Fermi diad Raman peak position of symmetric stretch vibrational mode of solvated CO ₂ in oligomer solvents.	93

6.14	Upper Fermi diad Raman peak position of symmetric stretch vibrational mode of solvated CO ₂ in ILs.	94
6.15	Example of peak analysis to determine k_H^{cc} from Raman spectra using Selexol [®] . Each point plots the integrated area of the CO ₂ upper band in the solvent spectra vs. the CO ₂ upper band area in the gas spectra for an equilibrium CO ₂ pressure. The slope of this dataset is related to k_H^{cc} through Equation 6.7.	97
6.16	A comparison of Henrys law constants for octane and decane computed using vapor-liquid equilibrium data reported in literature over a range of temperatures and the Raman spectroscopy technique presented in this work. Octane: k_H from literature (\square), this work (∇)., Decane: k_H from literature(\circ), this work(∇).	100
6.17	k_H^{cc} for CO ₂ in different molecular weight PDMS and [C _n mim][Tf ₂ N] solvents.	102
A.1	Aspen flowsheet of post-combustion CO ₂ capture absorption tower model.	121
A.2	Aspen flowsheet of post-combustion CO ₂ capture amine regeneration tower model.	122
B.1	Raman spectra of PEGDME, MW 250, at atmospheric conditions and equilibrium with 5 to 40 bar CO ₂ at 295 K. . .	123
B.2	Raman spectra of PPGDME, MW 230, at atmospheric conditions and equilibrium with 5 to 40 bar CO ₂ at 295 K. . .	124
B.3	Raman spectra of PDMS, MW 1250, at atmospheric conditions and equilibrium with 5 to 40 bar CO ₂ at 295 K.	124
B.4	Raman spectra of PDMS, MW 2000, at atmospheric conditions and equilibrium with 5 to 40 bar CO ₂ at 295 K.	125
B.5	Raman spectra of [bmim][Tf ₂ N] at atmospheric conditions and equilibrium with 5 to 40 bar CO ₂ at 295 K.	126
B.6	Raman spectra of [hmim][Tf ₂ N] at atmospheric conditions and equilibrium with 5 to 40 bar CO ₂ at 295 K.	127
B.7	Raman spectra of [emim][TCB] at atmospheric conditions and equilibrium with 5 to 40 bar CO ₂ at 295 K.	127
B.8	Raman spectra of [emim][FAP] at atmospheric conditions and equilibrium with 5 to 40 bar CO ₂ at 295 K.	128
B.9	Raman spectra of [emim][BF ₄] at atmospheric conditions and equilibrium with 5 to 40 bar CO ₂ at 295 K.	128

1 Introduction

1.1 The Need for CO₂ Capture For Coal Fired Power Plants

Recognizing the connection between an increase in greenhouse gases present in the atmosphere and global climate change, social and political movements targeted at reducing the anthropogenic emissions of these gases have grown in the last decades. Many governments, emphasizing carbon dioxide (CO₂), the most abundant greenhouse gas, have set large CO₂ emissions reduction targets for 2020 (Table 1.1).

Country	Reduction Targets by 2020 (base year)	2009 CO ₂ Emissions [kt]	Base year CO ₂ Emissions [kt]
United States	17% (2005) ^a	5,299,563	5,826,394
China	40-45 (2005)%	7,687,114	5,790,017
European Union ^b	20%/30% ^c (2009)		
India			

Table 1.1: CO₂ emissions targets by country as reported in Appendix I and II of the 2010 Copenhagen Accord.(Source: unfccc.int/meetings/copenhagen_dec_2009/items/5264.php) Emission data provided by the World Bank.¹

Power generation accounts for 41% of the global CO₂ emission, predominately from the combustion of fossil fuels, leading this industry to be

^aContingent on passage of emissions legislation

^bMember States: Belgium, Bulgaria, Czech Republic, Denmark, Germany, Estonia, Ireland, Greece, Spain, France, Italy, Cyprus, Latvia, Lithuania, Luxembourg, Hungary, Malta, Netherlands, Austria, Poland, Portugal, Romania, Slovenia, Slovakia, Finland, Sweden, United Kingdom acting in common

^cdepends on adoption of reduction plan in developing world

a large target for CO₂ emissions reduction efforts.³ Power generation emissions could be reduced by decreasing energy consumption or transitioning to non-fossil fuel based power sources that do not have CO₂ as a byproduct. However, given the current supply and demand for energy, it is unrealistic to think that these efforts alone will be enough to address the scale of the CO₂ problem. Energy consumption has grown steadily as the world continues to develop and as progress continues energy demand will not decline. Additionally, non-fossil fuel power sources are expensive and only account for 9.2%^d of the global power portfolio.¹ In the near term it is not possible for the non-fossil fuel base power generation industry to grow substantially to affect large CO₂ emissions reductions. Due to these issues, and the low cost and prevalence of fossil fuels, in the near term fossil fuel power generation is unavoidable. Thus, in a carbon regulated environment, it is critical to develop carbon capture and sequestration (CCS) technologies that aim to control CO₂ emissions from fossil fuel power to the atmosphere by removing a concentrated CO₂ gas stream from industrial processes and sequestering the CO₂ in long term storage sites, i.e. underground aquifers or enhanced oil recovery operations. This would enable us to use our existing resources and energy infrastructure, while providing low CO₂ emissions power.

In 2010, 45% of the United States' electricity was produced from coal resources, which accounted for 32% of the nation's CO₂ emissions.^{4,5} To meet emissions goals while trying to limit the economic impact of CCS, the Department of Energy (DOE) has targeted technology development to capture 90% of CO₂ from power plants, with only a 30% increase to the cost

^dNuclear + alternative energy sources in 2010

of electricity. There are two commercially demonstrated technologies that could achieve this: post-combustion CO₂ capture and pre-combustion CO₂ capture.² Post-combustion CO₂ capture, the more advanced of the two processes, removes CO₂ from the flue gas stream of a traditional coal-fired power plant using an amine solvent scrubbing process. Pre-combustion CO₂ capture, also a solvent based technology, removes CO₂ from the syngas stream of an Integrated Gasification Combined Cycle (IGCC) power plant, a new advanced coal power generation technology. The syngas is at high pressure with a high partial pressure of CO₂, thus physical solvents are ideal for separating out the CO₂ from this stream.

Although there are some concerns regarding the ability to scale up both processes to CO₂ capture from an average power plant, 550 MW, the larger concern is the significant impact these processes are predicted to have on overall plant efficiency. In review of carbon capture technologies Rubin et al. show that in order to capture 90% CO₂ from these power plants, the cost of electricity from these plants will increase 60-80%.² The economic impact of increased cost of electricity is far reaching, thus it is imperative that the cost of CO₂ capture is reduced.

1.2 Thesis Objectives

Current research is focused in developing enhanced CO₂ capture process configurations with heat recovery and integration, new separation technologies, and to increase the efficiencies of existing process with the development new solvents. The efficiency of the capture process can be increased with the development of better performing chemical solvents used for gas separation, which is the focus of the present work. This work aims to develop the understanding and tools necessary to approach intelligent design

of new molecular solvents for CO₂ capture. We address two main questions, (1) how to tune CO₂-solvent interactions with molecular modifications of the solvent by studying the CO₂-solvent system at the molecular level and (2) how do CO₂-solvent interactions impact process energy demands and other performance metrics at the process level to identify the direction to modify solvents. This thesis is divided into two sections, one addressing building an understanding of chemical solvent-CO₂ interactions for post-combustion capture applications (Chapters 2 - 4) and the other using experimental and modeling techniques to build similar understanding for pre-combustion capture applications (Chapters 5 - 6).

2 An Overview of the Post-Combustion CO₂ Capture Process Using Amine Solvents

2.1 The Post-Combustion CO₂ Capture Process

Aqueous absorption/stripping using amine solvents is regarded as one of the most promising first generation CO₂ capture technologies for traditional coal-fired power plants.⁶ In this process CO₂ is removed from the flue gas stream by chemical absorption via reaction with a solvent, typically an amine (Figure 2.1). Decades of use in the food and natural gas processing industries, although at a smaller scale than would be necessary for CO₂ capture from a coal-fired power plant, has led to a large depth of operations knowledge for this process that is valuable for CO₂ capture compared to other newer processes. This, coupled with the wide applicability for CO₂ capture from other large point sources, i.e. natural gas power plants, refineries, and manufacturing plants, makes this process advantageous for CO₂ emissions mitigation.⁶

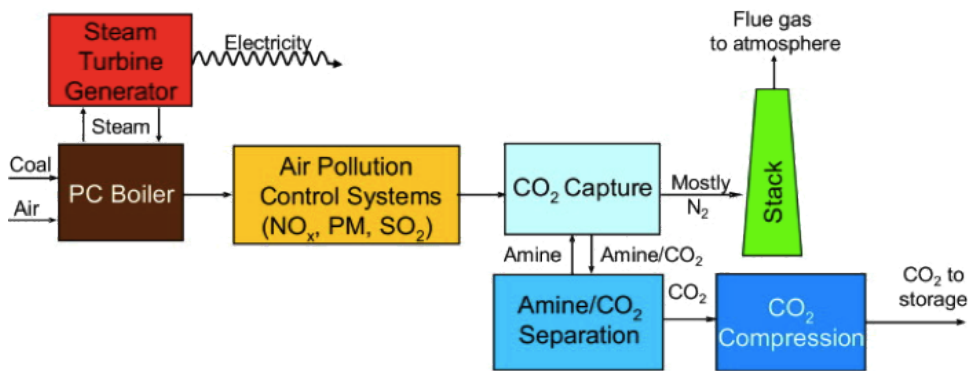


Figure 2.1: Block diagram of pulverized coal plant with a post-combustion CO₂ capture unit. Adapted from Rubin et al.²

The post-combustion capture process is a cyclic two tower process shown in Figure 2.2. The flue gas stream from the power plant is pre-cooled in a contact condenser and compressed slightly before entering the CO₂ absorber. In a crossflow configuration, solvent low in CO₂ concentration (Lean Amine), enters the top of the absorber. In the absorber, CO₂ reacts with the amine solvent resulting in a CO₂ lean overhead flue gas stream that can be emitted to the atmosphere and a solvent stream rich in CO₂ (Rich Amine) leaving the absorber bottoms. The Rich Amine is pre-heated in a crossflow heat exchanger, with the stripper bottoms as the heating stream, before entering the stripper. In the stripper, CO₂ is thermally driven out of the solvent, regenerating the amine and producing a moisture rich CO₂ overhead stream. The regenerated amine from the stripper bottoms is cooled before cycling back to the absorber as the Lean Amine.

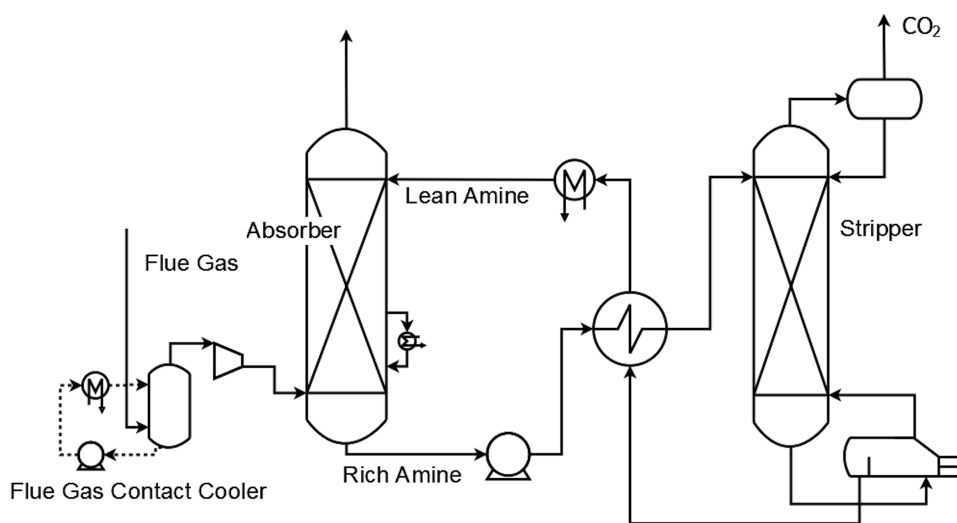


Figure 2.2: Simplified process flow digram of amine post-combustion CO₂ capture process.

The CO₂ overhead stream from the stripper is further processed based on the utilization or sequestration scheme identified for CCS. In most scenarios the location of utilization or sequestration will not be at the the power plant site. Therefore the CO₂ stream must be prepared for transportation as part of the capture process. This is done with a drying and compression process as shown in Figure 2.3.

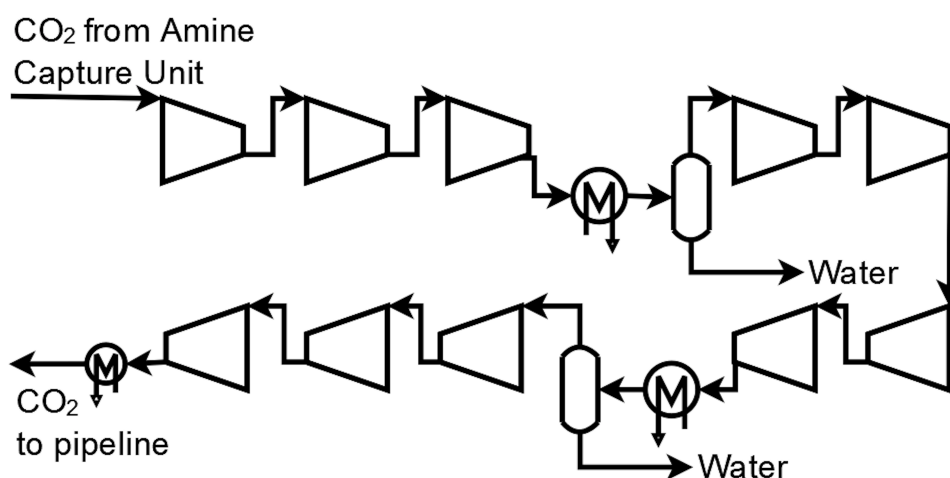


Figure 2.3: Simplified process flow diagram of CO₂ compression process.

Economic models estimate that 90% CO₂ capture from a new coal power plant using the leading commercial solvent monoethanolamine (MEA) could lead up to a 30% reduction in overall plant efficiency, corresponding to an 80% increase to the cost of electricity.⁷ This is due in part to the equipment size that is necessary to process large volumes of gas (2×10^6 m³/hr for a 550MW power plant),⁸ but predominantly due to the considerable parasitic energy demands of CO₂ capture. In the stripper low pressure steam from the steam cycle is used as the heat source to regenerate the amine. It is estimated that 40-50% of the low pressure steam is drawn off the steam cycle to regenerate the amine, and consequently not used for power generation. The steam utilized for

amine regeneration accounts for roughly 70% of the parasitic energy demands, with the next major contributor being the energy required to compress the CO₂ gas stream to pipeline conditions.⁹

As described by Oexmann and Kather, the thermal energy requirement for amine regeneration is fixed by three heating demands, the heat required to break the amine-CO₂ bond, latent heating of the solvent, and the required amount of stripping steam, all of which depend on the amine-CO₂ interaction energy.¹⁰ This relationship has motivated research focused on developing new amine solvents that have a lower energy penalty for CO₂ capture through the combined impacts on those three heating loads.

2.2 Amine-CO₂ Chemistry

The chemical absorption of CO₂ in amine solvent systems typically occurs through the formation of two products, a carbamate species and a bicarbonate species.¹¹ The overall carbamate reaction is shown in Equation 2.1. The protonated base, B, is usually another amine, giving an upper limit of 2:1 amine to CO₂ ratio for the carbamate pathway. This pathway is favored for primary and unhindered secondary amines.¹² The overall mechanism is still debated; the two leading theories are that the reaction occurs through the formation of a zwitterion intermediate (Equation 2.2) or carbamic acid intermediate (Equation 2.3).^{13–16}



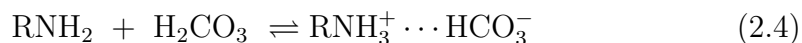
Overall Carbamate Reaction



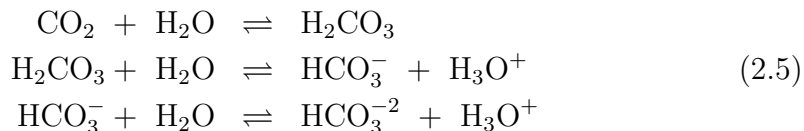
Zwitterion pathway



Carbamic Acid pathway



Overall Bicarbonate Reaction



Water - CO₂ Equilibrium

Bicarbonate formation occurs from the reaction of the amine with carbonic acid (Equation 2.4). CO₂ and water naturally equilibrate to form carbonic acid, bicarbonate, and carbonate species, but the equilibrium is not product (i.e. captured CO₂) favored in neutral water.¹⁷ Bicarbonate formation is enhanced in amine solvent solutions, since the amine is a more favorable Brønsted base than water to enhance product formation.¹⁸ Although possible with all amines, the bicarbonate pathway is commonly associated with hindered secondary and tertiary amines,^{12,19} where the barrier for carbamic acid formation is high due to steric hindrance around the interacting amine site or prohibited due to the lack of an N-H bond in the tertiary amine.

3 A Density Functional Theory Study of Amine Molecular and Electronic Structure Connections To Amine-CO₂ Reactivity

3.1 Introduction

As discussed in Chapter 2, the stripper heat duty, the largest parasitic energy demand of the post-combustion CO₂ capture process, is related to the amine-CO₂ reaction energy. The reaction energy can be modified through the presence of different functional groups on the amine. Given the exceedingly large number of amines that could be designed, it is important to understand the connection between the amine molecular structure and its reaction energy with CO₂. This chapter presents work using Density Functional Theory (DFT) modeling to understand the role of amine modifications in reactivity towards CO₂ by studying the variations in amine-CO₂ reaction energy of systematically different amines. A majority of the work presented here has been published in Lee and Kitchin.²⁰

Previous work studying amine-CO₂ systems predominantly focused on evaluating the CO₂ capture capacity for a range of amines with different functional groups, but an understanding of the relationship between amine properties and reaction enthalpy with CO₂ is still limited. Steric hindrance and amine basicity have long been standard descriptors of amine-CO₂ reactivity.^{12,19} However, the work of Puxty et al. challenges the completeness of this point of view.²¹ They measured the equilibrium CO₂ capacity of 76 amine solvents spanning primary, secondary, tertiary, and poly amines, and observed a wide range in capacity for the solvent systems. In some cases, solvents showed capacities exceeding the maximum theoretical performance

predicted by either an amine pK_a based capacity model for the bicarbonate pathway or a 2:1 amine to CO_2 interaction ratio along the carbamate pathway. Their work suggests that the relationship between reaction energy for the bicarbonate and carbamate pathway is more complicated than the simple framework of amine base strength, local geometry, and interaction ratios previously used to characterize amine- CO_2 reactions. Equally significant is that their work did not directly provide any molecular insight to the observed variations in performance.

More systematic studies of amine functionalization have shown evidence that the size and type of functional group play a role in amine- CO_2 reactivity. Singh et al. experimentally studied the effects of functional group chain length with alkylamines and alkanolamines and showed that the amine- CO_2 reaction was stabilized as the functional chain length increased.²² Mindrup and Schneider conducted a computational study on five groups of substituted amines using DFT to measure the trends in reaction energies relevant to CO_2 capture in the gas phase.²³ Their work showed that carbamic acid formation is more stable for the group of amines functionalized with electron-donating substituent and destabilized for amines with electron-withdrawing substituents. Additionally, they showed that the changes in reaction energy to form carbamic acid do not correlate with changes in amine protonation energy, suggesting that different properties of the amine control the reaction energy for carbamic acid formation and amine protonation.

The work of Chakraborty et al. provided some foundational insight into how the functional group alters the amine reaction site to control the energetics of the amine- CO_2 reaction.^{24,25} As the first to document the effects of functionalizing the alpha carbon of alkanolamines on the

amine-CO₂ reaction energy, they suggested that there was a molecular orbital interaction between the alpha carbon functional group and the local environment of the electron density around the nitrogen that led to destabilization of the amine-CO₂ interaction. However, the manner in which the local electron density changes was not addressed nor did the study consider the longer chain functional groups, which are now known to also impact amine-CO₂ reactivity. Xie et al. presented a closer look at substituent effects on carbamate and carbamic acid reaction energies by studying the reaction energy of alpha and beta carbon substituted monoethanolamine with CO₂.²⁶ Their work showed that the destabilization of the substituent effects on carbamate and carbamic acid formation was decreased as the number of carbons between the amine and the substituent increased, showing tunability of reactivity even within the selection of a single substituent. There remains a gap in understanding what molecular features control the amine-CO₂ reaction energies and how those features can be controlled through amine substitution, which has limited the design of new solvents with targeted properties.

The present work focuses exclusively on the relationship between molecular properties of amines and their influence on the amine-CO₂ interactions. Molecular modeling within the framework of density functional theory (DFT) was used to evaluate the reaction energy to form the product species associated with the amine-CO₂ system. Conceptual density functional theory was used to relate electronic structure properties of the amines to trends in their reactivity, with the purpose of providing the foundational understanding necessary to design of amine solvents with target reactivities towards CO₂.²⁷⁻²⁹ The objectives of this work are (1) to assess the impact of functionalizing amines on their reaction energy to form

products with CO₂, and (2) to identify descriptors based on electronic structure and reactivity properties that would enable the prediction of the reactivity of a new candidate amine towards CO₂.

3.2 Materials and Methods

In this work three classes of amines were studied: alkylamines, alkanolamines, and trifluoroalkylamines. The functional groups, -CH₃, -CH₂OH, and -CF₃, span a range of electron-donating and electron-withdrawing behavior and include hydrogen bonding groups. Within each class, primary, secondary, and tertiary amines were considered with three different alkyl chain lengths to determine the effects of type and proximity of the functional group and degree of functionalization on the amine-CO₂ reactivity. Figures 3.1-3.3 show the molecular structures of all 27 amines considered in this study.

R= CH ₃	Primary	Secondary	Tertiary
-R	H ₃ C-NH ₂		
-(CH ₂)R			
-(CH ₂) ₂ -R			

Figure 3.1: Alkylamines considered in DFT study of amine-CO₂ reactivity.


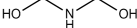
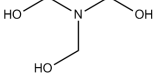
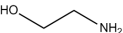
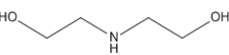
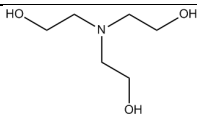

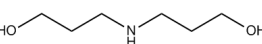
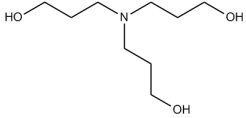
R=CH ₂ OH	Primary	Secondary	Tertiary
-R			
-(CH ₂)R			
-(CH ₂) ₂ -R			

Figure 3.2: Alkanolamines considered in DFT study of amine-CO₂ reactivity.

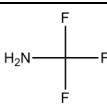
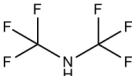
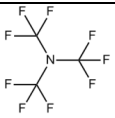
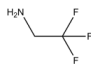
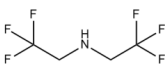
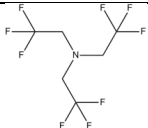
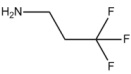
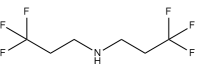
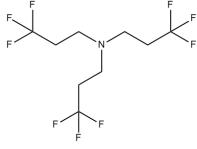
	Primary	Secondary	Tertiary
-R			
-(CH ₂)R			
-(CH ₂) ₂ -R			

Figure 3.3: Trifluoroalkylamines considered in DFT study of amine-CO₂ reactivity.

3.2.1 Density Functional Theory and Reaction Energy Calculations

The energy and electronic structure of the molecular systems were computed with Density Functional Theory (DFT) calculations using Gaussian 09 with the B3LYP functional and 6-31+G(d,p) basis set.³⁰ The B3LYP functional is sufficient to establish trends in molecular reactions of systems of the size considered in this study.^{14,23,31,32} Energy and electronic descriptor calculations were performed for a subset of the amines studied with a larger basis set, 6-311++G(d,p), with no changes to the energy correlations, indicating that the level of theory with using 6-31+G(d,p) was sufficient for the trends we observed. The solvent environment was simulated in the calculations using a polarizable continuum solvation model, with the integrated equation formalism model (IEFPCM), the united atom cavity model, and the dielectric constant of water.^{33,34} This approach has been shown to be reasonably accurate for solvent phase calculations compared to more complex representations of the solvent phase.^{35,36}

$$\Delta H_{rxn} = H_{Amine-CO_2(\ell)} - H_{Amine(\ell)} - H_{CO_2(g)} \quad (3.1)$$

The reaction enthalpy (ΔH_{rxn}) for a generalized CO₂ capture reaction, i.e. amine in the solvent (ℓ) reacting with CO₂ in the gas phase (g) to form a solvated amine-CO₂ product, is expressed in Equation 3.1. From the thermodynamic pathway shown in Figure 3.4, the overall reaction enthalpy can be expressed as the sum of two enthalpies, the enthalpy of CO₂ solvation ($\Delta H_{solv,CO_2}$) and the liquid phase amine-CO₂ reaction enthalpy (ΔH_{rxn}^ℓ), Equation 3.3.

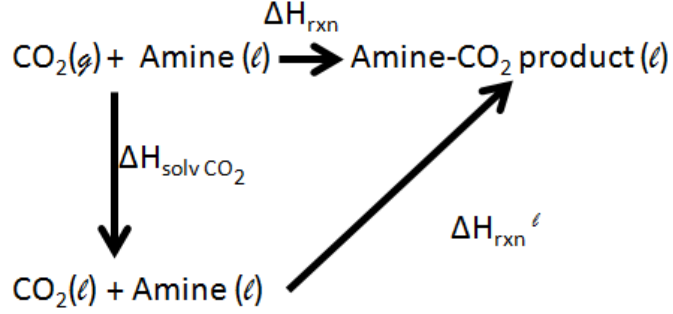


Figure 3.4: Thermodynamic pathway of amine-CO₂ reaction showing the relationship between the overall reaction and the solvent phase reaction.

Given the largely aqueous environment of amine solvents, the CO₂ solvation enthalpy is assumed to be constant for all amines. Thus, any variation in the overall reaction enthalpy will be captured by the liquid phase reaction enthalpy, $\Delta H_{rxn(\ell)}$. $\Delta H_{rxn(\ell)}$ can be approximated by the change in internal energy (ΔE), assuming the liquid system is incompressible, i.e. for the reaction $\Delta PV \approx 0$ (Equation 3.4). The reaction enthalpy analysis in this work focuses on ΔE_{rxn} , expressed in Equation 3.5, where the internal energy ($E_{298,i}$) of each species is the DFT computed energy in the simulated solvent environment of the IEFPCM model with zero point energy and temperature corrections.³⁷

$$\Delta H_{rxn} = \Delta H_{solv,CO_2} + \Delta H_{rxn}^{\ell} \quad (3.2)$$

$$\Delta H_{rxn}^{\ell} = H_{Amine-CO_2(\ell)} - H_{Amine(\ell)} - H_{CO_2(\ell)} \quad (3.3)$$

$$\Delta H_{rxn}^{\ell} = \Delta E_{rxn} + \Delta(PV)_{rxn} \approx \Delta E_{rxn} \quad (3.4)$$

$$\Delta H_{rxn}^{\ell} = \sum_i^{products} E_{298,i} - \sum_j^{reactants} E_{298,j} \quad (3.5)$$

Reaction energies for both the bicarbonate and the carbamate pathway were computed, including reaction energies for intermediates, considering product states consisting of non-interacting ions and interacting ion-complex product systems. Figure 3.5 shows a molecular representation for the reactions considered for the bicarbonate pathway. In Reaction 1, the bicarbonate and protonated amine were considered as a non-interacting product ion system and the energies of the each were computed in separate DFT calculations. In Reaction 2, the product system was considered as an interacting bicarbonate-protonated amine ion complex and the energy was calculated in a single DFT calculation. Figure 3.5 shows a molecular representation for the reaction energy calculations for intermediate and product formation for the carbamate pathway. Reactions 3 and 4 consider the zwitterion and carbamic acid intermediate. In Reaction 5, the carbamate ion and protonated amine energies were computed in separate calculations. In Reaction 6, the energy was calculated for the carbamate-protonated amine ion pair in a single calculation. All reaction energies were computed using the lowest energy (most thermodynamically relevant) conformation of the reactant and product molecules.

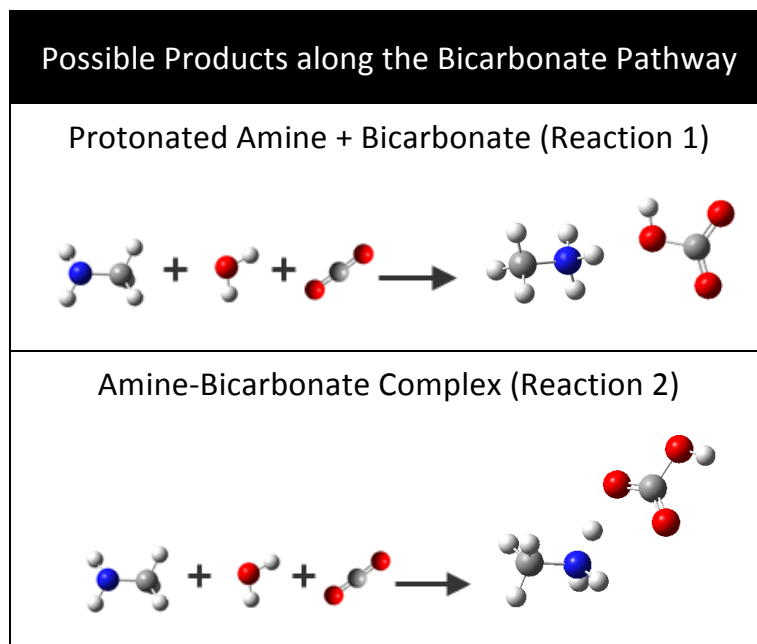


Figure 3.5: Reactions considered in this work along the bicarbonate pathway.

To identify the most thermodynamically relevant molecular conformation, a stochastic approach was used to create a large set of initial geometries for each molecule. For a given molecule with N_D dihedral angles associated with the molecular backbone, an algorithm generated $12N_D$ number of initial conformations by making random rotations of the dihedral angles. A geometry optimization was performed on each initial geometry, resulting in a set of stable conformers for each molecule. Figure 3.7a shows an example of the conformation search for MEA. The three backbone dihedral angles were rotated randomly to generate 36 initial geometries. Performing geometry optimizations on these recovered the known conformations of monoethanolamine, Figure 3.7b. For larger molecules with soft vibrational modes, this method recovers many local minima as seen in Figure 3.8 for tripropanolamine. The lowest energy molecular conformation was also used

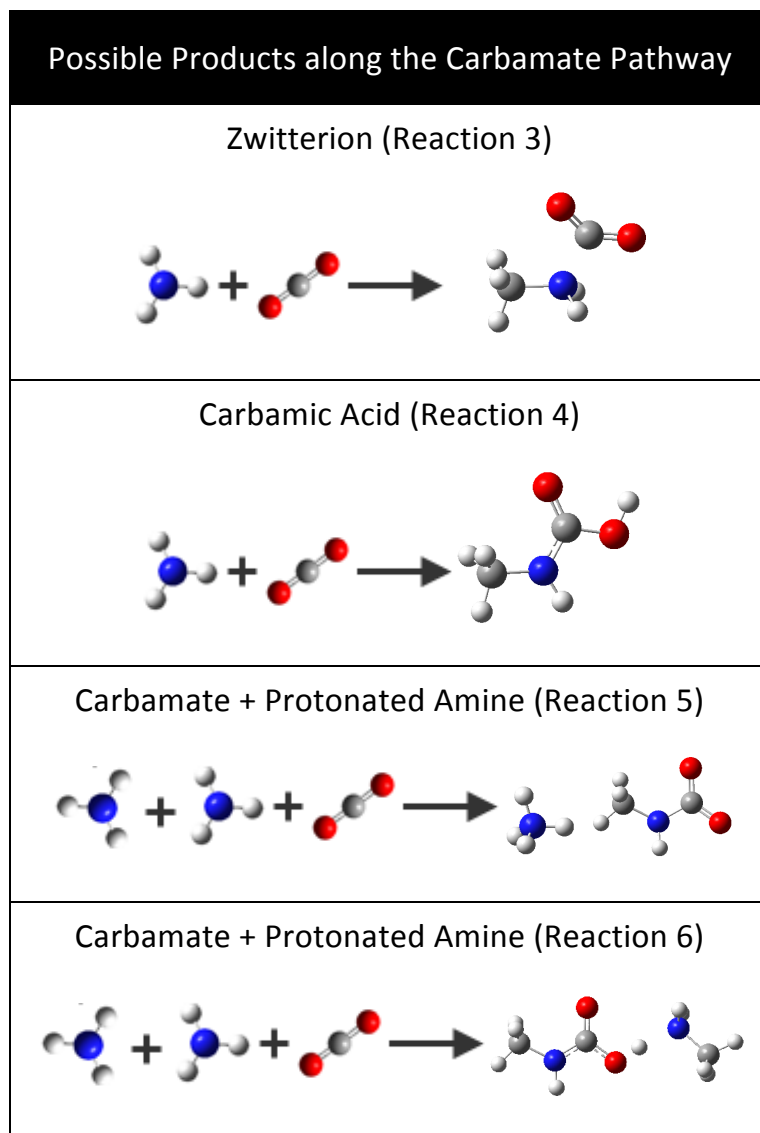


Figure 3.6: Reaction along the carbamate pathway considered in this study.

to perform the electronic structure property analysis using the mathematical relationships of conceptual density functional theory as described in the following section.

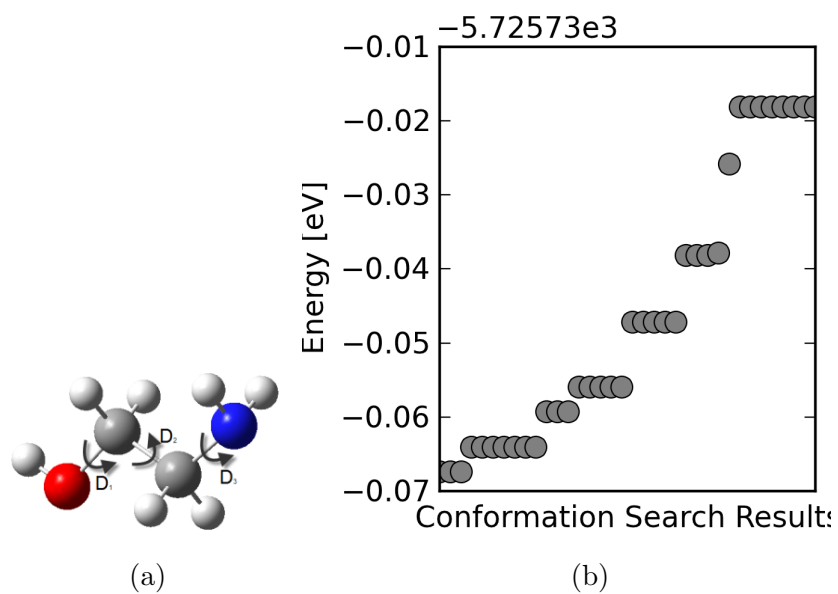


Figure 3.7: Lowest energy conformation search of MEA.

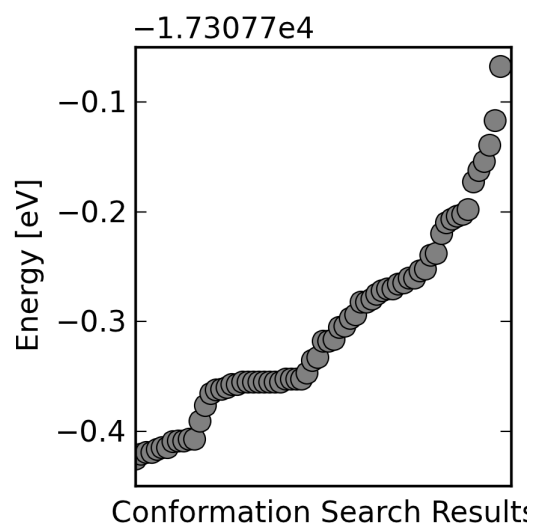


Figure 3.8: Lowest energy conformation search of tripropanolamine.

3.2.2 Theory of DFT Based Chemical Reactivity Descriptors

The context of the electronic structure property analysis is based in conceptual density functional theory, which connects mathematical relationships that naturally arise from density functional theory (DFT) to empirical concepts of chemical reactivity.²⁷⁻²⁹ The fundamental relationship between DFT and chemical reactivity was defined by Parr, Donnelly, Levy and Palke linking the electronic chemical potential, μ , to the first derivative of energy, E , with respect to the number of electrons, N , at a fixed external potential, $\nu_o(\vec{r})$.³⁸ The electronic chemical potential can be related to electronegativity using Equation 3.6.³⁹ This relationship is consistent with the qualitative understanding of these concepts; the electronic chemical potential is the escaping tendency of electrons from the system, while electronegativity measures the tendency of the system to attract electrons. Through a perturbation analysis, the derivative of energy with respect to the external potential at a constant number of electrons can be shown to be equal to the electron density, $\rho(\vec{r}) = \left(\frac{\partial E}{\partial \nu_o \vec{r}} \right)_N$. Collectively, this definition of density and Equation 3.6 are referred to as the first order energy response functions in conceptual DFT.

$$\mu = \left(\frac{\partial E}{\partial N} \right)_{\nu_o(\vec{r})} = -\chi \quad (3.6)$$

Sanderson’s electronegativity equalization principle uses electronegativity as a descriptor for the reaction between two states to form an overall product state.⁴⁰ This principle states that two bodies of different electronegativities interact in a manner such that the electronegativity of the product species is equalized to a value intermediate of the electronegativity of the reactants. The necessary electronegativity equalization between two reacting bodies could be

conceptualized as the driving force for interaction. Using results from DFT and Equation 3.6, the electronegativity difference of two reacting bodies can be quantified as a way to measure the driving force for reaction.

Second order response functions, shown in Equation 3.7 and Equation 3.8, are related to the concepts of absolute hardness and the Fukui function respectively and can be used to derive the local softness of a reacting site.^{41,42} The concepts of hardness and softness stem from Pearson’s work in understanding trends in the reactivity of Lewis acid base systems. Known as the principle of Hard and Soft Acids and Bases (HSAB), this concept states that hard acids react more strongly with hard bases and soft acids react more strongly with soft bases.^{43,44} Hard-hard interactions are more electrostatic in nature, while soft-soft interactions are more covalent in nature. Qualitatively, hardness describes systems of low polarizability, high electronegativity, and that are difficult to oxidize. Its conceptual counterpart, softness (S), refers to systems of the exact opposite characteristics: high polarizability, low electronegativity, and easily oxidizable. Mathematically, the definition of hardness, Equation 3.7, measures resistance to change of the electronic chemical potential due to a change in the number of electrons. Parr and Pearson showed that is conceptually equivalent to the qualitative chemical concept of hardness that Pearson first introduced.^{43,45} True to the qualitative definition, softness is mathematically defined as the inverse of hardness (Equation 3.9).

The Fukui function (Equation 3.8) quantifies the concepts of the frontier electron theory of Fukui et al.^{46,47} This theory describes the site selectivity of a reaction for a given molecule, where sites with a larger Fukui function are favored as the reaction site. This has correctly predicted well known trends

in intermolecular reactivity of many molecular systems, such as aromatics and carbonyl compounds.^{41,48-52}

$$\left(\frac{\partial^2 E}{\partial N^2}\right)_{\nu_0(\vec{r})} = \left(\frac{\partial \mu}{\partial N}\right)_{\nu_0(\vec{r})} = \eta \quad (3.7)$$

$$\left(\frac{\partial E}{\partial \nu_0(\vec{r}) \partial N}\right) = \left(\frac{\partial \rho(\vec{r})}{\partial N}\right) = f(\vec{r}) \quad (3.8)$$

$$S = \frac{1}{\eta} \quad (3.9)$$

A localized version of the HSAB principle, connecting concepts of frontier electron theory and HSAB principles, has been used to describe trends in intermolecular reactivity based on local properties of the reacting site.⁴⁹ This principle states that the soft-soft interaction of an acid (A) with a base (B) is favored when the reacting sites of the A and B have similar localized softness, s_i . The localized softness of a reacting site is determined by integrating the spatial representation of softness, $s(\vec{r})$, over the volume of the reacting site, Ω_i , as shown in Equation 3.10. The global softness is spatially resolved by projecting the global softness onto the Fukui function. We use the localized softness as an electronic structure descriptor for Lewis acid/base reactivity in this work by evaluating the localized softness of the nitrogen site of each amine. The volume of integration defined as the nitrogen (N) volume determined from Bader population analysis of the neutral amine.^{53,54}

$$s_i = \int_{\Omega_i} s(\vec{r}) dV = \int_{\Omega_i} S f(\vec{r}) \quad (3.10)$$

To evaluate electronegativity, a centered finite difference approach was used to evaluate the derivative, $\left(\frac{\partial E}{\partial N}\right)_{\nu_0(\vec{r})}$, shown in Equation 3.11. This is equivalent

to Mulliken’s definition of electronegativity, $\chi = \frac{I+A}{2}$, where I is the vertical ionization energy and A is the electron affinity.⁵⁵ For the density derivative associated with the Fukui function, finite difference approaches to evaluation of the derivative have been established based on the type of reaction.⁴⁷ These are shown in Equation 3.12 and Equation 3.13, where ρ_N is the density of an N-electron system, with both densities calculated at a fixed external potential.

$$\chi = - \left(\frac{(E_{N-1} - E_N) + (E_N - E_{N+1})}{2} \right)_{\nu_o(\vec{r})} \quad (3.11)$$

$$f^+(\vec{r}) = \rho_{N+1}(\vec{r}) - \rho_N(\vec{r}) \quad (3.12)$$

nucleophilic attack

$$f^-(\vec{r}) = \rho_N(\vec{r}) - \rho_{N-1}(\vec{r}) \quad (3.13)$$

electrophilic attack

Relationships between electronic property descriptors and reaction energies in this work were made using reaction energies computed using DFT electronic energies. Temperature and vibrational corrections to the energies were neglected in building the electronic property relationships to reactivity because these corrections are more a function of the molecular mechanics and not the molecular electronic state.

3.3 Results

Previous work studying the reaction energy of forming an amine-CO₂ product concentrated on the reaction energy associated with forming a carbamate species or a protonated amine.^{14, 15, 23, 56} This approach views the product state as two non-interacting ions and does not consider the

possibility of ion-pair formation through the interaction of these charged products with another charged species present in the system. Recently, transition state studies and ab initio molecular dynamics of amine-CO₂ systems showed in the case of the carbamate pathway, the stable product is a protonated amine-carbamate ion-pair, not the non-interacting two ion state.^{13,26,57} In this work, we performed reaction calculations for both a non-interacting ions and interacting ion-complex product systems for the bicarbonate and carbamate pathways (Figure 3.5- 3.6). For all amines, the reaction energy calculations showed that the ion-complex formation along both the bicarbonate and carbamate pathway were more favorable compared to the non-interacting ion product system. The reaction pathway diagrams shown in Figure 3.9 illustrate this point for NH₃ and MEA.

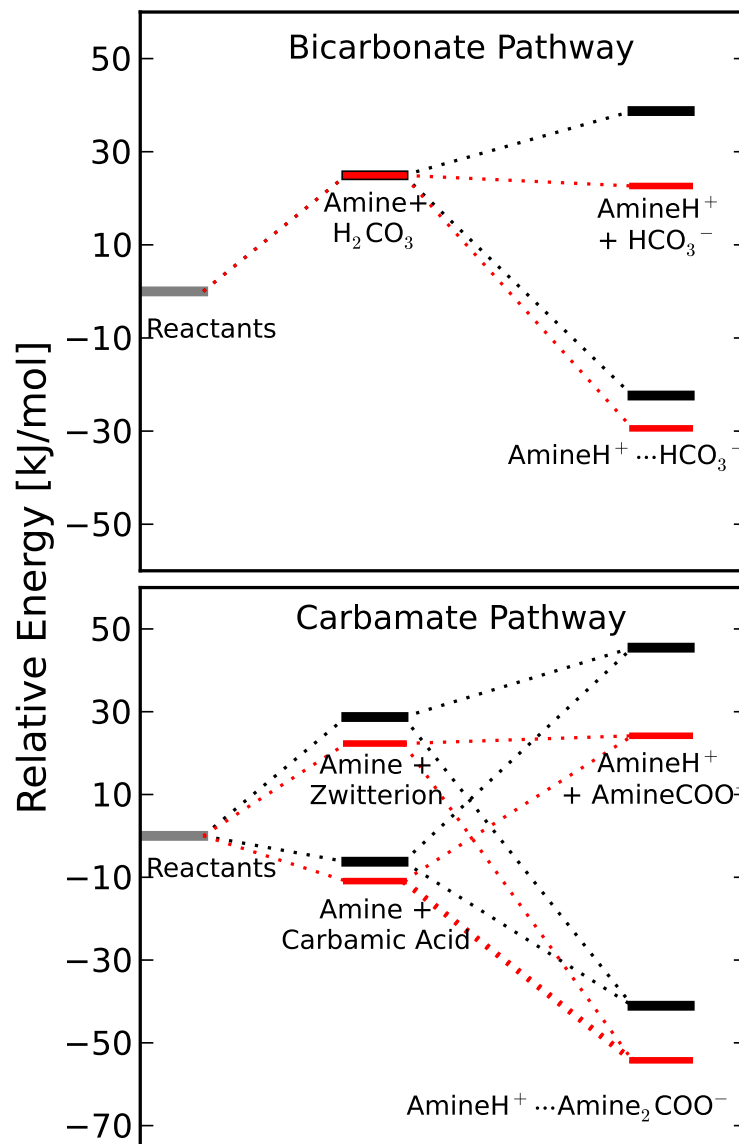


Figure 3.9: Reaction pathway diagrams showing the relative enthalpy (compared to enthalpy of reactants) of product states considered for the bicarbonate (a) and carbamate (b) pathway. Results for NH₃ are shown in black (—) and results for MEA are shown in red (—).

The amine-bicarbonate ion complex (Reaction 2) is characterized by an N-H-O interaction between the amine and bicarbonate, with the proton shared between them and a characteristic N-O distance of 2.66 ± 0.19 Å. The

characteristic ion-complex product was not found with the secondary and tertiary trifluoromethyl substituted amines ($\text{NH}(\text{CF}_3)_2$ and $\text{N}(\text{CF}_3)_3$). With these amines, the N-O distance was 3.12 Å and 4.5 Å respectively, with the H closely bound on the carbonic acid, indicating that these amines are not very basic. The interacting system for both of these amines was lower in energy than the corresponding non-interacting state, suggesting that possibly a long range weak electrostatic interaction existed between the amine and carbonic acid leading to a more stable product-like state, though not the amine-bicarbonate complex.

The carbamate pathway analysis was performed only for primary and secondary amines, because the reaction pathway is not possible for tertiary amines. Stable zwitterion species were found for all alkylamines and alkanolamines, and for primary and secondary trifluoropropylamines ($\text{NH}_2(\text{CH}_2)_2\text{CF}_3$ and $(\text{NH}(\text{CH}_2)_2\text{CF}_3)_2$). For the shorter trifluoroalkyl functionalized amines, the presence of the CF_3 group close to the reacting site of the amine had a destabilizing effect that prevented the close interaction with CO_2 necessary for zwitterion formation. Across all of the amines, the zwitterion intermediate was higher in energy than the carbamic acid intermediate. This is consistent with the view that the zwitterion, if present, would be a short lived intermediate in the amine- CO_2 -water system, given the energetic favorability of the proton transfer from amine nitrogen to either another base or to one of the oxygen atoms of the reacted CO_2 .^{13,58}

Figure 3.10 and Figure 3.11 show the reaction enthalpy of the bicarbonate ion-complex (Reaction 2) and carbamate ion-complex (Reaction 6) formation for the three groups of amines showing that the degree of substitution and type of substituent groups impact the stability of both product systems. Functionalizing NH_3 with an alkyl chain to form a primary

alkylamine stabilized the formation of both product complexes as compared to the product complexes formed with NH_3 (Figure 3.10a). Further functionalizing the amine with additional alkyl chains to form secondary and tertiary alkylamines increased the stability of the amine-bicarbonate complex, while decreasing the stability of the amine-carbamate complex. Both of these effects were independent of the length of the substituent chain, indicating that the minor increase in the inductive electron donating ability of the alkyl chain due to an increase in the chain length on the reactivity of the amine is outweighed by the effect of replacing a hydrogen atom with a carbon chain. Similar enhancements due to the presence of an alkyl functional group is seen with ionic liquids and gas phase amines.^{23,31}

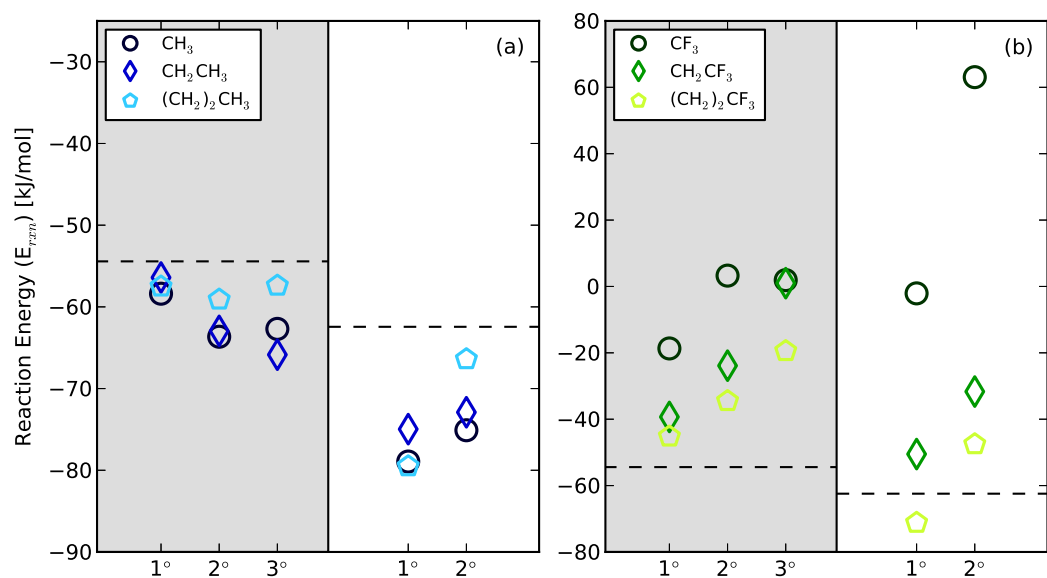


Figure 3.10: Reaction energy of amine-bicarbonate complex, Reaction 2 (gray area), and amine-carbamate complex, Reaction 6, formation for primary (1°), secondary (2°), and tertiary (3°) alkylamines (a) and trifluoroalkylamines (b). The reaction energy to form the respective product formation with NH_3 is denoted by the dashed line.

Functionalizing NH_3 with trifluoroalkyl groups destabilized the formation of both the amine-bicarbonate and amine-carbamate complex (Figure 3.10b). The destabilization was strongest when CF_3 , a strong inductive electron withdrawing group, was closest to the reacting site of the amine. As the carbon chain length separating the CF_3 group from the amine increased, the destabilizing effect was lowered. This is consistent with observations made by Xie et al. showing that destabilization effects of substituents on MEA were reduced as the substituent moved from the alpha to the beta carbon.²⁶ Since the effect persists in cases where the functional group is beyond the alpha carbon of the amine, a cause beyond interactions between the molecular orbitals of the alpha carbon and the reacting amine site alters the local electronic environment and causes destabilization of the product species.

Alkanolamines showed behavior in between the other two groups of amines, which was expected given the moderate inductive electron-withdrawing nature of the -OH group and its ability to participate in product stabilizing hydrogen bonding (Figure 3.11a).⁵⁹ First considering the product species without hydrogen bonding, with the primary methanolamine, the moderate electron-withdrawing effect -OH has a slight destabilizing effect, but is enhanced as the amine is further functionalized with methanol groups. As the functional chain length increases, the destabilizing effect of the -OH group is reduced, as observed previously with the trifluoroalkylamines. Figure 3.11b shows the reaction energy analysis including the additional stabilization due to hydrogen bonding was observed with both product complexes. Hydrogen bonding was observed in alcohol amine systems large enough to form five to six atom rings through intramolecular hydrogen bonds. The trends in reactivity attributed to amine

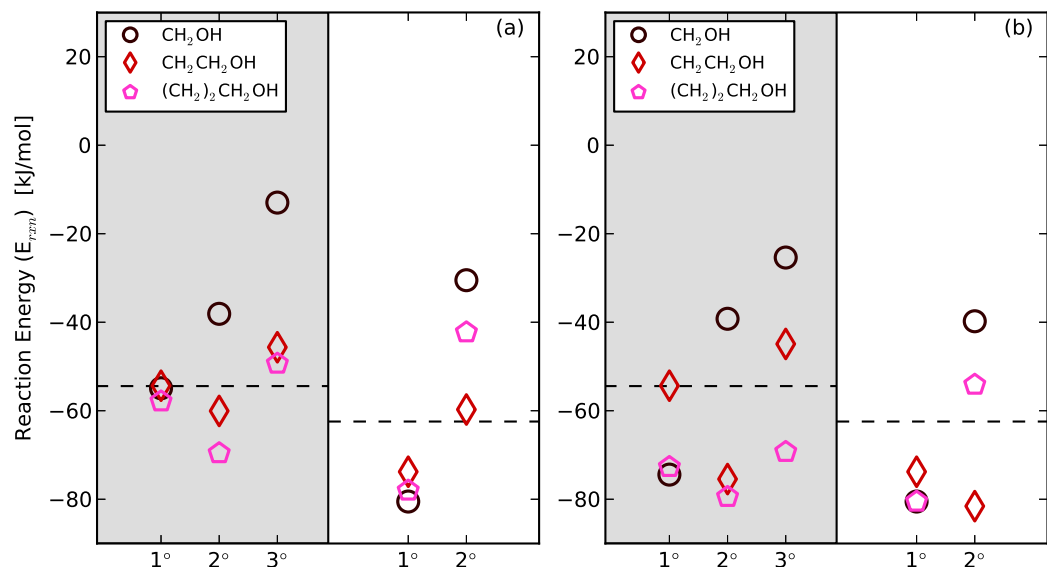


Figure 3.11: Reaction energy of amine-bicarbonate, Reaction 2 (shaded in gray), and amine-carbamate, Reaction 6, complex formation for primary (1°), secondary (2°), and tertiary (3°) alkanolamines without effects of intermolecular hydrogen bonding(a) and alkanolamines including intermolecular hydrogen bonding (b). The reaction energy to form the respective product formation for NH_3 is denoted by the dashed line

functionalization are clearer within the non-hydrogen bonding data set, thus the systems without hydrogen bonding will be used in the further analysis.

The molecular and electronic structure analysis of bicarbonate formation

Sanderson's concept of two body interactions is applicable to the interaction between carbonic acid and amines to form the amine-bicarbonate complex. The electronegativity difference of the amine and carbonic acid drives the charge transfer between the bodies necessary to equalize their electronegativity, resulting in an acquired partial charge and electrostatic interaction in the product species. Based on this principle, one expects that the electronegativity difference of two reactants may be a descriptor of

reactivity for the bicarbonate formation reaction. The reaction energy for amine-bicarbonate complex formation is plotted against the electronegativity difference between the two reactants, amine and carbonic acid, in Figure 3.12. As the electronegativity difference between the two reactants increases, the reaction energy to form the amine-bicarbonate complex is larger leading to a more stable amine-bicarbonate complex. Figure 3.13 shows that this relationship between amine-bicarbonate reaction energy and electronegativity is not sensitive to molecular conformation. When performing the same analysis on reactant conformations within 9.65 kJ/mol of the lowest energy conformation, the relationship persists.

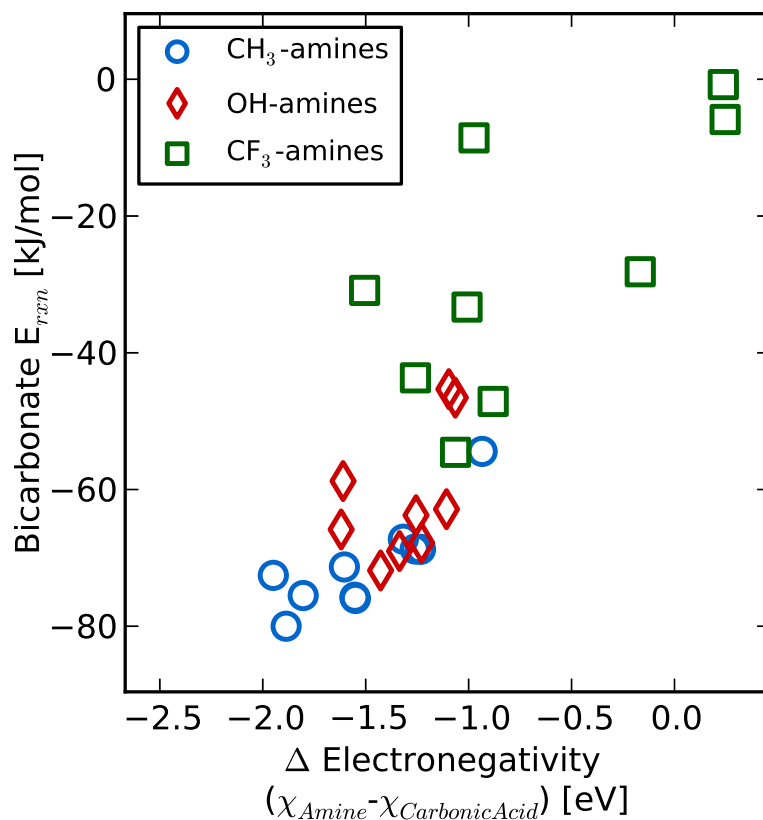


Figure 3.12: Amine-bicarbonate complex reaction energy as a function of the difference in the electronegativity of the amine reactant and carbonic acid.

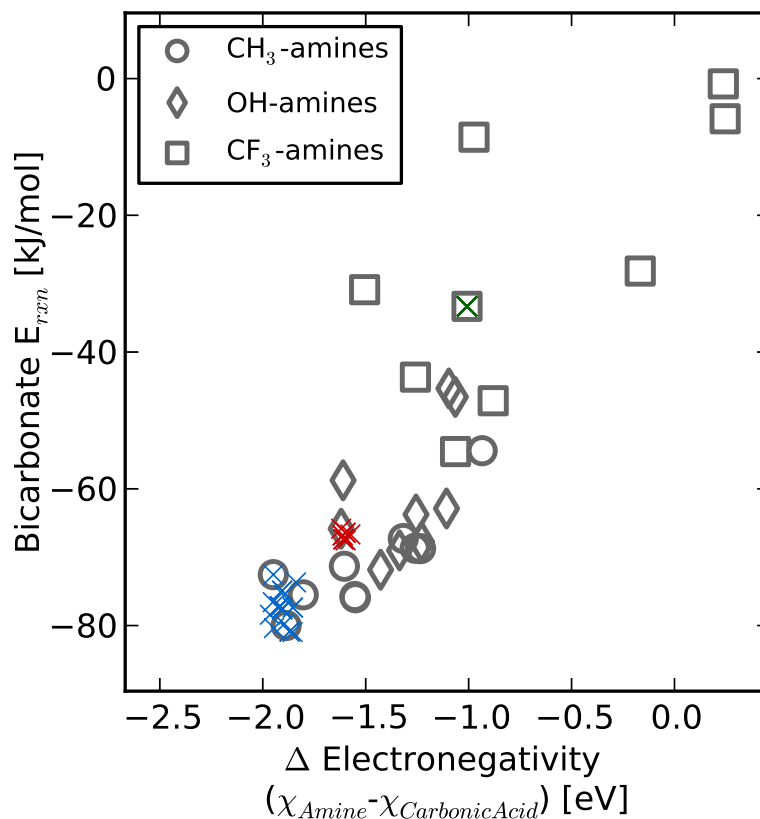


Figure 3.13: The amine-bicarbonate complex reaction energy as a function of the difference in the electronegativity of the amine reactant and carbonic acid for the lowest energy amine reactant conformation (gray) and conformations within 0.1 eV of the lowest energy conformation for tripropylamine (blue), tripropanolamine (red), and di-trifluoroethylamines (green).

There is a broad, but finite, range of reactivity for the formation of an amine-bicarbonate complex, spanning approximately 0 to -80 kJ/mol, suggesting a broad range of tunability based on the molecular structure of the amine. Since the electronegativity of carbonic acid is a constant, any tuning of the reaction energy along the bicarbonate pathway can solely be achieved by changes in the amine electronegativity through modifications to the molecular structure. Figure 3.14 shows the relationship between amine electronegativity and substituent groups on the amine. Electron withdrawing

functional groups like -CF_3 and -OH increase the electronegativity of the amine. This effect is strongest when the electron withdrawing group is directly substituted on the amine and is dampened when the carbon length of the substituent chain increases. With a longer chain substituent, the variations in electronegativity approach that seen with alkyl amines. The electronegativity of the amine can be systematically varied through the addition of substituent groups. However, there is a finite range over which the electronegativity of the amine can rationally be varied, of which a large portion has been sampled in this study, given the range in electron donating and electron withdrawing groups studied. This implies a limit to the range in achievable reactivity with amine-based solvents along the bicarbonate pathway.

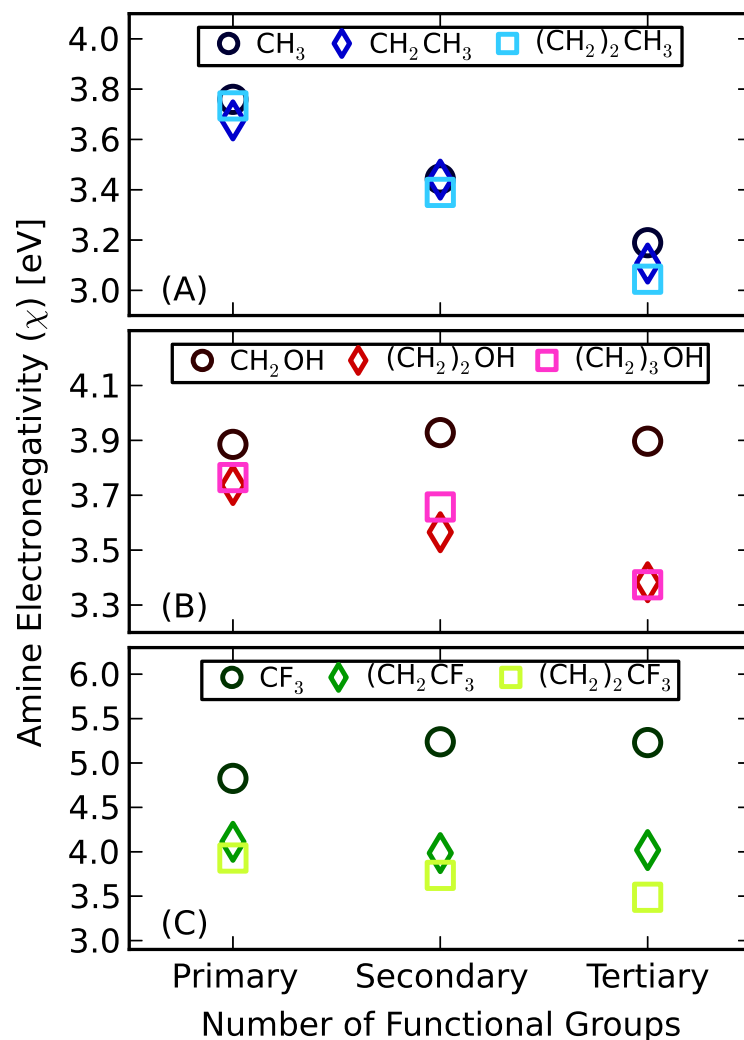


Figure 3.14: Electronegativity of primary, secondary, and tertiary amines for the (A) alkylamines, (B) alkanolamines, and (C) trifluoroalkylamines groups calculated using Equation 3.11.

The molecular and electronic structure analysis of carbamate formation

The defining characteristic of the carbamate pathway reaction is the formation of the N-C bond of the carbamic acid intermediate. We found that the carbamate reaction energy was reasonably correlated with the carbamic

acid formation reaction energy (Figure 3.15). Thus, for the electronic structure analysis of carbamate formation, we will focus on the reaction energy for the formation of the carbamic acid intermediate.

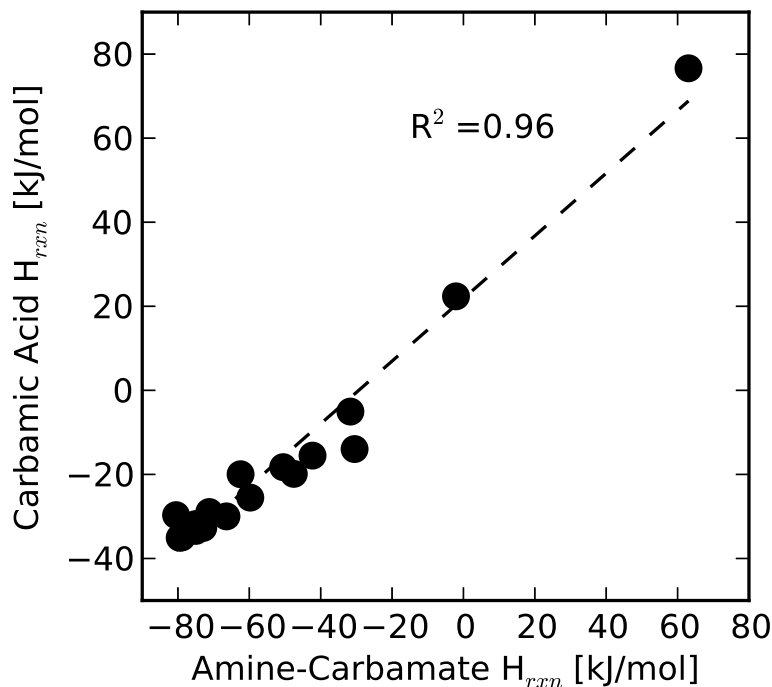


Figure 3.15: Correlation between amine-carbamate reaction energy and carbamic acid reaction energy.

The formation of carbamic acid is a Lewis acid/base interaction between the amine and CO_2 , where the amine undergoes electrophilic attack by CO_2 . The local Hard Soft Acid Base principle (HSAB) suggests that the energy associated with the covalent bond formation in carbamic acid should be correlated with the relative softness of the amine site to that of CO_2 . Figure 3.16 shows the relationship between the carbamic acid formation reaction energy and the localized softness of the amine nitrogen (s_N). The relationship is qualitatively consistent with the concepts of the HSAB; the

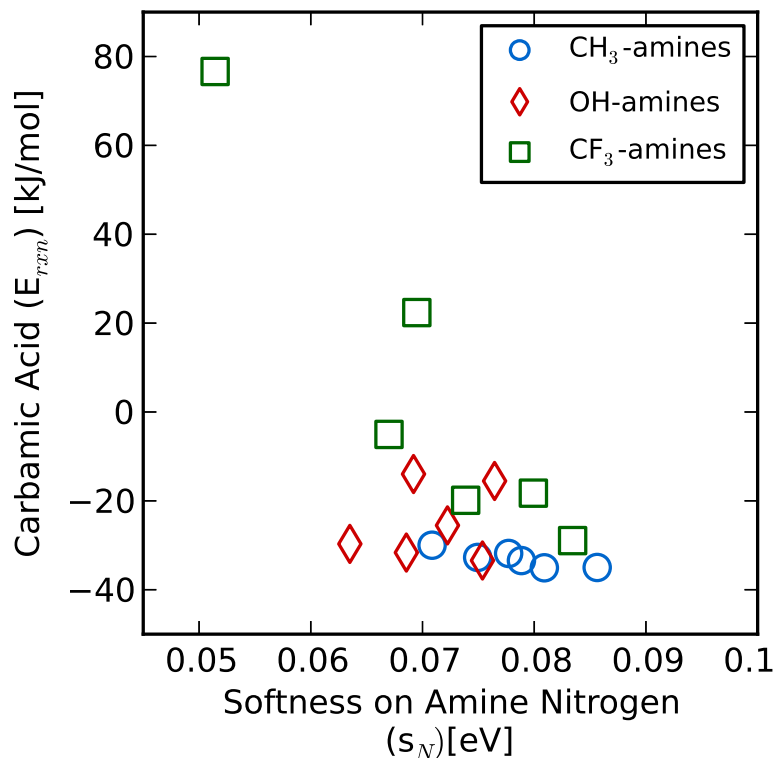


Figure 3.16: The reaction energy for carbamic acid formation as a function of the localized softness of the amine nitrogen (s_N). The softness of the reacting carbon (s_O) on CO_2 is 0.09 eV.

closer in value the localized amine softness of the nitrogen site is to the localized softness of the reacting site on CO_2 , the more exothermic the formation of carbamic acid. However, a single correlation for all of the amine families was not observed. Two correlations can be seen with the carbamic acid reaction energy and nitrogen site softness: one for trifluoroalkylamines and the other for alkanolamines and alkylamines. The response of the trifluoroalkylamine carbamic acid reaction energy to changes in s_N is strong, whereas the carbamic acid reaction energy dependence on s_N is much weaker for the alkyl and alkanolamines. This suggests that nitrogen softness is a good descriptor of the carbamic acid reaction energy for some amines, but

not simultaneously for all amines. It may be possible that inclusion of mechanical effects like steric hindrance need to be included to capture the remaining variations in reactivity.⁶⁰

The localized nitrogen softness of the amine can be tuned with amine functionalization as seen in Figure 3.17. Functionalizing the amine with strong electron withdrawing groups like with the trifluoroalkylamines gives a large range in s_N . The presence of the electron-withdrawing group decreases s_N , with the effect being strongest when CF_3 is closest to the nitrogen site and diminishing as the chain length increases. The s_N can be further reduced with the addition of more electron-withdrawing groups through amine functionalization (primary to a tertiary amine). The range in s_N observed with the alkanolamines is much smaller, though the trend from the presence of the moderate electron-withdrawing OH group has similar qualitative effects as in the trifluoroalkylamines.

Multiple correlations between s_N and the reaction energy can be rationalized through a subtle point within HSAB theory, which states that the relationship between the relative reactivity and reaction site softness holds only for Lewis acid/base groups that are similar in nature, e.g. structurally or chemically similar.⁴⁹ The three groups of amines in this study were selected to maximize structural similarity between the groups. However, Figure 3.18 suggests that there are some underlying differences between the trifluoroalkylamines and the alkanolamines and alkylamines. This point is further substantiated when examining the geometric characteristics of the carbamic acid product of each group of amines. Figure 3.18 shows the N-C bond length between the amine and CO_2 and the O-C-O bond angle for each carbamic acid intermediate. The bond distance and O-C-O bond angle between CO_2 and the trifluoroalkylamines is characteristically larger

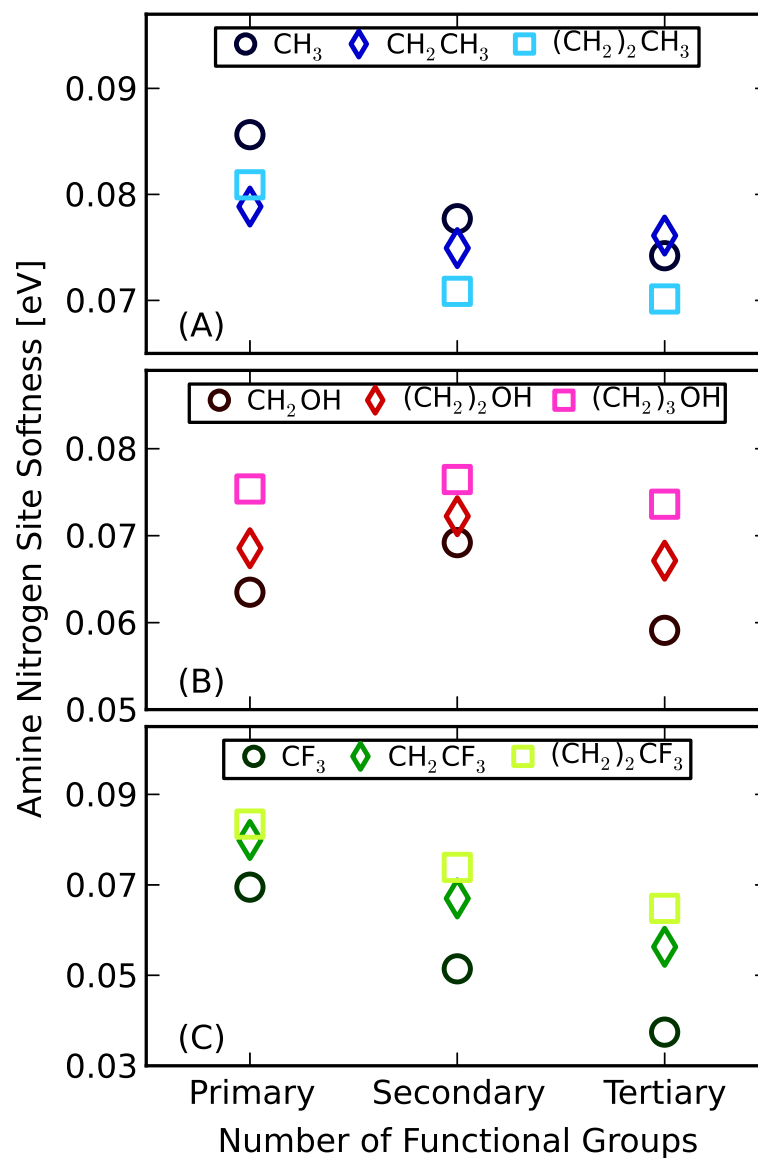


Figure 3.17: Trends in the localized softness on the amine nitrogen primary, secondary, and tertiary amines for (A) alkylamines, (B) alkanolamines, and (C) trifluoroalkylamines groups.

compared to the bond distance and bond angle with the other two groups of amines. These differences suggest that a different type of interaction occurs with the trifluoroalkylamine group, which may be possibly attributed to

long-range effects of the molecule’s electrostatic potential that does not allow a more intimate interaction between CO_2 and these amines.

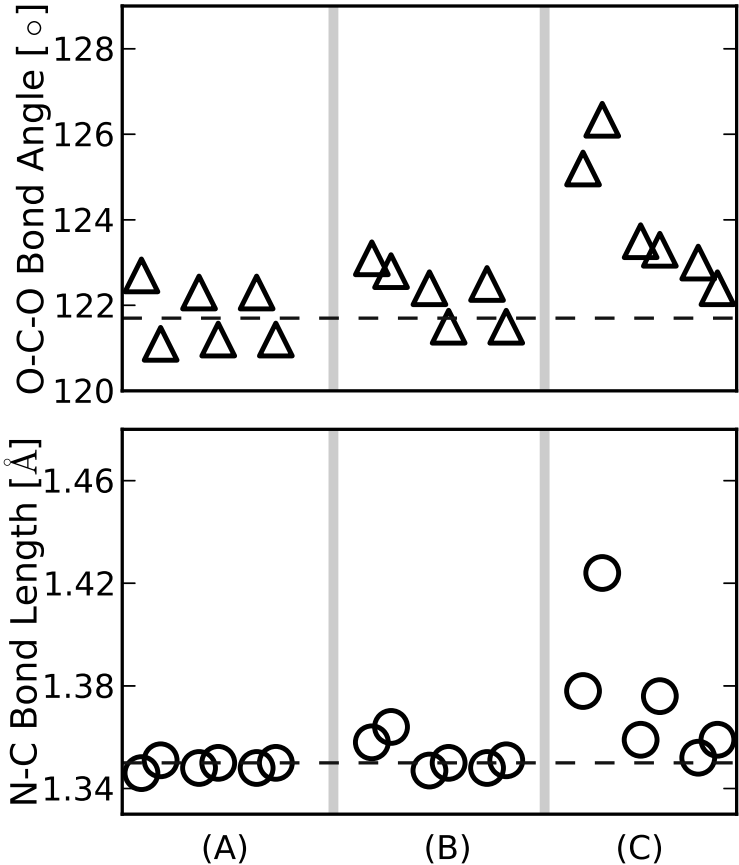


Figure 3.18: Molecular geometry descriptors of carbamic acid, O-C-O bond angle [°] (top) and N-C bond length [Å] (bottom) for (A) alkylamines, (B) alkanolamines, and (C) trifluoroalkylamines.

3.4 Conclusion

This work evaluated the reactivity of three groups of functionalized amines: alkylamines, alkanolamines, and trifluoroalkylamines, along the two main CO_2 capture pathways using density functional theory. Reaction energies including solvation effects were computed for several possible product species along each

pathway. For both the bicarbonate and carbamate pathway it was determined that the respective product ion-pair complex, amine-bicarbonate (Reaction 2) and amine-carbamate (Reaction 6), was more stable than the disassociated non-interacting product. Additionally, with respect to the carbamate pathway, it was determined that the carbamic acid is the likely intermediate state.

Trends in reaction energies were correlated to electronic structure properties through conceptual understanding of molecular interactions. In this work we selected two electronic property descriptors, electronegativity and local softness, due to their connection to qualitative principles of reactivity. Leading from Sanderson’s electronegativity equalization principle, the electronegativity difference between the amine and carbonic acid was identified as a good descriptor of the reaction energy to form the amine-bicarbonate complex. Additionally, it was found that through amine functionalization the electronegativity of the amine could be tuned. Following from the Hard Soft Acid Base principle, the local softness of the amine site was identified as a partial descriptor of the reaction energy along the carbamate pathway. The correlation between local amine softness and carbamate reaction energy was found to be weak for alkylamine and alkanolamine groups, and moderate for the trifluoromethyl functionalized amines. This indicates that a single descriptor may not be adequate in describing the reaction energy along the carbamate pathway.

4 What Is the Impact of Solvent Selection?

A Multi-objective Analysis of the Post-Combustion CO₂ Capture Process Using MEA, DEA, and AMP

4.1 Introduction

As discussed in Chapter 2, the stripper reboiler heat duty is the largest parasitic energy requirement of the post-combustion CO₂ capture process. The reaction energy plays a large role in this energy demand, which motivates research, like the work presented in Chapter 3, to understand the relationship between reaction energy and amine structure. Although knowledge of how to tune the amine-CO₂ reaction energy is valuable, the reaction energy, as well as other experimentally acquired measures of performance at the laboratory scale like capacity, diffusivity, reaction rates etc..., do not readily translate to process level measures of performance. Oexmann and Kather described the complex relationship between amine-CO₂ reaction energy and the parasitic energy demands of the post-combustion capture process.¹⁰ The reaction energy dictates many factors associated with how the process operates that impact the overall parasitic energy demands. Thus, understanding the process implications of the amine-CO₂ reaction energy of new solvents is critical in order to guide the direction of new solvent development in the laboratory. This chapter presents a framework to evaluate the performance of different amine solvents utilizing an approach to fairly assess the impact of the solvent on the process.

Aspen Plus process models have been used as tools to study the CO₂ capture process and quantify process energy demands, with a majority of the existing work using MEA as the capture solvent. Early works used these models to determine energy and mass balances around each process unit for a fixed process with a specific focus on determining the overall energy demands.⁶¹⁻⁶³ More recently, Aspen Plus models have been used to understand the relationship between operating conditions of the CO₂ capture process and energy demands, specifically the stripper reboiler heat duty. Parametric studies show that both equipment and process operating conditions, such as the CO₂ loading and temperature of the amine solvent entering the absorber, the absorber temperature, and stripper pressure, have a large impact on the stripper reboiler heat duty.⁶⁴⁻⁶⁶ These studies illustrate the large multi-dimensional design space of the post-combustion CO₂ capture process and emphasize the need to determine the best conditions for each solvent that optimize the design objectives, instead of arbitrarily setting them, when judging the performance of a process using a specific solvent.

Few studies have performed analysis of the CO₂ capture process using other amine solvents in addition to MEA.⁶⁷⁻⁷¹ However, many of the approaches used in those works limit the ability to fairly compare the energy demands of the different solvents and understand the impact of changes in amine-CO₂ reaction energy on the process. Chakma et al. presented a parametric study examining the impact of design variables as well as the choice of solvent selection on the cost of CO₂ capture, in \$CAD/ton CO₂ captured.⁷¹ They performed the cost comparison for six different amine solvents considering the market price of each solvent, which unfairly biases solvents that currently have a large market demand. Additionally, it is unclear if any process optimization was performed for each solvent, or if a

fixed process was used. Chang and Shih modeled three design schemes for the CO₂ capture process using two different amines, MEA and a mixed diglycolamine/methyldiethanolamine (DGA/MDEA).⁶⁷ Their analysis focused on identifying the major design variables for each amine, but they only performed a design optimization for the MEA. Similarly Dave et al. presented a comparison of the thermal energy requirements of amine regeneration of a fixed CO₂ capture process using MEA, DGA (diglycolamine), and AMP (2-amino-2-methyl-1-propanol).⁶⁸ The process operating conditions used for all the amines were those optimized for 30 wt.% MEA. Utilizing a fixed design and operating conditions of a process to compare the performance of different amines, obscures their true performance differences due to changes in amine-CO₂ chemistry and the results likely do not present the amine in the best light. Numerous process models of the MEA system have shown the significant effect of different operating conditions on the energy demands of the process. Additionally, each amine has a different chemistry with CO₂, which would likely lead to different optimal process operating conditions. Thus, it is important to model the CO₂ capture process using conditions best suited for the capture solvent.

Nuchitprasittichai and Cremaschi present a simulation-optimization approach using response surface optimization methods to analyze the impact of different amine solvents, solvent concentration, absorber and stripper column heights, and operating conditions on the \$/ton of CO₂ captured of a post-combustion capture process.⁷⁰ The optimization approach allowed the evaluation of the cost of CO₂ capture with each amine using the conditions best suited for that amine. However, their analysis only focused on the cost of CO₂ capture in the optimization, and did not consider the impact of the capture process on the overall plant net power output, which is the

performance measure that is most affected by amine-CO₂ chemistry of different solvents. Additionally, performance criteria on the capture process, i.e. 90% CO₂ capture (the target set by the DOE), was not imposed on their model.

The work in this chapter aims to address an existing gap in the understanding of the impact of solvent selection on the post-combustion CO₂ capture process by presenting a framework to analyze and compare the energy penalty and capital cost demands of a CO₂ capture process using different amine solvents. The CO₂ capture process is modeled in Aspen Plus using a fixed process flowsheet. The process models are coupled with a multi-objective genetic algorithm that sampled a defined design space of process and operating conditions, to determine sets of conditions that were best suited for each solvent to meet design objectives that maximize net power output of the overall power plant and minimize the capital cost investment of the CO₂ capture process. A traditional optimization approach could be used to determine the optimum point within the design space with respect to the design objectives. However, as highlighted in the work of Eslick and Miller, the multi-objective genetic algorithm approach results in a set of near optimal Pareto solutions.⁷² This solution set provides information about the behavior the system near optimal conditions and about the associated trade-offs between design objectives. We present the multi-objective analysis for three amine solvents, MEA, DEA (diethanolamine), and AMP. Comparisons of the Pareto front for each amine show the impact of solvent selection on the process and can be utilized to identify better performing amines.

4.2 Materials and Methods

4.2.1 Process Simulation and Optimization Information Flow

This work combines process models and a genetic algorithm analysis to sample a multi-dimensional design and operating space for the post-combustion CO₂ capture process to satisfy capital cost and power efficiency design objectives for the overall process. The CO₂ capture process was modeled with Aspen Plus (Section 4.2.2). The Aspen models were linked to an Excel-based simulation interface, Sinter, developed through the DOE Carbon Capture Simulation Initiative (CCSI).^{72,73} The Sinter application has Excel and VBA functionality and allows information input/output with Aspen simulations and execution of the simulations. Sinter was linked to modeFrontier, an optimization and data analysis tool, to carry out the genetic algorithm analysis (Section 4.2.4). Figure 4.1 shows a schematic of the information flow.

4.2.2 Aspen Plus Process Models

The standard amine based CO₂ capture and compression processes were considered in this work (Figure 2.2 and Figure 2.3 respectively), with the exception of the direct contact condenser. The direct contact condenser is traditionally considered as part of the CO₂ capture process, but not included in this analysis because it is a flue gas pretreatment unit and its size and performance is independent of amine selection. The CO₂ compression unit is included because the energy of compression accounts for a substantial portion of the power plant energy penalty of to CO₂ capture. Additionally, the compression energy also depends on the outlet conditions of the stripper, which is impacted by the amine-CO₂ chemistry.¹⁰

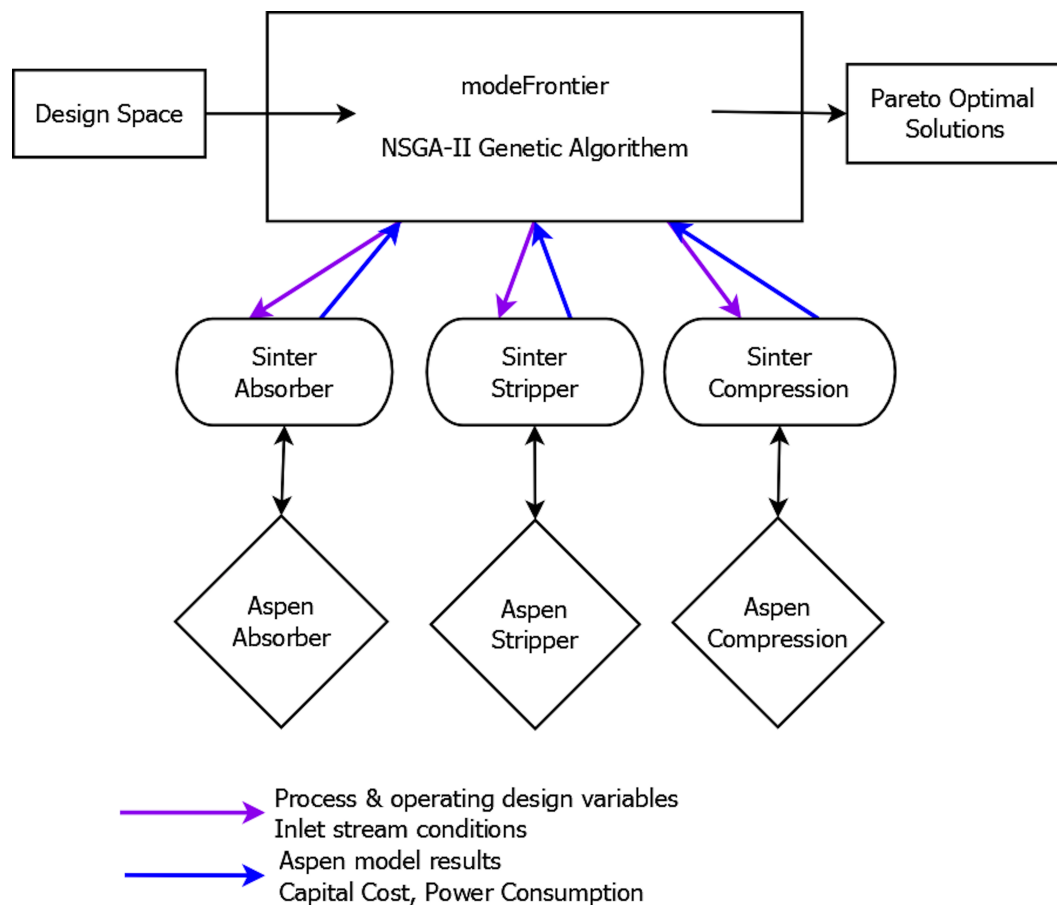


Figure 4.1: Information flow of modeFrontier, Excel, and Aspen Plus applications.

Process models were developed using Aspen Plus v.7.2 and the electrolyte-non random two liquid (NRTL) thermodynamic model with the electrolyte property inserts for each amine.⁷⁴ The flue gas inlet conditions were taken from the National Energy Technology Laboratory (NETL) 2010 bituminous coal baseline report for a 550 MW supercritical pulverized coal power plant and are shown in Table 4.1.⁸ For each amine, the amine solvent composition was fixed at 11 mol% amine basis, which is equivalent to 30 wt% MEA. Since the purpose of this study was to assess the impact of changes in the amine-

CO₂ chemistry on process performance, a fixed amine mol% basis was used for all amines to keep the number of available reacting molecules constant and ensure that any differences in process performance were only an effect of different chemistries.

Temperature [°F]	134.4
Pressure [psi]	16
Flowrate [lb/hr]	4,797,765
Mass Fraction	
N ₂	0.718
H ₂ O	0.071
CO ₂	0.211

Table 4.1: Flue gas inlet conditions used for multi-objective post-combustion capture process models.

The CO₂ capture process was modeled as five parallel trains. The CO₂ overhead streams from the five strippers were fed into two parallel CO₂ compression trains. Each unit, the absorber, stripper, and CO₂ compression units were modeled with three separate flow sheets(Appendix A). The absorber was modeled using the rate-based RadFrac tower model, with a five foot water wash section, 35 discretization sections, using Sulzer MellapackPlus 252Y packing. The absorber height was not fixed and considered as a design variable (Section 4.2.4). An intercooler was included in the lower section of the absorber,⁶⁷ drawing off hot liquid from a section and returning cooled liquid to the section below. A design objective was implemented in the process simulation to remove 90% of the CO₂ from the flue gas stream by adjusting the Lean Amine flow rates. The diameter of the

absorber was designed for 80% flooding. The Rich Amine conditions were recorded in modeFrontier and passed to the stripper Aspen model through the Sinter interface.

The stripper was also modeled using a rate-based RadFrac tower model, with 22 discretization sections, using Sulzer MellapakPlus 252Y structured packing, a kettle reboiler, and a partial vapor condenser. The stripper height was also not fixed and considered as a design variable, and sized for 80% flooding. A design specification was implemented in Aspen to adjust the reflux ratio and condenser temperature to produce a Lean Amine stream with CO₂ loading used in the absorber model. The stripper temperature was limited by the temperature of the low pressure steam draw (274.5 kPa, 267 °F). The reboiler temperature was not further constrained to limit the thermal degradation of the amine. Although, Davis and Rochelle have shown that thermal degradation of MEA does occur at elevated temperatures at lower CO₂ loadings, 0.2 mol CO₂/ mol amine, the degradation rate of the solvent at 275 °F is low.⁷⁵ At the stripper bottoms, the solvent is closer to these conditions than at the higher CO₂ loading conditions, suggesting that it may not be necessary to further limit the reboiler temperature. A better understanding of the degradation within the stripper is needed if further limits on the reboiler temperature were to be implemented.

The lean-rich heat exchanger and absorber trim cooler were included in the stripper Aspen model flowsheet. Both were designed as shell and tube heat exchangers. A 25 °F temperature approach between the rich amine stream from the absorber and the lean amine stream from the stripper was specified for the lean-rich heat exchanger. The approach temperature constraint was implemented in VBA, where Sinter interface would iteratively run and adjust the rich amine outlet temperature until the constraint was met. The amine

trim cooler was designed to cool the lean amine stream back to absorber inlet conditions.

The CO₂ compression unit was modeled using 10 compression stages with 2 intercoolers. The process was designed to compress and dry the CO₂ gas stream from the stripper overhead to pipeline transport conditions: 2215 psi and 100 °F.⁸

4.2.3 Process Performance Parameters

Net power output and capital cost were used in this work as performance metrics for the CO₂ capture process. Net power output was used as the energy metric instead of thermal energy demand in the stripper reboiler because it is a more complete measure of impact on power plant product and includes the pumping and compression costs.⁶⁵ Net power output for the coal power plant with CO₂ capture was calculated as the gross power output from a 550 MW power plant with reduced low pressure steam feed, determined from a surrogate model as described in Eslick and Miller less the energy demands from CO₂ compression and amine circulation.⁷² The model is detailed in Appendix A. The reduced steam feed was determined by calculating the necessary low pressure saturated steam draw at 274.5 kPa to meet the thermal energy demand in the stripper reboiler.

The equipment size and capital cost were determined using Aspen model results and sizing and costing functions for each equipment type from Seider et al.⁷⁶ All materials were assumed to be carbon steel. The capital cost was calculated as the free on board cost using the Lang method, with a CE factor of 550. Solvent cost was not included in the capital cost.

4.2.4 Multi-objective Genetic Algorithm Analysis

As previously discussed, when modeling and comparing performance of a CO₂ capture process using different amine solvents, it is important to model each amine using a set of operating conditions that are best suited for that amine. In this work we selected net power output and capital cost as the optimization variables, and we note that different objectives (e.g. minimization of water usage) may lead to different operating conditions that optimize those objectives. The multi-objective analysis approach used a NSGA-II genetic algorithm to probe the design and operating space with the objective of optimizing the performance parameters. The optimization was implemented in modeFrontier, an optimization and data analysis software package.⁷⁷ The Aspen process models were interfaced with modeFrontier through Excel, using the Sinter simulation interface.^{72,73}

The design objectives were to minimize the capital cost and maximize the net power output of the CO₂ capture process for each amine. Both design and process operating conditions were considered as manipulated variables. The design space for the genetic algorithm is listed in Table 4.2. The genetic algorithm was seeded with 25 cases determined using a Latin hyper cube distribution across the design space and carried out for 150 generations. The work was performed on a 2.93Ghz Core 2 Duo PC and took about a week to finish for each solvent.

Variable [units]	Bounds
Absorber	
Lean amine temp. [K]	[316.5, 333.15]
Lean amine loading [mol CO ₂ /mol amine]	[0.05, 0.35]
Absorber packing height [m]	[4.6, 13.7]
Intercooler draw stage	[23, 32]
Intercooler ΔT [°C]	[0, -10]
Stripper	
Regenerator packing height [m]	[3, 12.2]
Condenser pressure [kPa]	[137.9, 275.8]
Condenser temp. [K]	[316.5, 333.15]
CO ₂ Compression	
Cooler 1 outlet temp. [K]	[311, 322]
Cooler 2 outlet temp. [K]	[311, 322]

Table 4.2: Equipment and process operating optimization variables

4.3 Results and Discussion

4.3.1 Analysis of the MEA Process

The 150 generations of the genetic algorithm for the 11 mol% MEA CO₂ capture process yielded about 3000 converged and feasible Aspen Plus solutions for the CO₂ capture and compression process, each with different design and operating conditions and corresponding capital cost and power output. The cases that did not yield solutions either failed to converge in Aspen or led to infeasible results with the reboiler temperature being greater than the available low pressure steam temperature.

Figure 4.2 shows the results of the converged cases (a few irrelevant cases are outside the boundaries of the figure) leading to higher power output and

lower capital cost. The Pareto front (filled circles) shows the relationship and trade-offs between the two design objectives. There is a minimum capital cost to capturing 90% CO₂ from a 550 MW flue gas stream and a maximum possible net power output given the MEA-CO₂ chemistry and defined process. The Pareto front shows that increasing the plant efficiency comes with increased capital cost, due to larger equipment. However, there becomes a point such that only marginal gains in plant efficiency are seen with additional capital investment. This analysis provides a better understanding of the limitations of the CO₂ capture process and can be utilized in decision making during project design.

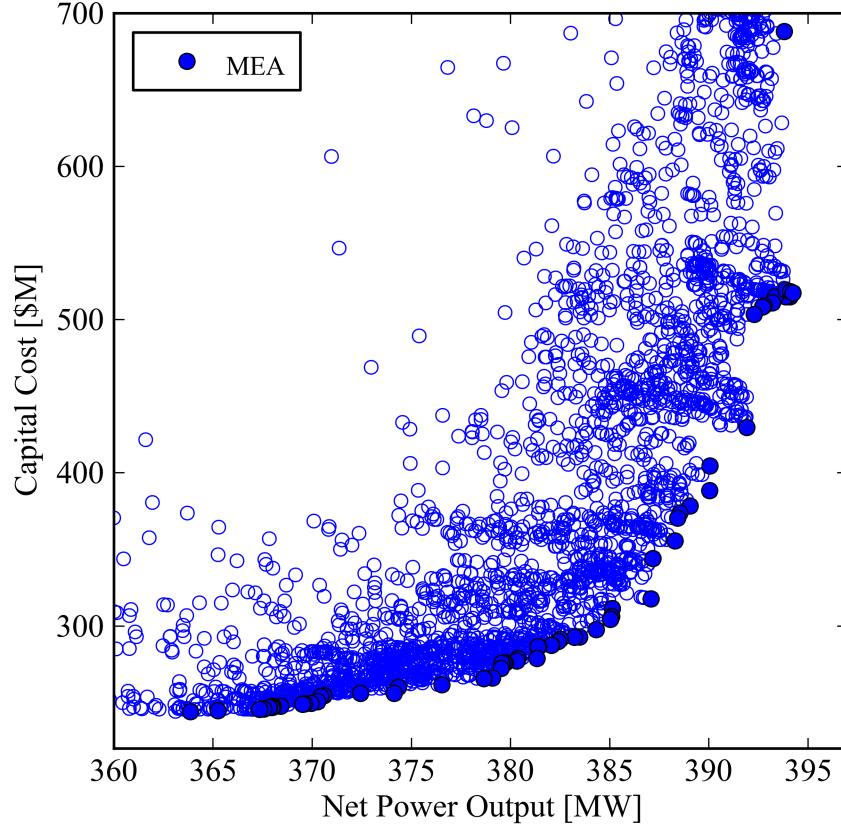


Figure 4.2: Solutions from genetic algorithm analysis for a post-combustion CO_2 capture process using MEA solvent. Pareto front solutions are denoted as filled circles.

Table 4.3 shows two cases that optimized each design variable independently, i.e. maximizing power output, and minimizing capital cost. Case 1 shows that the highest power output is achieved with moderate lean amine CO_2 loading and high stripper condenser pressure. The moderate lean loading is consistent with other parametric studies of lean amine loading on energy demands of CO_2 capture.^{64,69} Additionally, the high stripper operating pressure is consistent with process heuristics.^{65,78}

Results	Case 1	Case 2
Power output [MW]	394.2	363.5
Capital cost [\$M]	517.3	244.1
Reboiler temperature [K]	400	384
Working capacity ($\Delta\alpha$)	0.315	0.222
Model Inputs		
Lean amine temp. [K]	332.5	332.4
Lean amine CO ₂ Loading [n_{CO_2}/n_{amine}]	0.188	0.258
Absorber height [m]	13.56	4.69
Intercooler draw stage	31	24
Intercooler T [°C]	-9.89	-9.89
Regenerator height [m]	12.1	3.17
Condenser pressure [kPa]	222.01	138.58
Condenser temp. [K]	316.6	316.5
Cooler 1 outlet temp. [K]	312.9	311.2
Cooler 2 outlet temp. [K]	311.15	311.03

Table 4.3: Best solutions meeting individual design objectives using MEA in the post-combustion CO₂ capture process. Case 1: Maximum power output, Case 2: Minimum capital cost.

4.3.2 The Effect of Solvent Selection

To emphasize the importance of selecting process operating conditions that are specific to each amine, we performed a single case model evaluation using the operating conditions that led to the highest power output from the MEA analysis (Case 1), substituting MEA with AMP and DEA. The results, presented in Table 4.4, show that both AMP and DEA have a larger negative impact on the power output, though the capital cost for the process is lower in each case. This analysis could lead to the conclusion that MEA is the

superior CO₂ capture solvent (in terms of power output), though AMP is superior in terms of capital cost. However, this may be misleading because no consideration has been made to account for the effects of amine-CO₂ chemistry on the design and operating conditions.

	MEA	DEA	AMP
Power Output [MW]	394	373	364
Capital Cost [\$M]	517	362	353

Table 4.4: Single Aspen Plus process model evaluations of MEA, DEA, and AMP post-combustion CO₂ capture process using equipment and process design specification of Case 1.

Using the genetic algorithm optimization, the design space is sampled to identify the conditions for each amine that optimize the design objectives. For DEA and AMP, unique Pareto fronts were identified for each solvent (Figure 4.3). The relationship between capital cost and net power output using DEA and AMP as the capture solvent is similar to MEA, i.e. there are trade-offs between the two design objectives. Additionally, combinations of design and operating parameters can be identified for both solvents that enable the DEA and AMP systems to capture 90% CO₂ from a 550 MW power plant with a higher net power output and lower capital cost investments compared to MEA.

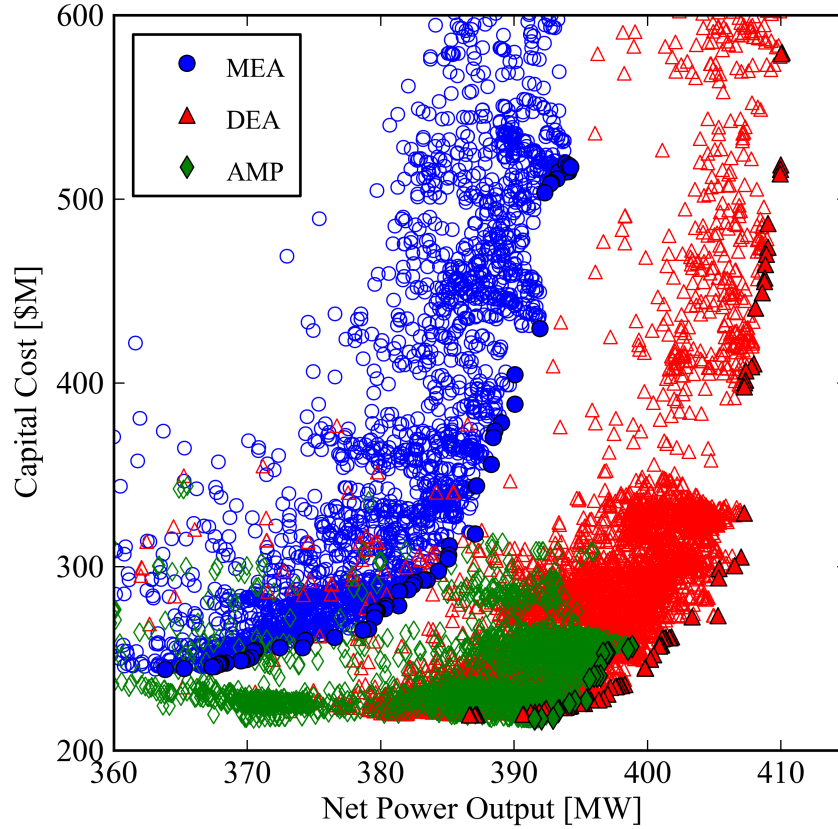


Figure 4.3: Solutions from genetic algorithm analysis for the post-combustion CO_2 capture process using MEA, AMP, and DEA solvents. Pareto front solutions for each amine are denoted with filled symbols.

The gain in power output and reduction in capital cost seen with the CO_2 capture process using DEA and AMP is predominantly due to a lower stripper reboiler heat duty. With a lower heat duty, less steam is required to regenerate the amine, leading to an increase in steam available for power generation (Figure 4.4). Additionally, the lower steam flow rate reduces the size of the kettle reboiler, which dominates the cost of the stripper process (Figure 4.5). These results show that minimizing the reboiler heat duty is a good design

objective for minimizing energy demands and capital cost of the CO₂ capture and compression process.

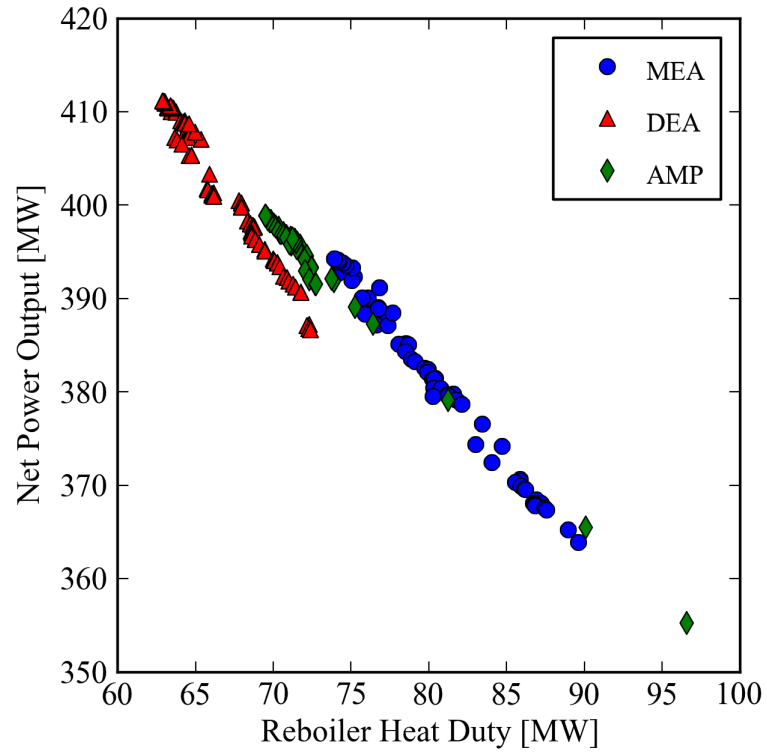


Figure 4.4: Reboiler heat duty [MW] versus net power output [MW] for Pareto front solutions from MEA, DEA, and AMP analysis.

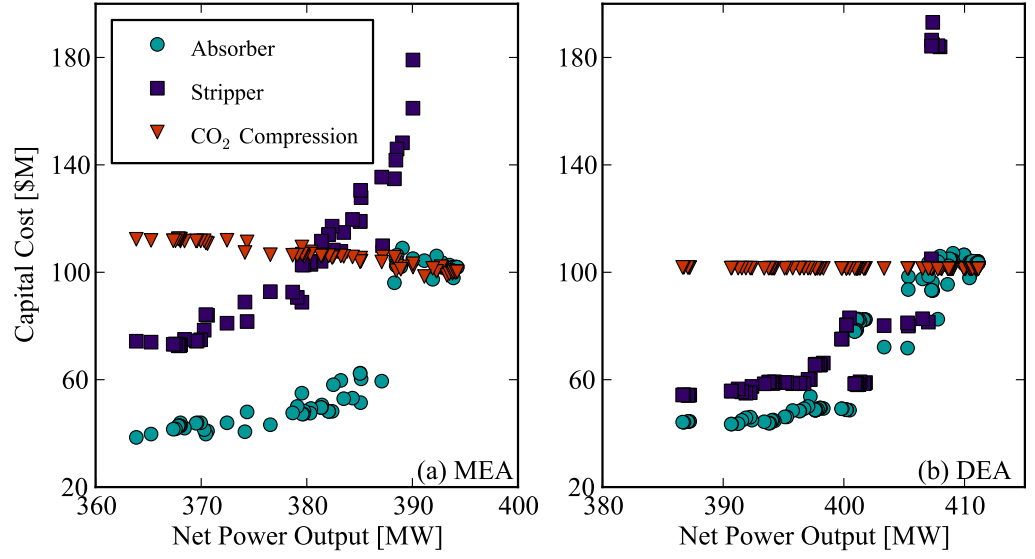


Figure 4.5: Capital cost breakdown of Pareto front solutions for absorber, stripper, and CO₂ compression units for the (A) MEA and (B) DEA CO₂ capture process.

The reboiler heat duty is a measure of the energy required to perform the CO₂-amine separation in the stripper in order to regenerate the amine. The degree of separation is the working capacity of the amine ($\Delta\alpha$)(Equation 4.1). The relationship between the working capacity of the solvent and the reboiler heat duty is shown in Figure 4.6-A.

$$\Delta\alpha = \alpha_{rich\ amine} - \alpha_{lean\ amine} \quad (4.1)$$

$$\alpha_i = \frac{n_{CO_2,i}}{n_{amine,i}}$$

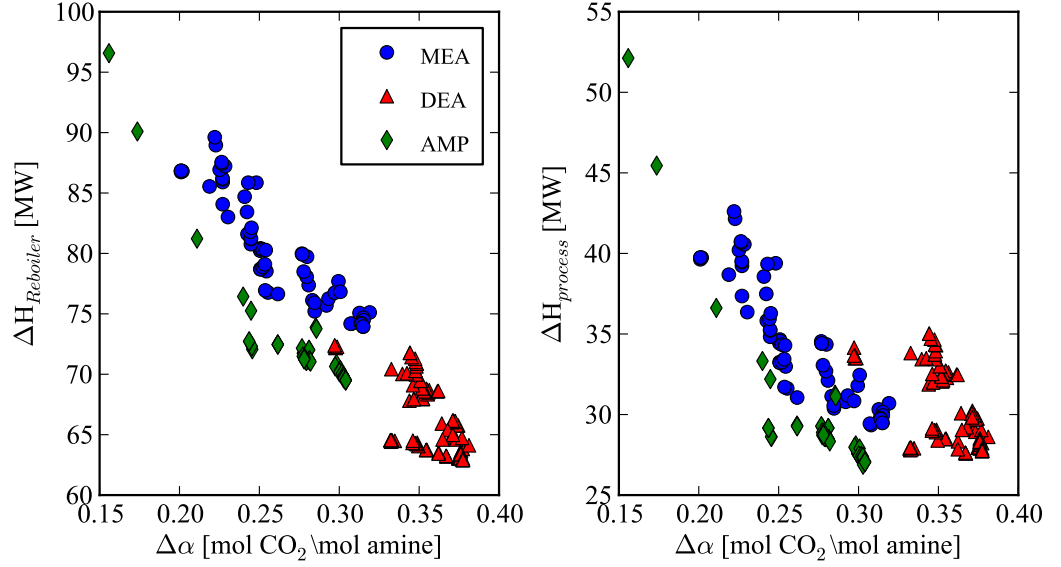


Figure 4.6: (A) Relationship between amine working capacity and total reboiler heat duty for Pareto front solutions of MEA, DEA, and AMP analysis. (B) Relationship between amine working capacity and process enthalpy component of reboiler heat duty (Equation 4.2) for Pareto front solution of MEA, DEA, and AMP analysis.

As discussed previously, the reboiler heat duty accounts for the energy to break the amine CO₂ bonds, as well as the stripping steam and latent heating requirements. Equation 4.2 shows this as the sum of two enthalpies, an enthalpy of reaction and a process enthalpy. Assuming the latent heating requirement is nominal due to heat recovery in the cross heat exchanger, the process enthalpy demands are dominated by the vaporization of water to generate stripping steam.

$$\Delta H_{Reboiler} = \Delta H_{rxn} + \Delta H_{Process} \quad (4.2)$$

Using the experimentally measured reaction enthalpies reported in Chowdhury et al.,⁷⁹ the process enthalpy demands for each solution can be determined (Figure 4.6-B). These results along with what is known experimentally about these amines (Figure 4.7) provide insight to tuning amines in order to minimize the reboiler heat duty.

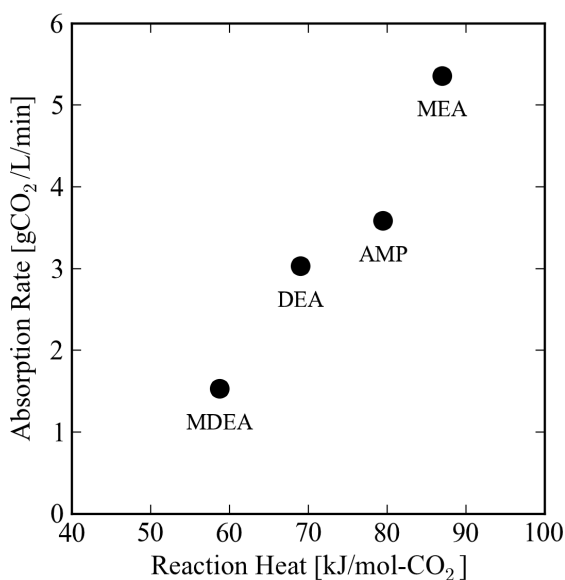


Figure 4.7: Experimentally measured heats of reaction and reaction rates for amine solvents. Adapted from Chowdhury et al.⁷⁹

Amines are known to interact with CO₂ along two pathways, through the formation of a bicarbonate species utilizing a 1:1 amine to CO₂ ratio, and a carbamate pathway with a 2:1 amine to CO₂ ratio. The carbamate pathway has a higher reaction enthalpy than the bicarbonate pathway, and therefore is more energetically favorable. Unhindered primary and secondary amines, like MEA and DEA, interact with CO₂ along both the carbamate and bicarbonate pathway. Tertiary and hindered amines, like AMP, only interact with CO₂ along the bicarbonate pathway.

The results of this study show that the working capacity of DEA is higher than that of MEA at the optimal process conditions and the higher working capacity leads to a lower reboiler heat duty. Since the number of available reacting molecules is constant for all amines in this study, a higher working capacity likely indicates that the carbamate pathway in DEA is less stable compared to MEA, thus favoring the 1:1 bicarbonate pathway. This conclusion is consistent with the heat of reaction presented in Figure 4.7 and stability studies performed by Sartori et al. showing that carbamates are six times less stable in DEA than MEA.¹² Thus, tuning the molecular structure of unhindered amines to destabilize carbamate formation could lead to a lower reboiler heat duty and a more optimal CO₂ capture process.

The AMP results suggest that hindered and tertiary amines fall along a different working capacity reaction enthalpy relationship. Figure 4.7 shows that the reaction enthalpy and kinetics of AMP are close to that of DEA. However, the working capacity of the Pareto front solutions are closer to that of MEA. The single pathway interaction must limit the working capacity of AMP. Although the working capacity of AMP is limited, Figure 4.6-B suggests that AMP requires less stripping steam to regenerate the solvent and therefore the reboiler heat duty is lower. The lower stripping steam demand could also be an artifact of the single interaction pathway. Therefore, if a tertiary or hindered amine could be designed to have a high working capacity like DEA, it may result in a lower reboiler heat duty because of a lower stripping steam demand.

4.4 Conclusion

In this work we presented a methodology to evaluate and compare the performance of different amines as CO₂ capture solvents for a 550 MW power

plant using net power output and capital cost of the CO₂ capture process as performance metrics. Using Aspen Plus to model the process and the NSGA-II genetic algorithm to identify a Pareto front of the the best design and operating conditions for each process that minimized capital cost and maximized power output, we observed a large set of possible solutions. The Pareto front for each amine illustrates the trade-offs between the two conflicting objectives. Additionally, comparing the Pareto fronts of each amine, we see that DEA has the potential to be the best solvent both in minimizing capital cost and maximizing power output, of the MEA, AMP, and DEA, for CO₂ capture. Comparing to the experimental performance of these amines, our results suggest that the added benefits of a lower reaction heat of DEA and AMP outweigh the kinetic penalties associated the lower reaction rates of these amines. Additional studies incorporating reaction kinetics into the process models need to be performed to confirm that relationship.

5 An Overview of Pre-combustion CO₂ Capture Using Physical Solvents

5.1 Process Overview

In addition to addressing CO₂ emissions from traditional coal power generation technologies, lower emissions CO₂ power generation technologies are being developed, including Integrated Gasification Combined Cycle (IGCC) power plants. A schematic of the overall IGCC process is shown in Figure 5.1. In an IGCC plant, a coal feed is partially oxidized in a gasifier to produce synthesis gas (syngas), which is predominantly a mixture of H₂, CO₂, and CO. The syngas is combusted and thermally expanded to generate power. The combined cycle power generation scheme has a 38-47% LHV plant efficiency, which is higher compared to a traditional coal fired power plant (33-37%).⁸⁰ The increased plant efficiency means that power generation with IGCC plants already reduces CO₂ emissions (0.68-0.85 ton CO₂/MWh), compared to pulverized coal plants (0.9-1 ton CO₂/MWh).⁸⁰ Additionally, IGCC can be coupled with a pre-combustion CO₂ capture process that can further reduce emissions.

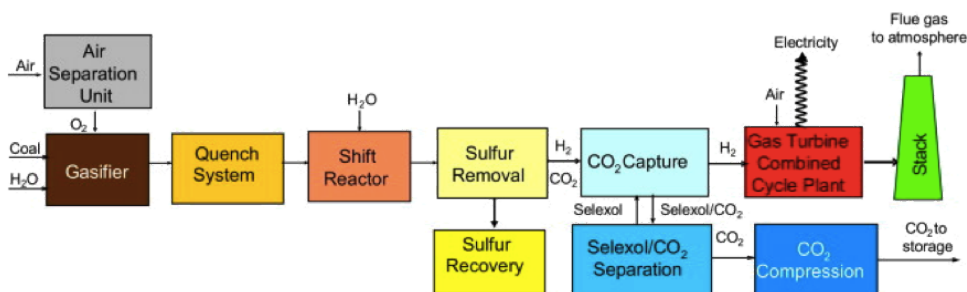


Figure 5.1: Block diagram of IGCC process.

In a pre-combustion capture process, CO_2 is removed as part of the acid gas clean-up process, prior to syngas combustion as shown in Figure 5.2. CO_2 capture can be integrated with the H_2S removal process by either coupling them or removing the acid gases in series. The schematic in Figure 5.2 represents the later CO_2 capture scenario, in which H_2S is removed prior to CO_2 capture. The syngas entering the CO_2 removal process is at low temperature, high pressure, up to 50 bar, and approximately 38-45 mol% CO_2 and 50-55 mol% H_2 .^{8,81} Given the high partial pressure of CO_2 , physical solvents can be used to separate CO_2 from the syngas stream. Additionally, physical solvents possess a process advantage over chemical solvents, like those used in the post-combustion capture process, because they can be regenerated with a pressure reduction instead of a thermal regeneration. The syngas enters the pressurized absorber and comes into contact with the solvent and CO_2 is absorbed into the solvent. The H_2 leaves the absorber overhead and is sent to the power generation cycles. The CO_2 rich solvent leaves the absorber bottoms and is regenerated with a multi-stage flash and cycled back to the absorber. The CO_2 can be dried and compressed for pipeline transportation using the process described in Chapter 2.1 (Figure 2.3).

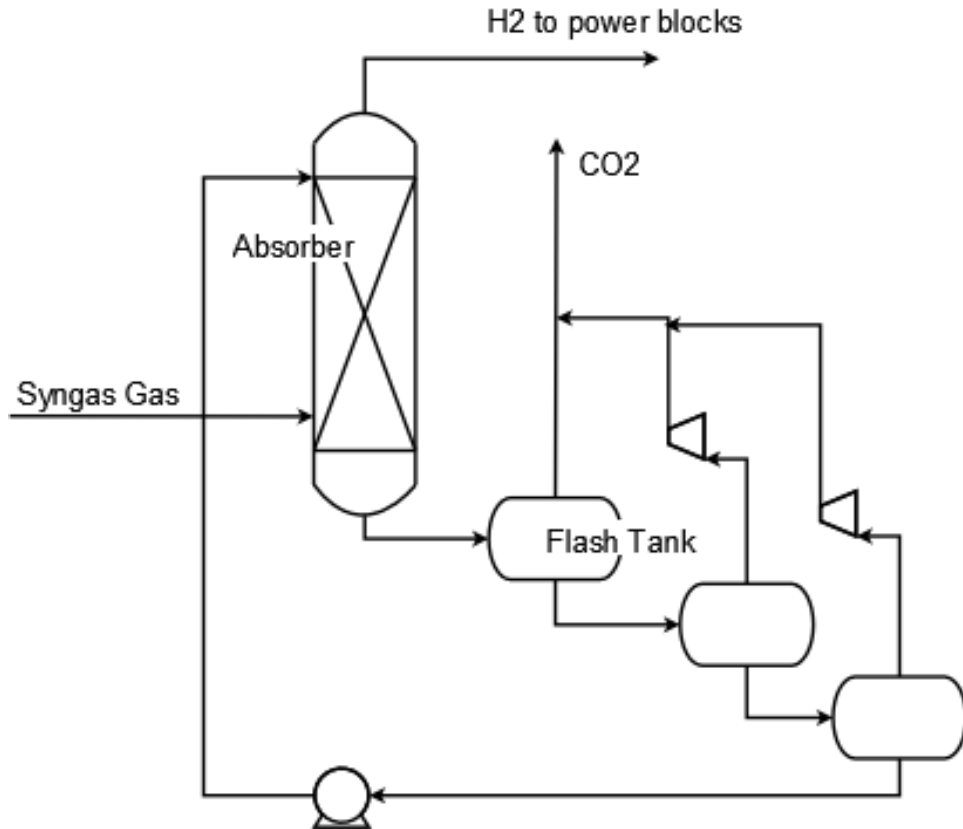


Figure 5.2: Process flow diagram of pre-combustion CO₂ capture process using a pressure swing to regenerate the solvent. Adapted from Rubin et al.²

Process analysis of baseline IGCC plants and plants with CO₂ capture using Selexol[®], the leading commercial solvent, suggest that the inclusion of a CO₂ capture process only reduces the overall plant efficiency by 7-8 percentage points,⁸² which is minor compared to the inclusion of a post-combustion CO₂ capture process in a pulverized coal plant. However, due to the high capital costs of IGCC power plants, marginal changes in plant efficiency have a large impact on plant economics. Although some additional equipment for CO₂ capture is required, the heavy emphasis of research and development efforts

are focused on reducing the overall energy penalty of CO₂ capture, which may be reduced through the development of new solvents.

5.2 Advancements of Physical Solvents for Pre-combustion CO₂ Capture

The leading commercial process for pre-combustion CO₂ capture uses Selexol[®], a mixed molecular weight polyethyleneglycol dimethylether. Selexol[®] has many desirable properties that are advantageous for the acid gas removal process. It has good selectivity of H₂S and CO₂ over H₂, low volatility, and low viscosity. However, solvent development is focused on addressing some of the inefficiencies associated with Selexol[®], namely decreased CO₂ solubility at high temperatures and hydrophilicity.

Commercial processes using Selexol[®] typically operate below 40 °C because the solubility of acid gases drops substantially at high temperatures. The syngas leaving the upstream gas processing units is about 240 °C and must be cooled substantially before the acid gas removal process. Not only is it inefficient to cool the syngas to the operating temperature of Selexol[®], because it requires an additional utility, but the lower CO₂ capture temperature reduces the maximum pressure of the captured CO₂ and consequently increases the CO₂ compression work. Developing solvents that can achieve good CO₂ solubility at higher temperatures, while maintaining the other desirable properties of an acid gas removal solvent, will increase the efficiency of the IGCC plant with CO₂ capture.

Hydrophobic solvents could also boost the efficiency of an IGCC plant with CO₂ capture by increasing the mass of the syngas stream entering the gas turbine. As previously stated, the syngas is a mixture of H₂, CO₂, and CO, prior to CO₂ capture. In order to maximize the CO₂ captured from the power

plant, the CO must be completely oxidized to CO₂. This is typically done with a water-gas shift reaction, upstream of the acid gas removal process, and leaves the syngas stream entering the acid gas removal unit saturated with water. Although this is an additional process required only in the case of CO₂ capture, the increased mass of the syngas stream due to the additional water could increase the power generation in the gas turbine. However, water is completely soluble in Selexol[®], and therefore is removed from the syngas stream in the processes of removing the other gases. In addition to reducing the power generation potential of the syngas, the water uptake by Selexol[®] increases the work of the CO₂ compression unit.

A wide range of materials has been proposed as advanced physical solvents for pre-combustion capture to address the inefficiencies associated with Selexol. This includes CO₂-philic oligomers, similar in molecular structure to Selexol with hydrophobic groups introduced in the monomer unit, and room temperature ionic liquids. Both classes of materials, offer many possibilities with fictionalization to tune interactions with CO₂. As with developing post-combustion solvents, understanding the structure-performance relationships of physical solvent-CO₂ systems can aid in the direction of solvent design and research. The following chapter presents a Raman spectroscopy study of CO₂-philic oligomers and room temperature ionic liquids to elucidate structure-performance relationships and quantify CO₂ solubility in these solvents. Using process models these relationship can be connected to process performance to understand the impact of solvent selection on the pre-combustion CO₂ capture process and guide the direction of solvent design.

6 Characterization of CO₂-Physical Solvent Systems Using Raman Spectroscopy

6.1 Introduction

Two leading classes of solvents, CO₂-philic oligomers and room temperature ionic liquids, have been proposed as advanced pre-combustion CO₂ capture solvents with the potential of lowering the overall parasitic energy impact of the process on Integrated Gasification Combined Cycle power generation.^{78,83-89} Oligomer systems similar in structure to Selexol[®], the leading commercial solvent, offer the possibility of comparable, or enhanced, CO₂ solubility and more desirable properties like hydrophobicity through modifications to the monomer backbone, termination units, and number of repeat units to tailor the solvent for CO₂ capture. Ionic liquids are low-melting salts and have gained a lot of attention as CO₂ capture physical solvents because of their non-volatile nature, high solubility of CO₂, and large range of tunability of both the cation and anion of the system.^{78,89}

Miller et al. have studied a wide variety of CO₂-philic oligomers, including glycols, glycerols, and silicone with 3-6 repeat units, which are similar in molecular structure to Selexol[®].^{83,84} Using bubble point measurements to determine the pressure-composition phase behavior of CO₂ with these solvents, they found polydimethylsiloxane (PDMS), branched monomer polypropyleneglycol dimethylether (PPGDME), branched monomer polybutyleneglycol diacetate, and linear monomer polybutyleneglycol diacetate to have comparable CO₂ solubility to Selexol[®]. Viscosity and water solubility measurements were also carried out on these solvents. The viscosity of PPGDME was found to be 6 cP, equivalent to that of Selexol[®], while the viscosity of PDMS was found to be 3 cP. The other

solvents showed much higher viscosities, which is undesirable from a process standpoint. Additionally, PDMS was found to be fully immiscible with water and PPGDME was only slightly miscible with water, solvating 0.021 g H₂O/g of solvent. These measurements, along with the comparable CO₂ solubility to Selexol[®], showed PPGDME and PDMS to be the most promising as CO₂ capture solvents of those studied.

With ionic liquids (ILs) there has been extensive experimental work measuring the solubility of CO₂ and other gases for a large combination of anion-cation pairs.^{88,90-96} The choice of cation has only a minor impact on CO₂ solubility. Aki et al. showed that increasing the alkyl chain length of the 1-alkyl-2-methylimidazolium cation increased CO₂ solubility slightly on a mole fraction basis.⁹² Muldoon et al. and Anderson et al. showed that the solubility of CO₂ is independent of cation type unless the cation gives a strong interaction with the anion, as seen when comparing [hmim][Tf₂N] and [choline][Tf₂N].^{87,94} Molecular modeling and infrared spectroscopy have shown that solvated CO₂ predominantly interacts with the Lewis base site on the anion, substantiating Muldoon's conclusion that the effect of the cation is only to inhibit interaction between CO₂ and the anion.⁹⁷ Although the Lewis acid-base interaction is likely, the solubility of CO₂ does not correlate with the basicity of the anion and is further enhanced with fluorinated anions.⁹⁴

The development of new physical solvents requires a clear understanding of the mechanism of CO₂ solvation and the structure-CO₂ solubility relationship of these solvents. Additionally a measure of CO₂ solubility in the candidate solvent at CO₂ capture conditions is necessary in the development of new solvents. Many techniques for measuring gas solubility require mL sample values, which could be problematic for new materials being synthesized at the

bench scale.^{83,94,98} Additionally these techniques cannot provide molecular interaction information about the gas-solvent system.

This chapter presents a Raman spectroscopy study of CO₂-solvent systems of CO₂-philic oligomers and 1-alkyl-2 methylimidazolium based ionic liquids at pressure conditions relevant to pre-combustion CO₂ capture applications to build that understanding. A microliter Raman assembly was designed to minimize the solvent volumes used for the experiments. Comparisons of the clean solvent, gas phase CO₂, and CO₂-solvent Raman spectra provide a qualitative understanding of the changes that occur with CO₂ and the solvent upon CO₂ solvation and may give some insight to the CO₂-solvent interactions present. Additionally, a technique to extract quantitative information from the Raman experiments to quantify solubility of CO₂ in the physical solvents was developed. From the analysis, a Henry's law constant was determined using small volumes of solvent, with results that are comparable to results obtained from traditional VLE experiments. Although the work presented here specifically addresses challenges in characterizing pre-combustion CO₂ capture solvents, the approach is general and could be used for other Raman active gases.

6.2 Materials and Methods

6.2.1 Materials

Figure 6.1 shows the oligomer solvents examined in this work. We studied: Selexol[®], a proprietary CO₂-selective solvent that is rich in polyethyleneglycol dimethylether (PEGDME), a known molecular weight PEGDME, a branched polypropyleneglycol dimethylether (PPGDME) at two molecular weights, and polydimethylsiloxane (PDMS, also referred to as silicone oil) at three molecular weights. PPGDME and PDMS were selected

based on structural similarity to Selexol[®] and their observed immiscibility with water.⁸³ Selexol[®] was purchased from Univar USA Inc. and used as received. PEGDME (average molecular weight 250) was purchased from Sigma Aldrich, and filtered once with activated carbon before using. The samples of PDMS were purchased from Geleste and used as received.

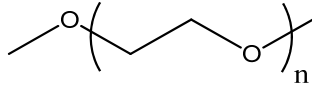
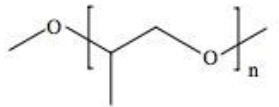
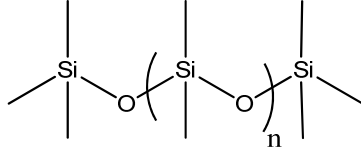
Name	Abbreviation	Molecular Structure
poly(ethyleneglycol) dimethylether	PEGDME	
poly(propyleneglycol) dimethyleth	PPGDME	
poly(dimethylsiloxane),	PDSM 550	

Figure 6.1: Molecular structure of oligomer solvents studied in this work.

Figure 6.2 shows the 1-alkyl-3- methylimidazolium ($[C_n\text{mim}][\text{Tf}_2\text{N}]$) ionic liquids studied in this work. 1-ethyl-3-methylimidazolium bis(trifluoromethylsulfonyl)imide ($[\text{emim}][\text{Tf}_2\text{N}]$), 1-butyl-3-methylimidazolium bis(trifluoromethylsulfonyl)imide ($[\text{bmim}][\text{Tf}_2\text{N}]$), 1-hexyl-3-methylimidazolium bis(trifluoromethylsulfonyl)imide ($[\text{hmim}][\text{Tf}_2\text{N}]$), and 1-ethyl-3-methylimidazolium tetrafluoroborate ($[\text{emim}][\text{BF}_4]$) were purchased from Sigma Aldrich and used as received. 1-ethyl-3-methylimidazolium tetracyanoborate $[\text{emim}][\text{TCB}]$ and 1-ethyl-3-methylimidazolium tris(pentauroethyl)triurorophosphate $[\text{emim}][\text{FAP}]$ were purchased from

EMD chemicals and were used as received. CO₂ gas was purchased from Matheson Gas with 99.5% purity and used without further purification.

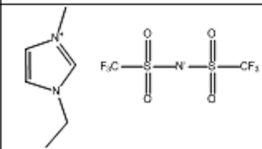
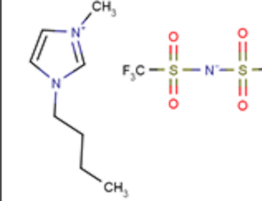
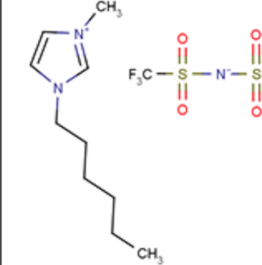
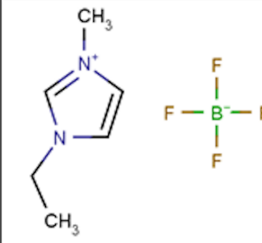
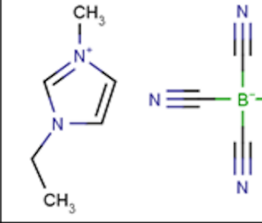
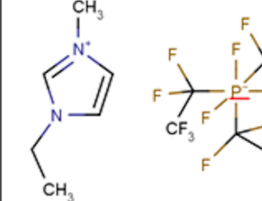
Name	Abbreviation	Molecular Structure
1-ethyl-3-methylimidazolium bis(trifluoromethylsulfonyl)imide	[emim][Tf ₂ N]	
1-butyl-3-methylimidazolium bis(trifluoromethylsulfonyl)imide	[bmim][Tf ₂ N]	
1-hexyl-3-methylimidazolium bis(trifluoromethylsulfonyl)imide	[hmim][Tf ₂ N]	
1-ethyl-3-methylimidazolium tetrafluoroborate	[emim][BF ₄]	
1-ethyl-3-methylimidazolium tetracyanoborate	[emim][TCB]	
1-ethyl-3-methylimidazolium tris(perfluoroalkyl)trifluorophosphate	[emim][FAP]	

Figure 6.2: Ionic liquid solvents studied in this work.

6.2.2 Experimental Apparatus for Raman Spectroscopy Measurements of High Pressure Gas-Solvent Systems

We developed a microliter sample volume apparatus for Raman spectroscopy measurements of gas-solvent systems at pressures up to 60 bar (Figure 6.3). The apparatus consist of a round fused silica capillary, the solvent sample carrier, epoxied to a stainless steel high-pressure Swagelok® system, the gas carrier. The microliter sample size volume is beneficial when studying novel solvents, since it is challenging to synthesize large volumes during initial development. Similar sample cells have been used in geothermal literature when studying fluid phase equilibrium in geological environments.⁹⁹

The fused silica capillary solvent sample cell was approximately 4 cm in length with 350 μm ID/450 μm OD (Polymicro Inc. LLC). As purchased, the surface of the capillary is coated with a polyimide layer to increase durability. The polyimide coating produces a strong fluorescence signal in the Raman spectra overpowering the signal from any sample inside the capillary. A butane torch was used to remove 3 cm of the polyimide coating, leaving a clean fused silica section of capillary, with one end clear and the other still coated with a polyimide layer.

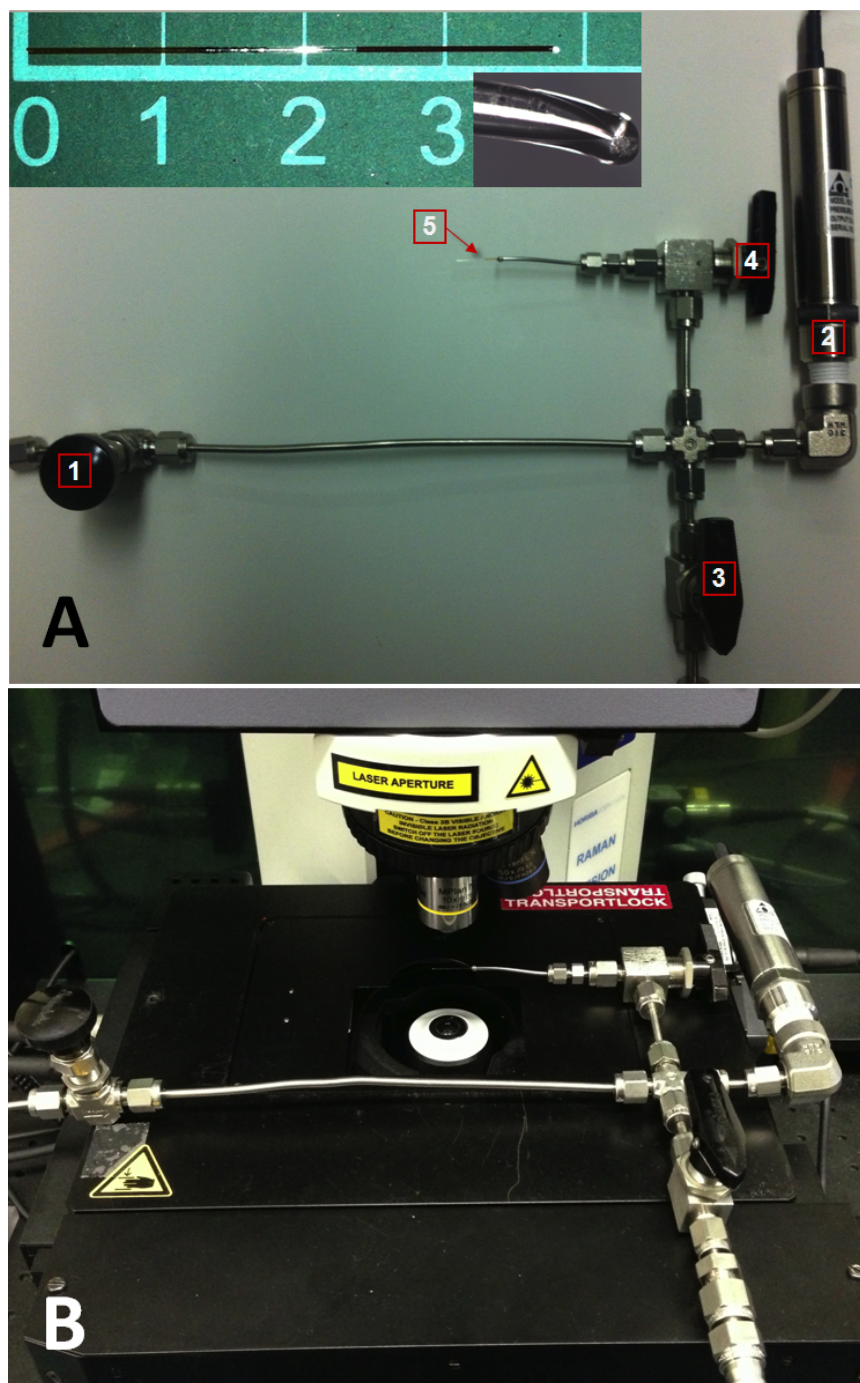


Figure 6.3: (A) Overhead view of high-pressure assembly: (1) Gas inlet valve (V1), (2) pressure sensor, (3) pressure release valve/vacuum line connection (V2), (4) solvent exposure valve (V3), (5) capillary. Inset figures show capillary filled with colored sample and fused end of capillary under 10X objective. (B) High pressure assembly positioned on motorized microscope stage.

The capillary was filled with solvent from the polyimide coated end by dipping that end into a drop of solvent, 1 μ L, on a clean glass slide. Using capillary action, this drew in 1-1.5 cm (in length) of solvent. For volatile and/or highly non-viscous solvents, to prevent evaporation or movement of the solvent drop in the capillary, the polyimide end was sealed with hot wax. Care was taken to move the solvent in the capillary away from the capillary opening to prevent mixing between the wax and solvent at the opening.

The clear end of the capillary was fused using a small flame tip oxy-acetylene torch. When sealing the clear end, the solvent was sufficiently far from the flame tip to avoid thermal decomposition of the solvent. The fused capillary was then centrifuged to remove the air trapped between the solvent and the fused end, resulting in all of the solvent at the fused end of the sample cell and approximately a 2.5 cm window between the solvent-air interface and the opening of the capillary (Figure 6.3-A).

The polyimide coated open end of the sample cell was epoxied to a 1/16 in. stainless steel tubing. Once fully cured, the tubing was connected to the rest of the high pressure assembly. The system was pressurized from the CO₂ gas tank with a maximum delivery pressure of 60 bar, which was limited by the CO₂ tank pressure. The CO₂ entered the system through V1 and was exposed to the solvent sample by opening V3 (Figure 6.3-A). The pressure was measured using an in-line Omega[®] PX409USB pressure sensor. The high-pressure assembly was placed on a motorized microscope stage, which enabled the sample to move in the x, y, z direction relative to the microscope objective during the experiments (Figure 6.3-B).

6.2.3 Overview of Raman Spectroscopy

Raman spectroscopy is a technique used to study the molecular vibrational modes present in a system by detecting the inelastic scattering that arises from an excitation event. When applying an energy source, like a laser, to a system many absorption and excitation events can occur. Some of the applied energy, or photons, will excite the system to a short-lived virtual energy state. In this occasion, most commonly, the system will relax in an elastic manner back to its initial energy state, and give off a photon equal in energy to that of the incident photon (Figure 6.4). This is known as Rayleigh Scattering. The system can also relax in an inelastic manner to a different energy state and the resulting photon will have an energy different than that of the incident photon. This is known as Raman scattering. The energy difference between the incident and resulting photon corresponds to the energy difference of the final and initial energy states, which is the energy of the vibrational mode that was excited. Mapping these inelastic relaxations over an energy range results in the Raman spectrum of the system.

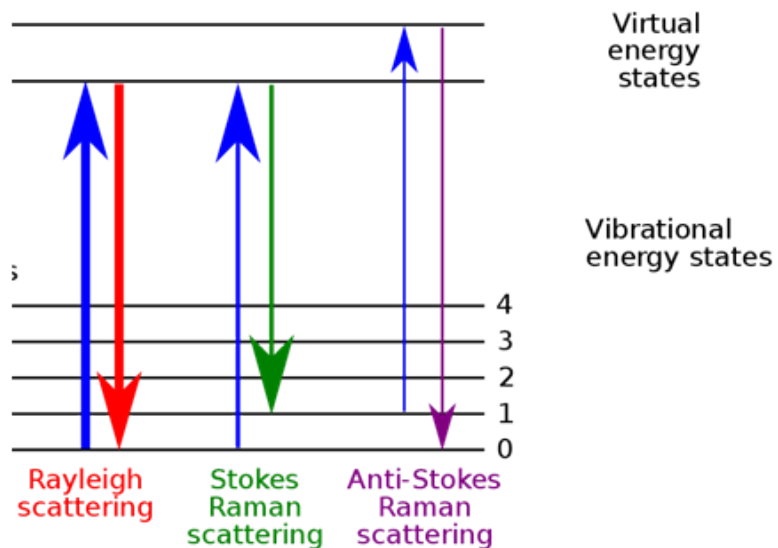


Figure 6.4: Energy diagram of Rayleigh and Raman Scattering. Two types of Raman scattering can occur, either Stokes or anti-Stokes, and depend on the initial energy state of the system. Stokes scattering is the more common of the two, since systems are more likely to be in the ground state prior to excitation.

The physics behind the Raman effect dictate that only vibrational modes that lead to a change in the polarizability of the molecule can be detected with this technique.¹⁰⁰ For many systems, this selection rule complements the selection rules of infrared spectroscopy, where only vibrational modes that change the dipole moment of the system are detected. For example, CO_2 has three distinct vibrational modes, and only the symmetric stretch mode is Raman active and the remaining two are IR active (Figure 6.5).

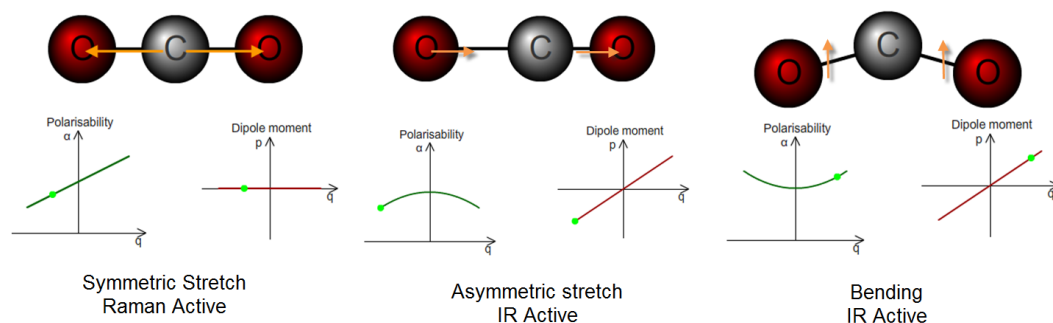


Figure 6.5: Raman and IR activity of the 3 vibrational modes of CO_2 (bending mode is degenerate). Adapted from www.doitpoms.ac.uk/tlplib/raman/active_modes.php

Raman spectroscopy is more commonly used as a qualitative probe of the molecular vibrations in a system. However, the measured Raman intensity also holds quantitative information about the sample.¹⁰¹ Equation 6.1 shows a simplified relationship between the measured Raman intensity of vibration j of an analyte, $I_{R,j}$, and system variables: the incident laser intensity (I_0) and Raman focal length (dz) and sample variables: Raman scatter cross-section of analyte (σ_j) and concentration of analyte in the sample (c_j).

$$I_{R,j} = I_0 dz \sigma_j c_j \quad (6.1)$$

6.2.4 Experimental Procedure for Raman Spectroscopy Measurements of the Gas and Liquid Phase

As shown in Equation 6.1, the intensity of a Raman spectrum depends on the focal length of the measurement. The optimal focal length will maximize the intensity of the spectrum. For a thin sample, i.e. a film on a slide, there is

only a small window in the focal length in which a spectrum can be obtained without introducing signal from the sample carrier, so the optimal focal length is easy to discern. However, in this work the sample carrier was a 350 μm inner diameter fused silica capillary, giving depth to the sample. With this geometry, a spectrum of the sample could be obtained when focused on the top of the capillary as well as anywhere within the depth of the capillary, thus leading to the question of what is the optimal focal length for the sample and could it be determined consistent for each measurement.

Using the motorized microscope stage, a z-position (perpendicular to the axial direction of the capillary) spectral scan was performed of [emim][Tf₂N], taking a spectrum of the sample every 5 microns. Figure 6.6 shows the spectra obtained from the S-N-S stretch mode. The inset plot shows the intensity of the peak at 746 cm^{-1} over the range of z-positions scanned. The position that maximizes the Raman intensity was selected as the optimal focus position for the sample. A scan was performed for each measurement to identify the optimal focus position and ensure consistency in the manner in which Raman measurements were made.

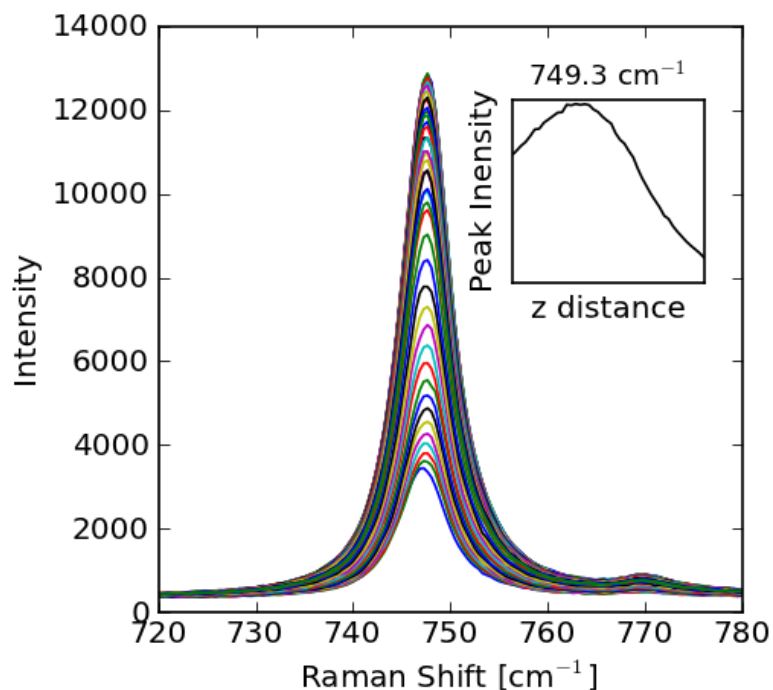


Figure 6.6: Raman band of S-N-S stretch mode of [emim][Tf₂N] from z-position scan of sample in capillary. Inset figure: Absolute band intensity of S-N-S stretch mode as a function of z-position.

All Raman spectroscopy experiments were carried out on a Horiba LabRamHR spectrometer using an 1800 grooves/mm grating, giving a 0.5 cm⁻¹ spectral resolution. The excitation source was a Spectra Physics 532 nm Nd:Yag laser, with an operating power of 0.2 Watts. Raman spectra were taken using an Olympus 50xLWD objective of the gas and liquid phase in the sample cell at atmospheric conditions and CO₂ pressures ranging from 2.5 to 40 bar at 295 K. The solvent was exposed to CO₂ for 45-60 minutes to allow the liquid region close to the gas-liquid interface to equilibrate before measurements were made. To measure the gas phase spectrum, the laser was focused along the axial direction of the sample cell capillary, 450 μm above

the gas-liquid interface. The z-position focus was selected as the position that yielded the highest CO₂ Raman peak intensity from a z-axis Raman spectra scan of the system.

To measure the liquid phase spectrum, the laser was focused in a similar manner to the measurement of the gas phase, with the laser positioned 50 μm below the gas-liquid interface. Spectra were collected at a single window at 1050-1450 cm^{-1} for all pressures. Additionally, at system pressures of 10, 20, and 40 bar a multiple window spectrum of the solvent was taken spanning 500-3300 cm^{-1} . All spectra were recorded as eight averages of one second exposures to increase the signal to noise ratio.

The spectrometer was calibrated at the beginning of each experiment using a silica standard. Additionally, at each CO₂ pressure a single window 1050-1450 cm^{-1} spectrum was taken of an external standard, naphthalene, was also taken. The sharp Raman peak of naphthalene at 1382.2 cm^{-1} was used to calibrate the peak positions in the gas and solvent phase spectra.¹⁰²

6.2.5 Data Analysis of the CO₂ Peak

The total CO₂ peak intensity and position are important in the analysis of the solvated CO₂ spectrum. To determine these values for any peak, the Raman spectrum in the shift region of the peak is fitted with a cubic spline function. The peak center, ν_i , was defined as the Raman shift at the maximum of the cubic spline fit. The peak area was defined as the integral of the cubic spline fit over the Raman shift range of the peak. To analyze the solvated CO₂ peak analysis, the background solvent spectrum was first subtracted.

The calibrated center of the CO₂ Raman peak ($\nu_{CO_2}^*$), or peak position, was determined using Equation 6.2, the peak center center from the raw spectra, and the peak center of the naphthalene peak, $\nu_{naphthalene}^{1382.2}$.

$$\nu_{CO_2}^* = \nu_{CO_2} + (1382.2 - \nu_{naphthalene}^{1382.2}) \quad (6.2)$$

6.3 Results

6.3.1 Raman Spectra of Gas Phase CO₂

Recall, CO₂ has three distinct vibrational modes: symmetric stretch (ν_1), bending (ν_2), and anti-symmetric stretch (ν_3) and only the symmetric stretch mode is detectable through Raman spectroscopy. The Raman spectrum of CO₂ appears as two Fermi diad peaks at 1285 cm⁻¹ (lower band) and 1388 cm⁻¹ (upper band) due to a Fermi resonance of the ν_1 mode with the ν_2 mode.^{103,104} As seen in Figure 6.7, as CO₂ pressure increases the intensity of the Raman peaks also increases. At higher CO₂ pressure, two smaller hot bands appear outside the Fermi diad peaks. The relative intensity split and peak position of the Fermi diad peaks is constant for the pressure range considered in this work.¹⁰⁵

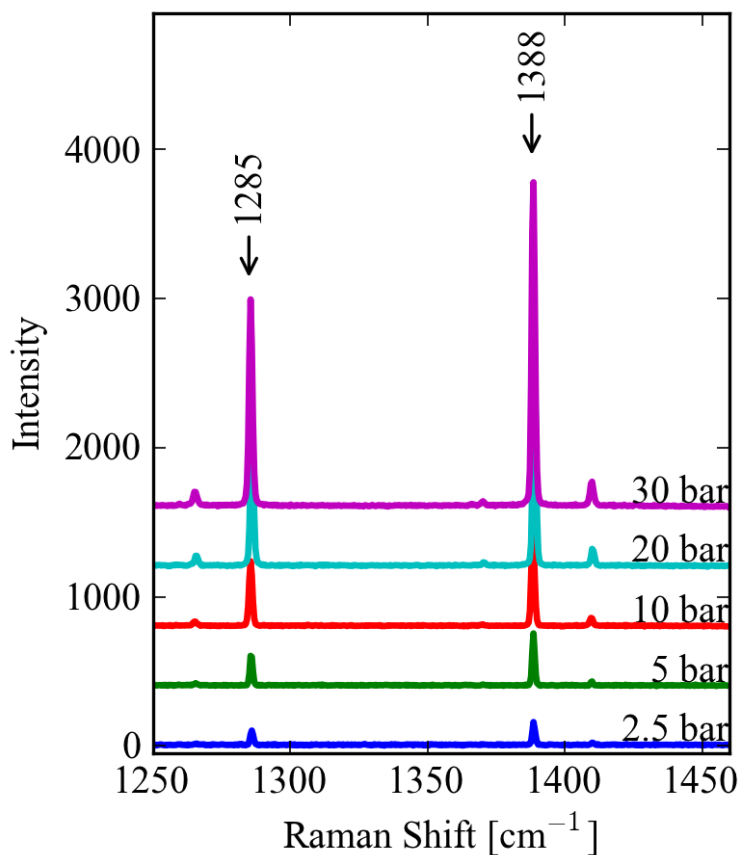


Figure 6.7: Raman spectra of CO₂ gas at 2.5 to 30 bar and 295 K. The Fermi diad peaks are annotated at 1285 cm⁻¹ (lower band) and 1388 cm⁻¹ (upper band). The measured intensity, not normalized intensity, is displayed to illustrate the relationship between CO₂ pressure and intensity.

6.3.2 Raman Spectra of CO₂-Oligomer Solvent Systems

The spectra of Selexol[®] in equilibrium with atmospheric conditions up to 20 bar of CO₂ are shown in Figure 6.8. Comparing the spectra of the solvent in equilibrium with CO₂ to the spectrum at atmospheric conditions, a peak at 1380 cm⁻¹ appears, even at low pressures. At higher pressures, a peak at 1282 cm⁻¹ also appears in the spectra. These peaks are assigned to the Fermi diad

peaks of CO₂ dissolved in the solvent. The upper band is dominant, while the lower band is obscured by the solvent spectra. No additional peaks appear in the CO₂-Selexol[®] system over the Raman shift range studied (500 cm⁻¹-3200 cm⁻¹).

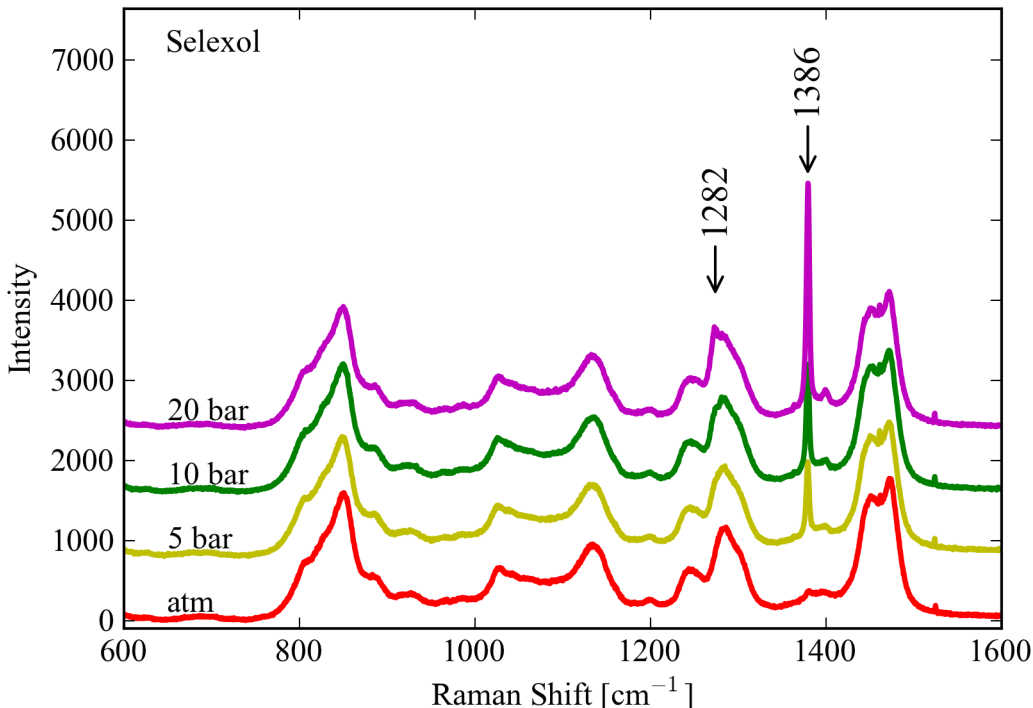


Figure 6.8: Raman spectra of Selexol[®] at atmospheric conditions and equilibrium with 5 to 20 bar CO₂ at 295 K. Arrows markers denote Fermi diad peaks of CO₂.

Besnard et al. and Cabaço et al. have published Raman spectroscopic studies of CO₂ dissolved in other physical solvents, including acetone, ethanol, benzene, and [bmim][TFA] at pressures from 1 to 100 bar CO₂.^{106–108} Similar to this work, they observed peaks near 1278 cm⁻¹ and 1382 cm⁻¹. In the spectra of acetone, ethanol, and benzene, they also observed a peak at 650 cm⁻¹ starting at 10 bar CO₂. They attribute this peak to the bending mode of CO₂, which

as previously discussed is not Raman active in a linear CO₂ molecule. The appearance of the bending mode in the Raman spectrum suggests that some of the dissolved CO₂ is in a slightly bent geometry due to weak interactions with the Lewis base sites of those solvents. From additional analysis of the CO₂ Fermi diad peaks, they showed that both the upper and lower band can be decoupled into two peaks, also indicating the presence of two geometries of CO₂ solvated in the systems, a linear CO₂ and an interacting slightly bent CO₂.

Infrared spectroscopy studies of CO₂-polyethylene glycol systems show evidence of similar behavior between CO₂ and the PEG solvents as reported by Besnard et al. and Cabaço et al. with acetone, ethanol, benzene systems. At high CO₂ pressures, deformations in the IR peaks associated with the C-O stretch vibrational mode of the ether backbone were observed, suggesting that CO₂ interacts weakly with the lewis base sites of the backbone.^{109–111} The corresponding Raman shift for the C-O stretch mode of the ether backbone is 1130 cm⁻¹.^{112,113} The analysis of this peak in the CO₂-Selexol[®] does not show any deformations. This, along with absence of any new Raman peaks in the CO₂-Selexol[®] other than the Fermi diad peaks, suggests that at pressures up to 40 bar there is no interaction between solvated CO₂ and PEGDME or the concentration of interacting CO₂ is too low to detect using Raman spectroscopy.

The spectra of CO₂-PPGDME-430, and CO₂-PDMS-550, are show in Figure 6.9 and Figure 6.10 respectively. The spectra of these systems show similar behavior to the CO₂-Selexol[®] system. Compared to the solvent spectra at atmospheric conditions, only the Fermi diad peaks of the CO₂ symmetric stretch mode appear in the CO₂-solvent spectra. With the PDMS system, the intensity of the solvent spectra is in the CO₂ Raman shift region

(1270 cm^{-1} - 1390 cm^{-1}) and both Fermi diad peaks are visible in the CO_2 -PDMS spectra at low pressures. These spectra also show no indication of CO_2 interaction with the solvent. Corresponding spectra of the remaining CO_2 -oligomer solvent systems are shown in Appendix B.

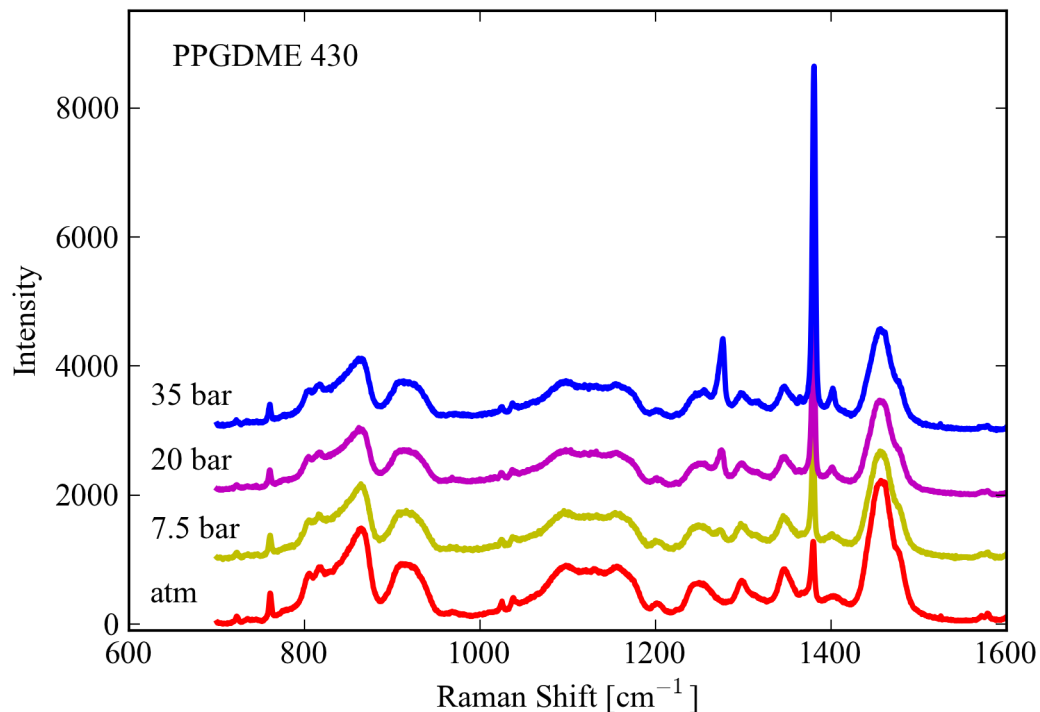


Figure 6.9: Raman spectra of PPGDME, MW 430, at atmospheric conditions and equilibrium with 5 to 40 bar CO_2 at 295 K.

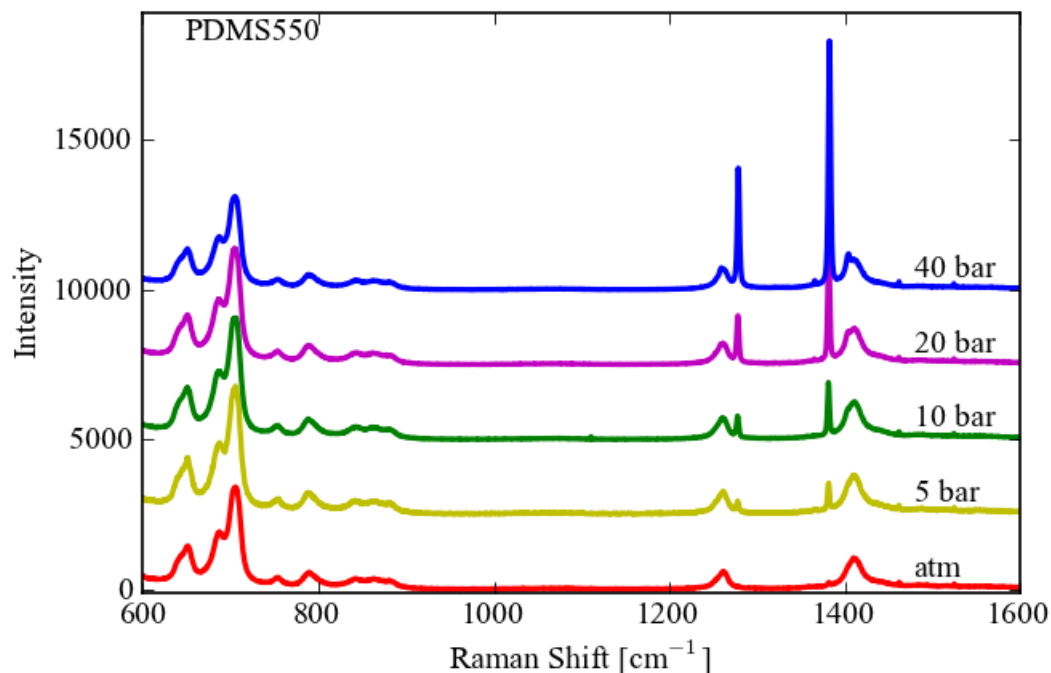


Figure 6.10: Raman spectra of PPGDME, MW 550, at atmospheric conditions and equilibrium with 5 to 40 bar CO_2 at 295 K.

6.3.3 Raman Spectra of CO_2 -Solvent-Ionic liquids

Solubility studies of CO_2 in ionic liquids have shown that CO_2 interacts with the anion of the IL.⁹⁴ Additionally, since the interaction is enhanced with fluorinated anions, likely CO_2 interacts with the fluorine groups.^{87,92} DFT studies of these systems also show the interaction to be with the anion of the IL, specifically with the Lewis base site, resulting in a slightly bent CO_2 geometry.¹¹⁴ Evidence of this interaction has been seen in IR studies of $[\text{emim}][\text{BF}_4]$ and $[\text{emim}][\text{PF}_6]$.⁹⁷ In the IR spectra of these ILs in equilibrium with 68 bar CO_2 , a splitting of the bending mode peak around 655 cm^{-1} occurs. Kazarian et al. interprets this as two CO_2 bending modes present in the system, one of linear CO_2 and the other of a slightly bent

CO₂. The effect is more apparent with [emim][BF₄], indicating that the fluorinated anion enhances the interaction with the anion that leads to a bent CO₂ geometry. In the Raman spectroscopic study of CO₂+ [bmim][TFA] by Cabaço et al., the characteristic peak at 650 cm⁻¹, associated with interaction of CO₂ and the Lewis base site of [TFA]⁻, was not observed. However, they suggest the interaction was present, by evidence seen with DFT studies and decoupling of the Fermi diad peaks of CO₂, but the 650 cm⁻¹ peak obscured by the spectra of the solvent.¹¹⁴

The Raman spectra of the CO₂-[emim][Tf₂N] system at atmospheric conditions and in equilibrium with up to 40 bar are shown in Figure 6.11. As with the oligomer solvents, the Fermi diad peaks of the CO₂ symmetric stretch mode are present in the spectra and grow with CO₂ pressure. The literature evidence suggests that there are interactions between CO₂ and the anions of the IL system. However, in these spectra we do not observe any direct indication of interactions, specifically there is no peak formation at 650 cm⁻¹. Makino et al. reported similar results to ours in their study of [emim][Tf₂N] and [emim][BF₄].⁸⁶

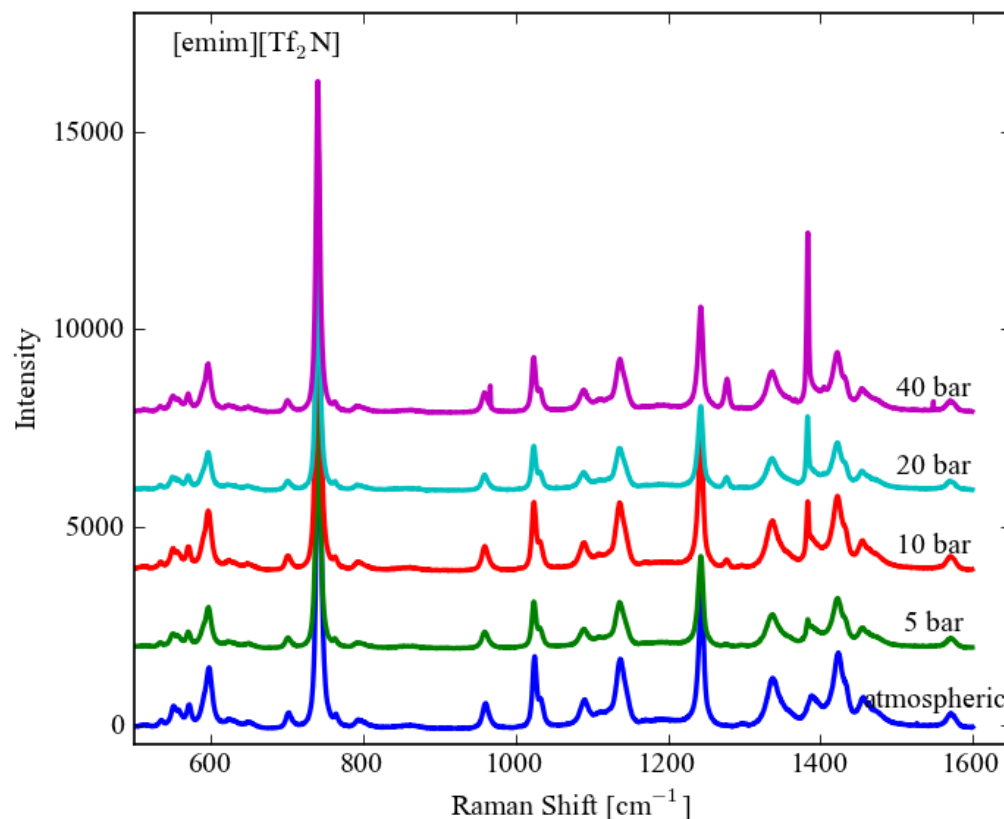


Figure 6.11: Raman spectra of [emim][Tf₂N] at atmospheric conditions and equilibrium with 5 to 40 bar CO₂ at 295 K.

The absence of a peak at 650 cm⁻¹ is not enough to conclude that there is no interaction between the CO₂ and anion. With [emim][Tf₂N], the likely interaction site for CO₂ is around the -CF₃ groups and any interaction should affect the vibrational modes associated with -CF₃. Both the -CF₃ stretch mode and the -SO₂ stretch modes, a neighboring group to CF₃, produce strong Raman peaks at 1244 cm⁻¹ and 1137 cm⁻¹ respectively.¹¹⁵ We examined the shape and positions of these peaks for the CO₂ pressures studied and saw no conclusive signs of perturbation of either peak, further suggesting that at up to 40 bar no interaction takes place or the interaction is too small to be

detected. This suggests that the observed enhanced solubility of CO₂ in ILs with fluorinated anions, even at low pressures, is not enhanced directly by CF₃ interactions but possibly by long range forces due to the presence of F atoms.

6.3.4 Analysis of Solvated CO₂ Spectra

Figure 6.12 shows the spectra of the CO₂-Selexol[®] system in the Raman shift region of the CO₂ Fermi diad. As previously discussed, the intensity of the Fermi diad peaks grows as the CO₂ pressure increases. Additionally, the Fermi diad peaks of solvated CO₂ are red shifted (lower in energy) relative to the position of the gas phase peaks. In the case of Selexol[®], the upper band of the 5 bar spectra appears at 1380 cm⁻¹ and the lower band appears at 1275 cm⁻¹.

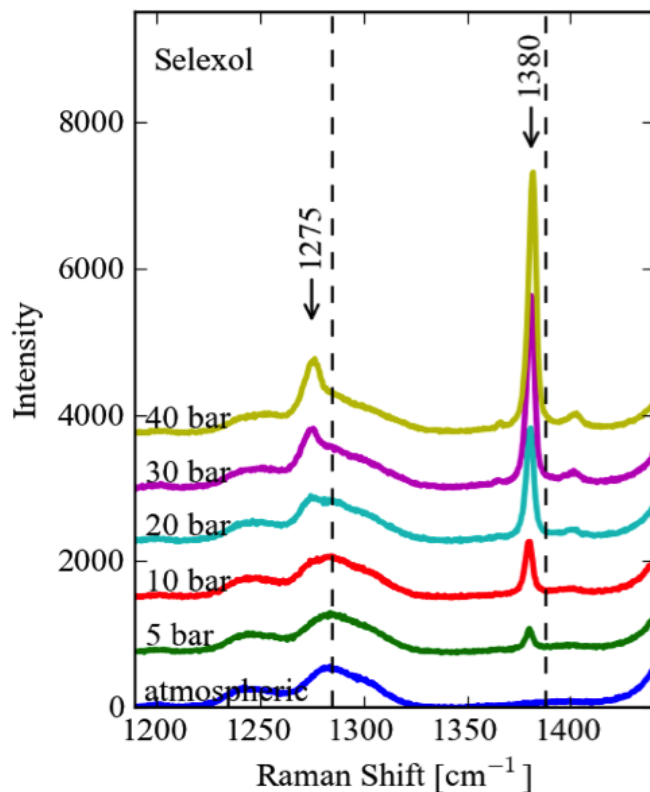


Figure 6.12: Raman spectra of Fermi diad peaks of solvated CO_2 in Selexol[®] in equilibrium with 5 to 40 bar CO_2 pressure. The arrow markers denote the position of the Fermi diad peaks in the 5 bar spectra. The position of the Fermi diad peaks of gas phase CO_2 are indicated by the dashed lines.

This phenomena was observed for all the solvents. The positions of the Fermi diad upper band of solvated CO_2 are shown in Figure 6.13 for the oligomer systems as a function of CO_2 pressure. The peak positions were calculated using baseline subtracted solvated CO_2 spectrum and calibrated using spectrum of external naphthalene standard taken at each pressure. The red shift of Fermi diad is solvent specific, indicating that it is an effect of the solvent, not just the condensed state of CO_2 . In the absence of interactions between CO_2 and the solvent, the red shift in the CO_2 symmetric stretch mode could be caused by the solvent environment softening the interatomic bonds of

CO₂.¹⁰¹ Some have attributed this shift, also observed in other solute solvent systems to the interaction between the solute dipole and the dielectric constant of the solvent.^{116–118}

Comparing the oligomer systems, the molecular structure of the solvent has a larger impact on the red shift, with linear structures (PEGDME, MW 250, and Selexol) inducing a larger shift compared to branched structures, PPGDME and PDMS. The molecular weight, or chain length, of the oligomer does not appear to effect the red shift. Additionally, Figure 6.13 shows that as the equilibrium CO₂ pressure increases, the red shift of the dissolved CO₂ spectra reduces, with the peak position tending toward the Raman shift position of gas phase CO₂.

Swelling has been reported with PDMS and PEG systems upon dissolving CO₂ into the solvents.^{109,119} This was observed qualitatively during the course of our experiments. Swelling corresponds directly to an increase in the molar volume of the solvent and could explain the shift in the CO₂ Raman bands. As the molar volume increases, the effect of the solvent on the solute is diluted and the local environment that CO₂ experiences becomes more like a pure CO₂ environment.

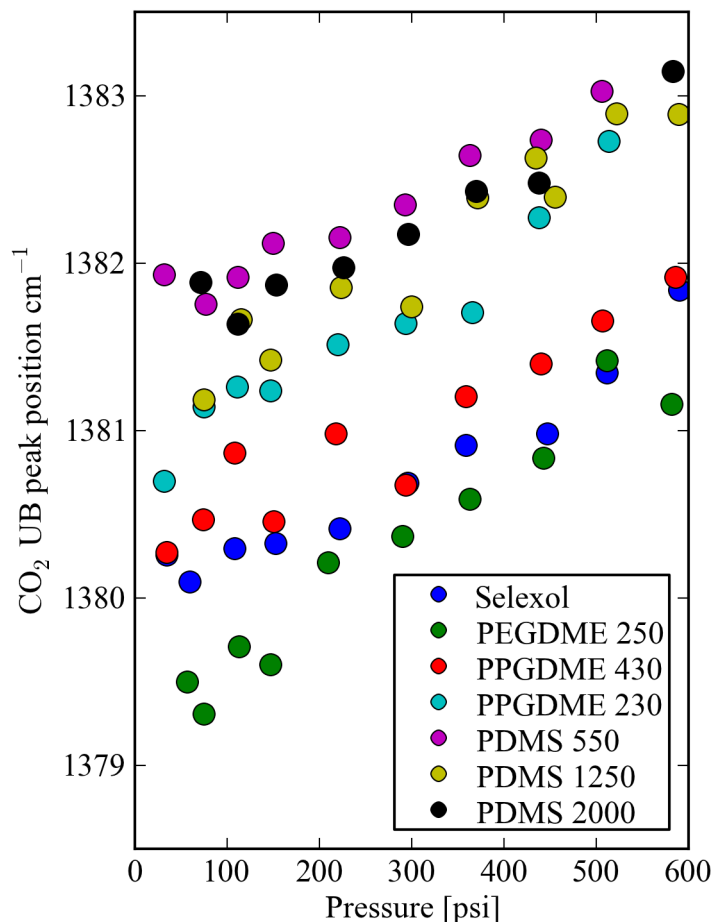


Figure 6.13: Upper Fermi diad Raman peak position of symmetric stretch vibrational mode of solvated CO_2 in oligomer solvents.

Figure 6.14 presents the peak position analysis for the ionic liquid systems as a function of CO_2 pressure. The y-axis of Figure 6.14 is shifted from Figure 6.13, but the scale is preserved to facilitate comparisons. In general the $[\text{C}_n\text{mim}][\text{Tf}_2\text{N}]$ solvent induces a smaller red shift in the symmetric stretch peak compared to the oligomers (Figure 6.14-A). The effect appears to be independent of alkyl chain length. Since the resolution of the spectrometer is 0.5 cm^{-1} , it is hard to conclude if the peak position of CO_2 in $[\text{hmim}][\text{Tf}_2\text{N}]$ and $[\text{emim}][\text{Tf}_2\text{N}]$ are truly different. Figure 6.14-B shows that anion selection impacts the red shift in the symmetric stretch peak of solvated CO_2 , with $[\text{TCB}]^-$ having the largest effect. Comparing the

structure of $[\text{TCB}]^-$ with $[\text{BF}_4]^-$ and $[\text{Tf}_2\text{N}]^-$, the molecular structure, or bulkiness, of the anion is not related to this effect since $[\text{TCB}]^-$ have $[\text{BF}_4]^-$ similar structures, but produce large differences in the red shift of the CO_2 peak. $[\text{emim}][\text{Tf}_2\text{N}]$ and $[\text{emim}][\text{BF}_4]$ have similar dielectric constants, which could explain the closely clustered CO_2 peak positions for these solvents.¹²⁰ However, not enough information is known about $[\text{emim}][\text{TCB}]$ and $[\text{emim}][\text{FAP}]$ to confirm this.

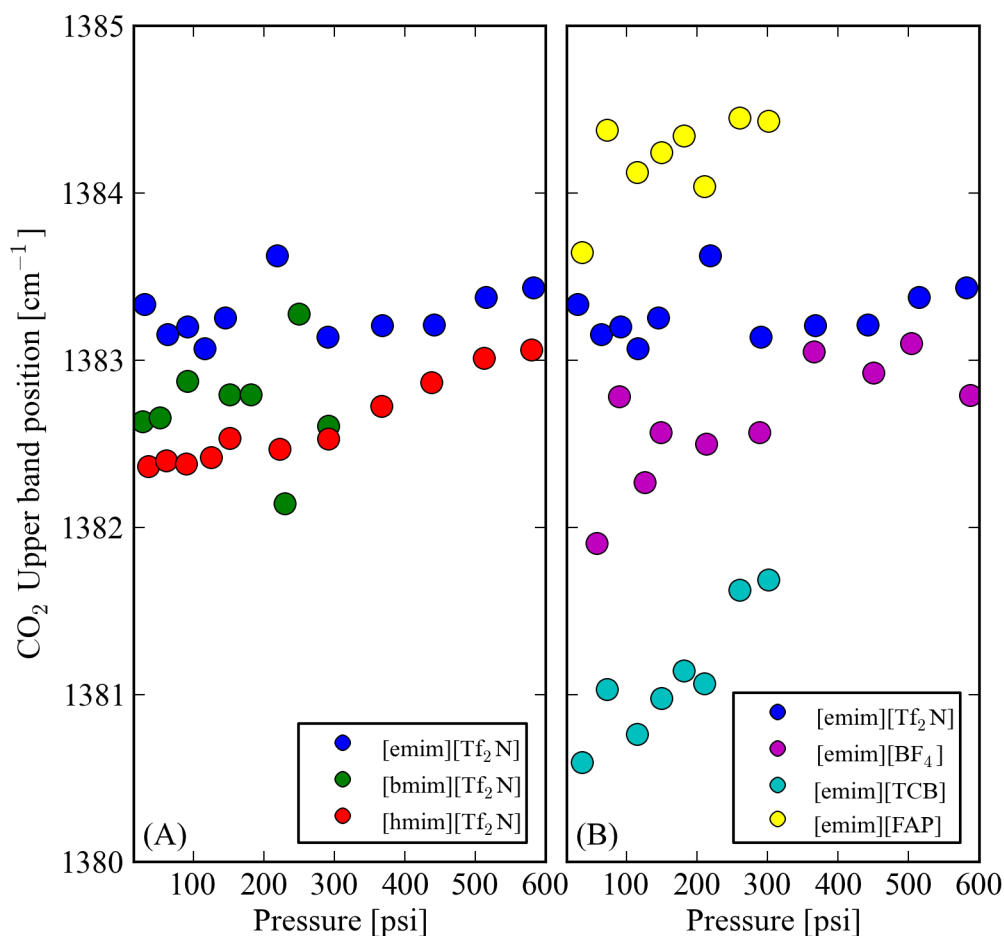


Figure 6.14: Upper Fermi diad Raman peak position of symmetric stretch vibrational mode of solvated CO_2 in ILs.

The reduction in the red shift of the CO₂ peak due to an increase in CO₂ pressure is minor compared to the oligomer solvents, with the exception being [emim][TCB]. This could be explained by the nature of ionic liquids. Given that the structure of ILs is defined by charge interaction between the anion and cation, swelling of the liquid involves charge separation, which should be more difficult than separating neutral molecules. The limited swelling of the solvent maintains the solvent effect on the solute, even at high CO₂ pressures. In the case of [emim][TCB], the anion-cation interaction in [emim][TCB] is weaker than with [emim][BF₄], thus reducing its resistance to swell.¹²¹

6.3.5 Measuring Solubility of CO₂ in Physical Solvents Using Raman Spectra

Henry's law is a simple means to quantify gas solubility in a solvent through a proportionality relationship between the equilibrium amount of solute dissolved in a solvent and the amount of that species in the gas phase. Equation 6.3 represents Henry's law through a concentration relationship, relating the CO₂ concentration in the solvent phase, CO_{2,solv}, and the concentration of CO₂ in the gas phase, CO_{2,gas}, with a dimensionless Henry's law constant, k_H^{cc} . The Henry's law constant, in one quantity, measures the performance of the solvent and can be utilized to make comparisons of performance between solvents, which is an integral piece of information in developing and ranking CO₂ capture solvents.

$$c_{CO_2,gas} = k_H^{cc} c_{CO_2,solv} \quad (6.3)$$

Recall Equation 6.1, the Raman intensity of an analyte holds quantitative information about the system, specifically the concentration of analyte in the

system. However, the Raman intensity also depends on system parameters that can also be variable and the Raman cross-section of the analyte which can be difficult to measure. Examples in literature have utilized the relationship in Equation 6.1 to quantify the analyte concentration in a sample from Raman spectra by using a calibration model for their system to relate measured intensity to known concentration.¹²² These analytical models capture the effects of system variables and the Raman cross-section on the measured intensity.

A conventional calibration model cannot be obtained with our experimental setup because we cannot prepare samples of known CO₂ concentration. However, k_H^{cc} of the solvent can still be determined from the Raman spectra by leveraging our experimental system set-up to eliminate variation in system variables and utilizing the spectra to determine the equilibrium concentration ratio of CO₂ in the gas and solvent phase.

The measured intensity of the CO₂ peaks in solvent and gas phase spectra can be expressed as Equation 6.4 and Equation 6.5, respectively, and are a function of the system variables: the incident laser intensity (I_0) and the focal length (dz); and phase dependent variables: Raman cross-section of CO₂ in that phase (σ_{CO_2}), and the concentration of CO₂ in the phase ($c_{CO_2, gas}$).

$$I_{CO_2, gas} = I_0 dz \sigma_{CO_2, gas} c_{CO_2, gas} \quad (6.4)$$

$$I_{CO_2, solv} = I_0 dz \sigma_{CO_2, solv} c_{CO_2, solv} \quad (6.5)$$

Using the 1380 cm^{-1} peak for analysis, the integrated intensity of the Raman peak for CO_2 in the gas and solvent phase are plotted against each other in Figure 6.15. Throughout a gas-solvent experiment, the incident laser intensity was constant and focal length was determined for each measurement using a consistent approach. Thus, the system variables were constant and expected to be the same for the gas and solvent phase spectra. Therefore, the slope of the trend in Figure 6.15 can be expressed as Equation 6.6, with the system dependent variables canceling out. Rearranging Equation 6.6, gives a relationship for k_H^{cc} from the analysis of the gas and solvent phase Raman spectra.

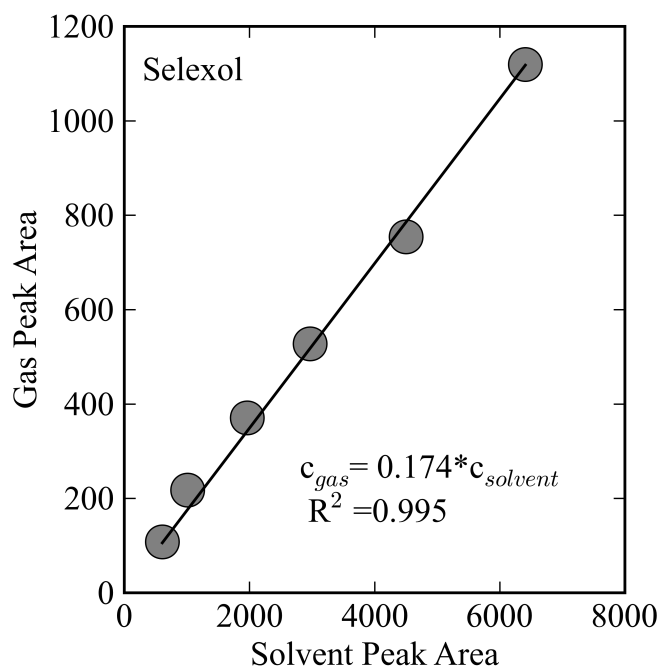


Figure 6.15: Example of peak analysis to determine k_H^{cc} from Raman spectra using Selexol[®]. Each point plots the integrated area of the CO_2 upper band in the solvent spectra vs. the CO_2 upper band area in the gas spectra for an equilibrium CO_2 pressure. The slope of this dataset is related to k_H^{cc} through Equation 6.7.

$$m = \frac{\sigma_{CO_2,gas} c_{CO_2,gas}}{\sigma_{CO_2,solv} c_{CO_2,solv}} \quad (6.6)$$

$$m \frac{\sigma_{CO_2,solv}}{\sigma_{CO_2,gas}} = \frac{c_{CO_2,gas}}{c_{CO_2,solv}} = k_H^{cc} \quad (6.7)$$

The Raman cross-section ratio in Equation 6.7, describes a well-observed solvent enhancement on Raman intensity.¹²³ The Raman signal of a molecule in the condensed phase is stronger than that of the molecule in the gas phase due to local dielectric enhancement. The enhancement factor can be estimated using the local-field correction derived by Mirone et al. and Eckhart and Wagner (Equation 8), where n_{CO_2} is the refractive index of CO₂ and n_{solv} is the refractive index of the solvent.^{124, 125}

$$\frac{\sigma_{CO_2,gas}}{\sigma_{CO_2,solv}} = \left[\frac{n_{CO_2}^2 + 2}{\frac{n_{CO_2}}{n_{solv}} + 2} \right]^4 \quad (6.8)$$

Fini et al. demonstrated this relationship worked well for binary liquid systems and Berger et al. showed it was applicable to dissolved gases in water.^{122, 126} Using the cross-section ratio (Equation 8), the slope from the relationship in Figure 6 can be corrected to determine the equilibrium CO₂ concentration ratio and k_H^{cc} (Equation 7). Following Berger's computation of refractive index of gases, n_{CO_2} was determined to be 1.18. The refractive indexes of the solvents in this work were provided by Sigma Aldrich and if unavailable measured using a Reichert Analytical Instruments AR7 refractometer.

To demonstrate the validity of this approach, the analysis was first performed on CO₂-octane and CO₂-decane systems. Raman studies of CO₂-alkanes studies were carried out three times each for decane and octane. The Henrys law constant of CO₂-octane and CO₂-decane from the analysis of the Raman spectra was found to be 1269±25 psi and 1288±48 psi respectively. Figure 6.16 shows these results alongside k_H values computed from multiple vapor-liquid equilibrium data sets presented in literature using traditional experimental techniques to measure solubility. The solubility of CO₂ in alkanes determined from the analysis of Raman spectra is consistent with the trend seen by compiling literature values. Also, the experimental variation observed is within the range of variation of the literature data sets, specifically referring to k_H for decane at 344 K. This shows that our technique is comparable to more standard techniques to measuring solubility.

Table 6.1 shows the k_H^{cc} values obtained from the Raman spectra analysis of the CO₂-solvent systems. There is a range of CO₂ solubility observed with each solvent class, indicating that there is the potential to tune the CO₂ solubility with slight modifications to the chemical structure of the solvent. Of the CO₂-philic oligomers, PEGDME-250 shows the highest CO₂ solubility. However, as previously discussed it is completely miscible with water and not ideal for pre-combustion CO₂ capture. Comparing the results of the more hydrophobic oligomers, as the oligomer becomes less water miscible (PEGDME >> PPGDME > PDMS) the solubility of CO₂ decreases. This is a potential trade-off associated with these systems. The [C_nmim][Tf₂N] ionic liquids show comparable solubility to the CO₂-philic oligomers.

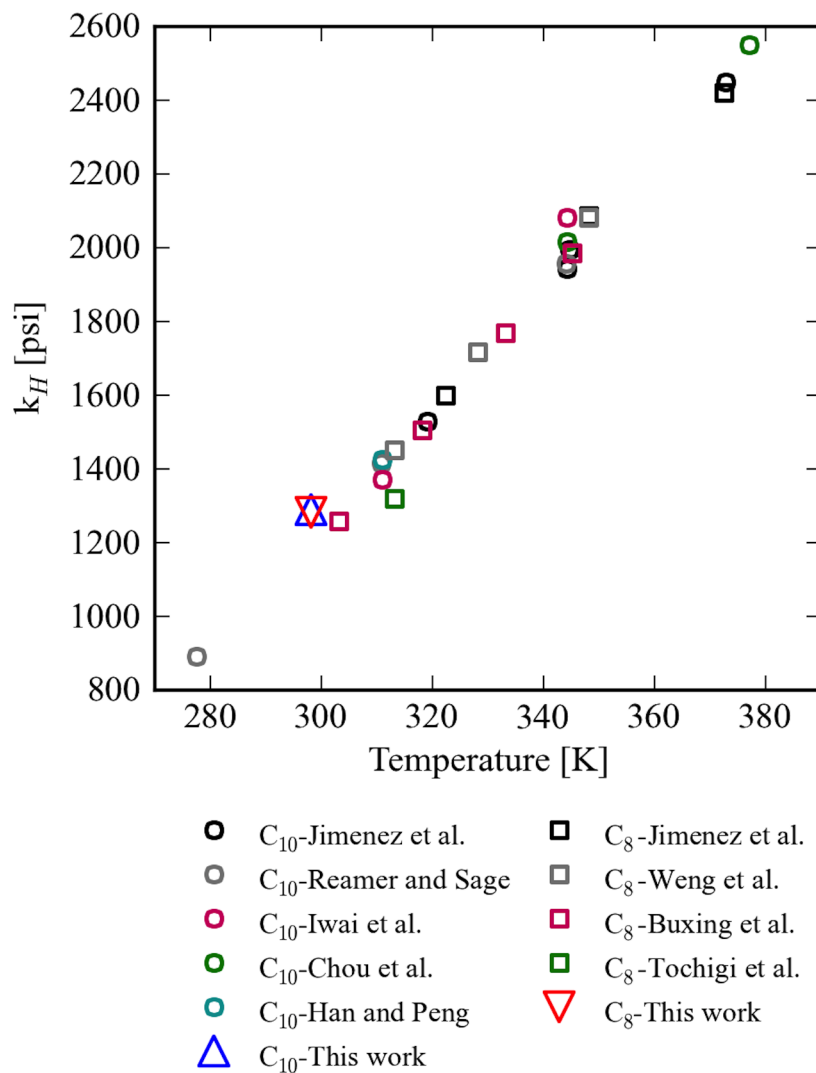


Figure 6.16: A comparison of Henrys law constants for octane^{98,127–129} and decane^{98,130–133} computed using vapor-liquid equilibrium data reported in literature over a range of temperatures and the Raman spectroscopy technique presented in this work. Octane: k_H from literature (\square), this work (∇), Decane: k_H from literature(\circ), this work(\triangle).

Solvent	MW	k_H^{cc}
CO ₂ -philic Oligomers		
Selexol	–	0.562 ± 0.025
PEGDME	250	0.386 ± 0.032
PPGDME	230	0.409
PPGDME	430	0.422
PDMS	550	0.656 ± 0.032
PDMS	1250	0.716 ± 0.042
PDMS	2000	0.793 ± 0.030
[C _n mim][Tf ₂ N] Ionic Liquids		
[emim][Tf ₂ N]	391.3	0.455 ± 0.121
[bmim][Tf ₂ N]	419.3	0.487 ± 0.020
[hmim][Tf ₂ N]	447.4	0.536 ± 0.024

Table 6.1: k_H^{cc} values for CO₂-philic oligomers and [C_nmim][Tf₂N] Ionic Liquids determined from analysis of Raman spectra of CO₂-solvent system. Error reported for 95% confidence intervals.

Connecting molecular property to performance, Figure 6.17 shows the relationship between molecular weight and CO₂ solubility for PDMS and [C_nmim][Tf₂N] ionic liquids. The quantitative relationship is solvent type specific, but qualitatively with both classes of solvents, the CO₂ solubility increases with decreasing molecular weight. The molecular weight is an easy property to tune for PDMS, or any other oligomer solvent, by adjusting the average number of monomer units/molecule in the system. However, other chemical properties, like volatility, are also affected by molecular weight and other performance metrics like solvent loss may come at an expense to increased CO₂ capacity. The correlation between molecular weight and CO₂ solubility with [C_nmim][Tf₂N] ionic liquids is much steeper, indicating that

small adjustments to the MW of the IL have large effects on the CO₂ solubility. However, the solvents in this study are already close to the lower molecular weight limit of [C_nmim][Tf₂N] type ionic liquids, leaving only 1-methyl-2-methylimidazolium bis(trifluoromethylsulfonyl)imide and possibly 1-methylimidazolium bis(trifluoromethylsulfonyl)imide as lower molecular weight alternatives. Additional relationships likely exist for other types of ionic liquids that could access lower k_H^{cc} values.

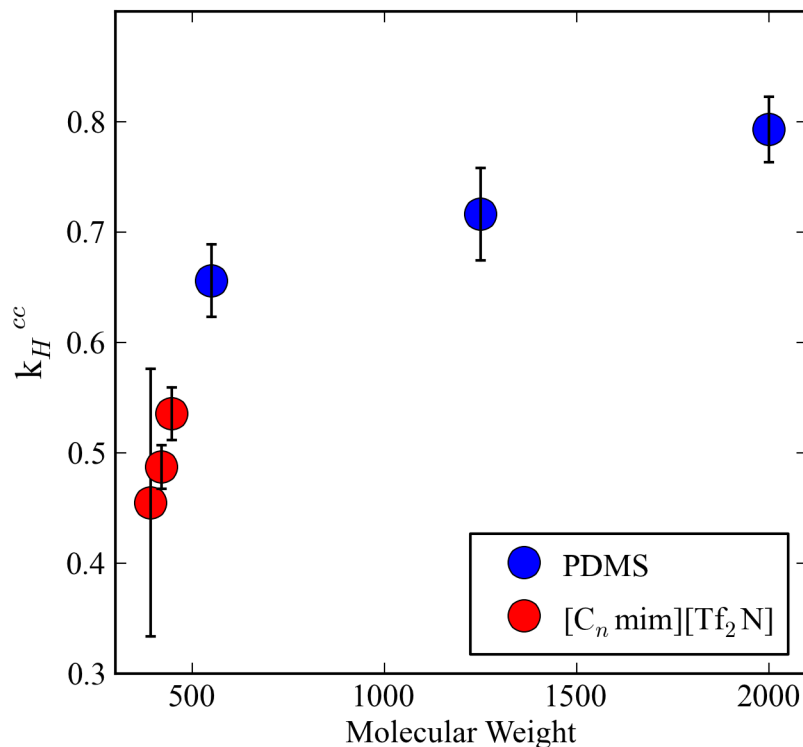


Figure 6.17: k_H^{cc} for CO₂ in different molecular weight PDMS and [C_nmim][Tf₂N] solvents.

6.4 Conclusions

This chapter presented a study of two classes of physical solvents, hydrophobic CO₂-philic oligomers and 1-alkyl-3-methylimidazolium based

ionic liquids, using Raman spectroscopy at pre-combustion CO₂ capture relevant pressure conditions. Using Raman spectroscopy we characterized CO₂-solvent interactions and presented an approach to obtain quantitative solubility measurements from the Raman spectra of these systems. The Raman spectra of the CO₂-solvent system showed the presence of solvated CO₂ with the appearance of the Fermi diad peaks of the CO₂ symmetric stretch mode. At pressures up to 40 bar CO₂, there were no additional peak formations or deformation of the solvent spectra that would indicate CO₂-solvent interactions. Analysis of the Fermi diad peaks of solvated CO₂ showed that the peaks were red shifted (at lower frequencies) compared to the gas phase. The magnitude of this effect was solvent specific, suggesting that this observation is a marker of the role of the solvent in the system. The quantitative measure of CO₂ solubility obtained from the Raman spectra showed a strong relationship between solvent molecular weight and CO₂ solubility. The CO₂ solubility increased with decreasing molecular weight. Although the relationship was specific to the class of solvent, it does show the ability to tune solvents for desired CO₂ solubility through the solvent molecular weight.

7 Conclusions

Developing an effective CO₂ capture process to address emissions from coal-fired power plants is a large problem, both in scale and economic impact. However, there is room to improve the economics and overall efficiency of CO₂ capture, while leveraging the commercial processes that exist for both post-combustion and pre-combustion capture, with the development of new solvents. The work presented in this thesis employed multi-scale techniques to develop the necessary understanding to approach the intelligent design of advanced carbon capture solvents. Density Functional Theory and Raman spectroscopy were used to study CO₂-solvent interactions at the molecular level, with the objective of understanding the role of the solvent in these interactions and to identify what solvent properties impact these interactions and how to control them. This level of knowledge enables researchers to tailor solvents to desired performance for CO₂ capture.

In addition to understanding the CO₂-solvent system at the molecular level, a process level understanding of the impact of solvent selection is necessary to define the direction of solvent design. As highlighted by Oexmann and Kather, stronger interactions do not equate to better performance of the process.¹⁰ This is particularly true for the post-combustion capture process. Solvent-CO₂ interactions impact many process variables and in turn have a complex relationship to energy demands and cost of the process. We utilized Aspen models coupled with derivative-free optimization to quantify and equitably compare the energy and capital cost demands of post-combustion CO₂ capture using different solvents to understand the relationship between solvent selection and process performance.

7.1 A Molecular Understanding of CO₂-Amine Interactions for Post-Combustion Capture From Density Functional Theory

In this work we utilized density functional theory to study amine-CO₂ interactions and focused specifically on three classes of structurally similar amines: alkylamines, alkanolamines, and fluorinated alkylamines including primary, secondary and tertiary amines. These classes spanned electron-withdrawing to donating behavior in the functional group and accounted for the effects of hydrogen-bonding, extent of functionalization, and functional group proximity to the reacting site on amine-CO₂ interactions. We presented trends in the reaction energies to form amine-bicarbonate and amine-carbonate products. Generally, amines with electron withdrawing groups destabilized CO₂ reaction products, whereas electron-donating groups stabilized CO₂ reaction products. Hydrogen bonding also stabilized CO₂ reaction products.

A conceptual view of molecular interactions was used to build and understanding of the relationship between electronic structure and reaction energy along each pathway. We concluded the amine electronegativity was a descriptor for the bicarbonate pathway. We attempted to describe the carbamate pathway reaction energy using the local softness of the reacting nitrogen site, following Sandersons Hard Soft Acid Base principal, but were not able to observe a conclusive trend. This indicates that a single descriptor may not be adequate in describing the reaction energy along the carbamate pathway.

Additionally, we showed that the amine electronegativity could be tuned in an intuitive manner by functionalizing the amine with electron donating or

electron withdrawing groups. This shows promise for tuning the bicarbonate reaction energy with different functional groups. Also, this work suggests that there may be practical bounds to the range in bicarbonate reaction energy, most of which is spanned by this work, since we considered strong electron withdrawing and electron donating groups.

7.2 Understanding the Impact of Solvent Selection on the Post-Combustion CO₂ Capture Process

In this work we presented a methodology to evaluate and compare the performance of different amines as CO₂ capture solvents for a 550 MW power plant using net power output and capital cost of the CO₂ capture process as performance metrics. We used Aspen Plus coupled with a multi-objective genetic algorithm optimization to determine the best process design and operating conditions for each solvent. This ensured that the processes utilized for the comparison are those which are best suited for the specific solvent. We evaluated and compared the process energy demands and capital cost of a 90% CO₂ capture process from a 550 MW coal fired power plant using three different amines: monoethanolamine (MEA), diethanolamine (DEA), and 2-amino-2-methyl-1-propanol (AMP). Our analysis, as expected, showed that the optimal process and operating specifications are amine specific. Additionally, there are trade-offs between the net power output of the coal plant and capital cost and a single solution optimized both design objectives. Comparing the results of each solvent, we showed that DEA has the potential to be a better performing solvent than MEA, with a lower energy penalty and lower capital cost investment.

This approach and subsequent results can be utilized to focus the direction of solvent design by enabling the evaluation and comparison of contextually

relevant performance metrics, instead of relying on only values measured at the laboratory level. However, the quantitative results from this work are highly dependent on the robustness of the thermodynamic models for the amine-CO₂ systems available in Aspen. Therefore, as the development of new solvents progresses, it will become increasingly important for research to include refining thermodynamic models for the solvents.

7.3 A Molecular Understanding of CO₂-Physical Solvent Interactions From Raman Spectroscopy

In this work we presented a Raman spectroscopic study of CO₂-philic oligomer solvents and 1-alkyl-3-methylimidazolium based ionic liquids to understand the role of the solvent in CO₂-solvent interactions at pre-combustion capture pressure conditions. From the spectra of the CO₂-solvent systems for all the solvents studied, we concluded that at the pressures up to 40 bar most, if not all, of the solvated CO₂ existed in a linear geometry with no interaction with the solvent that led to deformation of the CO₂ structure. However, the observed red shift of the symmetric stretch mode suggests a long range interaction of CO₂ with the solvent that softens this vibrational mode. The magnitude of the red shift is solvent dependent, but it remains unclear as to what attribute of the solvent dictates this shift.

Additionally, we developed a method to measure the solubility of CO₂ from the Raman spectra. We demonstrated the validity of this method on octane and decane to determine k_H^{cc} , the Henry’s law constant computed on a concentration basis, for the CO₂-philic oligomers and ionic liquids. Of the solvents studied, there was a range in observed CO₂ solubility. For PDMS and [C_{*n*}mim][Tf₂N] solvents, we showed that the CO₂ solubility increased with decreasing molecular weight, suggesting that solubility could be tuned

by modifying the molecular weight of the solvent. The relationship was stronger for the $[C_n\text{mim}][\text{Tf}_2\text{N}]$ solvents compared to PDMS, however there are only two $[C_n\text{mim}][\text{Tf}_2\text{N}]$ type ILs lower in molecular weight than the ones we studied, indicating that there is a limit to the solubility of CO_2 in $[C_n\text{mim}][\text{Tf}_2\text{N}]$ type ILs. We hypothesize that a corresponding linear trend exists for other structurally similar groups of solvents, but more experiments need to be performed to confirm this.

Although from this work we can conclude that CO_2 solubility is enhanced in lower molecular weight solvents, it is unclear that the lowest molecular weight solvent is the most desirable. There are many other solvent properties that correlate with molecule weight. For example, with PDMS, solvent volatility increases with decreasing molecular weight while viscosity decreases. Both volatility and viscosity of the solvent are important properties for performance of a pre-combustion capture process. Solvent volatility will factor into the flash pressures used for solvent regeneration and therefore impact the solvent circulation rate. The viscosity will impact the parasitic energy demand of the capture process through its effect on the pumping energy necessary to circulate the solvent. Even though no reaction takes place in the pre-combustion capture process, the trade-offs between the solvent properties that are desirable and what are physically accessible make the system just as complicated. Therefore a similar approach like the one presented in this thesis for post-combustion capture is necessary to understand the impact of solvent selection on the pre-combustion capture process and identify the direction to tune the CO_2 solubility of physical solvents.

References

- [1] W. Bank, *World Development Indicators 2012*. World Bank Publications, Apr. 2012.
- [2] E. Rubin, H. Mantripragada, A. Marks, P. Versteeg, and J. Kitchin, “The Outlook for Improved Carbon Capture Technology,” *Progress in Energy and Combustion Science*, pp. 1–42, 2012.
- [3] International Energy Agency, *CO₂ Emissions from Fuel Combustion: Highlights*. 2012 Edition, OECD, 2012.
- [4] U.S. Environmental Protection Agency, “Inventory of U.S. Greenhouse Gas Emissions and Sinks: 1990-2010,” Tech. Rep. EPA 430-R-12-001, U.S. Environmental Protection Agency, Washington D.C., Apr. 2012.
- [5] U.S. Energy Information Agency, “EIA Electricity Data.” <http://www.eia.gov/electricity/data>.
- [6] G. T. Rochelle, “Amine Scrubbing for CO₂ Capture,” *Science*, vol. 325, pp. 1652–1654, Sept. 2009.
- [7] J. Ciferno, J. Litynski, S. Plasynski, J. Murphy, G. Vaux, R. Munson, and J. Marano, “DOE/NETL Carbon Dioxide Capture and Storage RD&D Roadmap,” *US DOE National Energy Technology Laboratory, Pittsburgh*, 2010.
- [8] NETL, “Cost and Performance Comparison Baseline for Fossil Energy Power Plants,” Tech. Rep. DOE/2010/1397, Nov. 2010.
- [9] H. Herzog, J. Meldon, and A. Hatton, “Advanced Post-Combustion CO₂ Capture,” *Clean Air Task Force*, pp. 1–39, 2009.
- [10] J. Oexmann and A. Kather, “Minimising the Regeneration Heat Duty of Post-Combustion CO₂ Capture by Wet Chemical Absorption: the Misguided Focus on Low Heat of Absorption Solvents,” *International Journal of Greenhouse Gas Control*, vol. 4, pp. 36–43, Jan. 2010.
- [11] G. Versteeg, L. Van Dijck, and W. Van Swaaij, “On the Kinetics Between CO₂ And Alkanolamines Both in Aqueous and Non-Aqueous Solutions. An Overview,” *Chemical Engineering Communications*, vol. 144, no. 1, pp. 113–158, 1996.
- [12] G. Sartori and D. Savage, “Sterically Hindered Amines for Carbon Dioxide Removal From Gases,” *Industrial & Engineering Chemistry Fundamentals*, vol. 22, no. 2, pp. 239–249, 1983.

- [13] J.-G. Shim, J.-H. Kim, Y. H. Jhon, J. Kim, and K.-H. Cho, "DFT Calculations on the Role of Base in the Reaction Between CO₂ And Monoethanolamine," *Industrial & Engineering Chemistry Research*, vol. 48, pp. 2172–2178, Feb. 2009.
- [14] E. F. da Silva and H. F. Svendsen, "Computational Chemistry Study of Reactions, Equilibrium and Kinetics of Chemical CO₂ Absorption," *International Journal of Greenhouse Gas Control*, vol. 1, pp. 151–157, Apr. 2007.
- [15] E. F. da Silva and H. F. Svendsen, "Ab Initio Study of the Reaction of Carbamate Formation From CO₂ and Alkanolamines," *Industrial & Engineering Chemistry Research*, vol. 43, pp. 3413–3418, June 2004.
- [16] B. Arstad, R. Blom, and O. Swang, "CO₂ Absorption in Aqueous Solutions of Alkanolamines: Mechanistic Insight from Quantum Chemical Calculations," *The Journal of Physical Chemistry A*, vol. 111, pp. 1222–1228, Feb. 2007.
- [17] P. V. Danckwerts, "The Reaction of CO₂ With Ethanolamines," *Chemical Engineering Science*, vol. 34, pp. 443–446, Jan. 1979.
- [18] T. Donaldson and Y. Nguyen, "Carbon Dioxide Reaction Kinetics and Transport in Aqueous Amine Membranes," *Industrial & Engineering Chemistry Fundamentals*, vol. 19, no. 3, pp. 260–266, 1980.
- [19] R. J. Hook, "An Investigation of Some Sterically Hindered Amines as Potential Carbon Dioxide Scrubbing Compounds," *Industrial & Engineering Chemistry Research*, vol. 36, pp. 1779–1790, May 1997.
- [20] A. S. Lee and J. R. Kitchin, "Chemical and Molecular Descriptors for the Reactivity of Amines with CO₂," *Industrial & Engineering Chemistry Research*, pp. 13609–13618, 2012.
- [21] G. Puxty, R. Rowland, A. Allport, Q. Yang, M. Bown, R. Burns, M. Maeder, and M. Attalla, "Carbon Dioxide Postcombustion Capture: A Novel Screening Study of the Carbon Dioxide Absorption Performance of 76 Amines," *Environmental Science & Technology*, vol. 43, pp. 6427–6433, Aug. 2009.
- [22] P. Singh, J. P. M. Niederer, and G. F. Versteeg, "Structure and Activity Relationships for Amine Based CO₂ Absorbents—I," *International Journal of Greenhouse Gas Control*, vol. 1, pp. 5–10, Apr. 2007.
- [23] E. M. Mindrup and W. F. Schneider, "Computational Comparison of the Reactions of Substituted Amines with CO₂," *ChemSusChem*, vol. 3, pp. 931–938, July 2010.

- [24] A. Chakraborty, G. Astarita, and K. Bischoff, "CO₂ Absorption in Aqueous Solutions of Hindered Amines," *Chemical Engineering Science*, vol. 41, no. 4, pp. 997–1003, 1986.
- [25] A. Chakraborty, K. Bischoff, G. Astarita, and J. Damewood, "Molecular Orbital Approach to Substituent Effects in Amine-CO₂ Interactions," *Journal of the American Chemical Society*, vol. 110, no. 21, pp. 6947–6954, 1988.
- [26] H.-B. Xie, J. K. Johnson, R. J. Perry, S. Genovese, and B. R. Wood, "A Computational Study of the Heats of Reaction of Substituted Monoethanolamine with CO₂," *The Journal of Physical Chemistry A*, vol. 115, pp. 342–350, Jan. 2011.
- [27] R. G. Parr and Y. Weitao, *Density-Functional Theory of Atoms and Molecules (International Series of Monographs on Chemistry)*. Oxford University Press, USA, May 1994.
- [28] J. Gázquez, "Perspectives on the Density Functional Theory of Chemical Reactivity," *Journal of the Mexican Chemical Society*, vol. 52, no. 1, pp. 3–10, 2008.
- [29] P. Geerlings, F. De Proft, and W. Langenaeker, "Conceptual Density Functional Theory," *Chemical Reviews*, vol. 103, pp. 1793–1874, May 2003.
- [30] M. J. Frisch, G. W. Trucks, H. B. Schlegel, G. E. Scuseria, M. A. Robb, J. R. Cheeseman, G. Scalmani, V. Barone, B. Mennucci, G. A. Petersson, H. Nakatsuji, M. Caricato, X. Li, H. P. Hratchian, A. F. Izmaylov, J. Bloino, G. Zheng, J. L. Sonnenberg, M. Hada, M. Ehara, K. Toyota, R. Fukuda, J. Hasegawa, M. Ishida, T. Nakajima, Y. Honda, O. Kitao, H. Nakai, T. Vreven, J. A. Montgomery, Jr., J. E. Peralta, F. Ogliaro, M. Bearpark, J. J. Heyd, E. Brothers, K. N. Kudin, V. N. Staroverov, R. Kobayashi, J. Normand, K. Raghavachari, A. Rendell, J. C. Burant, S. S. Iyengar, J. Tomasi, M. Cossi, N. Rega, J. M. Millam, M. Klene, J. E. Knox, J. B. Cross, V. Bakken, C. Adamo, J. Jaramillo, R. Gomperts, R. E. Stratmann, O. Yazyev, A. J. Austin, R. Cammi, C. Pomelli, J. W. Ochterski, R. L. Martin, K. Morokuma, V. G. Zakrzewski, G. A. Voth, P. Salvador, J. J. Dannenberg, S. Dapprich, A. D. Daniels, . Farkas, J. B. Foresman, J. V. Ortiz, J. Cioslowski, and D. J. Fox, "Gaussian 09 Revision A.1." Gaussian Inc. Wallingford CT 2009.
- [31] G. Yu, S. Zhang, X. Yao, J. Zhang, K. Dong, W. Dai, and R. Mori, "Design of Task-Specific Ionic Liquids for Capturing CO₂: A Molecular Orbital Study," *Industrial & Engineering Chemistry Research*, vol. 45, pp. 2875–2880, Apr. 2006.

- [32] F. De Proft and P. Geerlings, "Calculation of Ionization Energies, Electron Affinities, Electronegativities, and Hardnesses Using Density Functional Methods," *Journal of Chemical Physics*, vol. 106, p. 3270, 1997.
- [33] G. Scalmani and M. J. Frisch, "Continuous Surface Charge Polarizable Continuum Models of Solvation. I. General Formalism," *Journal of Chemical Physics*, vol. 132, no. 11, pp. 114110–114125, 2010.
- [34] M. Cossi, G. Scalmani, N. Rega, and V. Barone, "New Developments in the Polarizable Continuum Model for Quantum Mechanical and Classical Calculations on Molecules in Solution," *Journal of Chemical Physics*, vol. 117, p. 43, 2002.
- [35] K. Iida, D. Yokogawa, A. Ikeda, H. Sato, and S. Sakaki, "Carbon Dioxide Capture at the Molecular Level," *Physical Chemistry Chemical Physics*, vol. 11, no. 38, p. 8556, 2009.
- [36] H. Sato and S. Sakaki, "Comparison of Electronic Structure Theories for Solvated Molecules: RISM-SCF versus PCM," *The Journal of Physical Chemistry A*, vol. 108, pp. 1629–1634, Mar. 2004.
- [37] J. Ochterski, "Thermochemistry in Gaussian," *Gaussian Inc, Pittsburgh, PA*, 2000.
- [38] R. Parr, R. Donnelly, M. Levy, and W. Palke, "Electronegativity: The Density Functional Viewpoint," *Journal of Chemical Physics*, vol. 68, p. 3801, 1978.
- [39] R. Iczkowski and J. Margrave, "Electronegativity," *Journal of the American Chemical Society*, vol. 83, no. 17, pp. 3547–3551, 1961.
- [40] R. T. Sanderson, "Electronegativity and Bond Energy," *Journal of the American Chemical Society*, vol. 105, pp. 2259–2261, Apr. 1983.
- [41] Y. Li and J. Evans, "The Fukui Function: a Key Concept Linking Frontier Molecular Orbital Theory and the Hard-Soft-Acid-Base Principle," *Journal of the American Chemical Society*, vol. 117, no. 29, pp. 7756–7759, 1995.
- [42] R. Parr and R. Pearson, "Absolute Hardness: Companion Parameter to Absolute Electronegativity," *Journal of the American Chemical Society*, vol. 105, no. 26, pp. 7512–7516, 1983.
- [43] R. Pearson, "Hard and Soft Acids and Bases, HSAB, Part 1: Fundamental Principles," *Journal of Chemical Education*, vol. 45, no. 9, p. 581, 1968.

- [44] P. W. Ayers, "The Physical Basis of the Hard/Soft Acid/Base Principle," *Faraday Discussions*, vol. 135, p. 161, 2006.
- [45] R. Pearson, "Hard and Soft Acids and Bases, HSAB, Part II: Underlying Theories," *Journal of Chemical Education*, vol. 45, no. 10, p. 643, 1968.
- [46] K. Fukui, T. Yonezawa, and H. Shingu, "A Molecular Orbital Theory of Reactivity in Aromatic Hydrocarbons," *Journal of Chemical Physics*, vol. 20, no. 4, pp. 722–725, 1952.
- [47] R. G. Parr and W. Yang, "Density Functional Approach to the Frontier-Electron Theory of Chemical Reactivity," *Journal of the American Chemical Society*, vol. 106, pp. 4049–4050, July 1984.
- [48] P. Thanikaivelan, J. Padmanabhan, V. Subramanian, and T. Ramasami, "Chemical Reactivity and Selectivity Using Fukui Functions: Basis Set and Population Scheme Dependence in the Framework of B3LYP Theory," *Theoretical Chemistry Accounts: Theory, Computation, and Modeling (Theoretica Chimica Acta)*, vol. 107, pp. 326–335, June 2002.
- [49] M. Torrent-Sucarrat, F. De Proft, P. W. Ayers, and P. Geerlings, "On the Applicability of Local Softness and Hardness," *Physical Chemistry Chemical Physics*, vol. 12, no. 5, p. 1072, 2010.
- [50] F. Mendez and J. Gázquez, "Chemical Reactivity of Enolate Ions: the Local Hard and Soft Acids and Bases Principle Viewpoint," *Journal of the American Chemical Society*, vol. 116, no. 20, pp. 9298–9301, 1994.
- [51] P. Mondal, K. K. Hazarika, and R. C. Deka, "Reactivity of α -Unsaturated Carbonyl Compounds Towards Nucleophilic Addition Reaction: a Local Hard–Soft Acid–Base Approach," *PhysChemComm*, vol. 6, pp. 24–27, Mar. 2003.
- [52] P. Pérez, Y. Simón-Manso, A. Aizman, P. Fuentealba, and R. Contreras, "Empirical EnergyDensity Relationships for the Analysis of Substituent Effects in Chemical Reactivity," *J. Am. Chem. Soc.*, vol. 122, pp. 4756–4762, Jan. 2012.
- [53] G. Henkelman, A. Arnaldsson, and H. Jónsson, "A Fast and Robust Algorithm for Bader Decomposition of Charge Density," *Computational Materials Science*, vol. 36, pp. 354–360, June 2006.
- [54] F. De Proft, J. Martin, and P. Geerlings, "Calculation of Molecular Electrostatic Potentials and Fukui Functions Using Density Functional Methods," *Chemical Physics Letters*, vol. 256, no. 4, pp. 400–408, 1996.
- [55] R. S. Mulliken, "A New Electroaffinity Scale; Together with Data on Valence States and on Valence Ionization Potentials and Electron Affinities," *Journal of Chemical Physics*, vol. 2, no. 11, p. 782, 1934.

- [56] M. T. Nguyen, G. Raspoet, L. G. Vanquickenborne, and P. T. Van Duijnen, "How Many Water Molecules Are Actively Involved in the Neutral Hydration of Carbon Dioxide?," *The Journal of Physical Chemistry A*, vol. 101, pp. 7379–7388, Oct. 1997.
- [57] B. Han, C. Zhou, J. Wu, D. J. Tempel, and H. Cheng, "Understanding CO₂ Capture Mechanisms in Aqueous Monoethanolamine via First Principles Simulations," *The Journal of Physical Chemistry Letters*, vol. 2, pp. 522–526, Mar. 2011.
- [58] C. Faurholt, "Etudes sur les solutions aqueuses de carbamates et de carbonates," *J. Chim. Phys.*, no. 22, pp. 1–44, 1925.
- [59] E. F. da Silva and H. F. Svendsen, "Study of the Carbamate Stability of Amines Using ab Initio Methods and Free-Energy Perturbations," *Industrial & Engineering Chemistry Research*, vol. 45, pp. 2497–2504, Apr. 2006.
- [60] Y. H. Jhon, J.-G. Shim, J.-H. Kim, J. H. Lee, K.-R. Jang, and J. Kim, "Nucleophilicity and Accessibility Calculations of Alkanolamines: Applications to Carbon Dioxide Absorption Reactions," *The Journal of Physical Chemistry A*, vol. 114, pp. 12907–12913, Dec. 2010.
- [61] C. F. Alie, *CO₂ Capture With MEA: Integrating the Absorption Process and Steam Cycle of An Existing Coal-fired Power Plant*. PhD thesis, University of Waterloo, 2004.
- [62] S. Freguia, *Modeling of CO₂ removal from flue gases using MEA*. PhD thesis, MS Thesis, The University of Texas Austin, May 2002.
- [63] S. Freguia and G. T. Rochelle, "Modeling of CO₂ Capture by Aqueous Monoethanolamine," *AIChE Journal*, vol. 49, pp. 1676–1686, July 2003.
- [64] M. R. M. Abu-Zahra, L. H. J. Schneiders, J. P. M. Niederer, P. H. M. Feron, and G. F. Versteeg, "CO₂ Capture From Power Plants Part I. a Parametric Study of the Technial Performance Based on Monoethanolamine," *International Journal of Greenhouse Gas Control*, vol. 1, pp. 37–46, Apr. 2007.
- [65] B. Oyekan and G. T. Rochelle, "Alternative Stripper Configurations for CO₂ Capture by Aqueous Amines," *AIChE Journal*, vol. 53, no. 12, pp. 3144–3154, 2007.
- [66] C. Alie, L. Backham, E. Croiset, and P. Douglas, "Simulation of CO₂ capture using MEA scrubbing: a flowsheet decomposition method," *Energy conversion and management*, vol. 46, no. 3, pp. 475–487, 2005.

- [67] H. Chang and C. M. Shih, "Simulation and Optimization for Power Plant Flue Gas CO₂ Absorption-Stripping Systems," *Separation Science and Technology*, vol. 40, pp. 877–909, Mar. 2005.
- [68] N. Dave, T. Do, G. Puxty, R. Rowland, P. H. M. Feron, and M. I. Attalla, "CO₂ Capture by Aqueous Amines and Aqueous Ammonia – A Comparison," *Energy Procedia*, vol. 1, pp. 949–954, Feb. 2009.
- [69] B. A. Oyekan and G. T. Rochelle, "Energy Performance of Stripper Configurations for CO₂ Capture by Aqueous Amines," *Industrial & Engineering Chemistry Research*, vol. 45, pp. 2457–2464, Apr. 2006.
- [70] A. Nuchitprasittichai and S. Cremaschi, "Optimization of CO₂ Capture Process with Aqueous Amines Using Response Surface Methodology," *Computers & Chemical Engineering*, vol. 35, pp. 1521–1531, Aug. 2011.
- [71] A. Chakma, A. K. Mehrotra, and B. Nielsen, "Comparison of Chemical Solvents for Mitigating CO₂ Emissions from Coal-fired Power Plants," *Heat Recovery Systems and CHP*, vol. 15, no. 2, pp. 231–240, 1995.
- [72] J. C. Eslick and D. C. Miller, "A Multi-Objective Analysis for the Retrofit of a Pulverized Coal Power Plant with a CO₂ Capture and Compression Process," *Computers & Chemical Engineering*, vol. 35, no. 8, pp. 1488–1500, 2011.
- [73] Carbon Capture Simulation Initiative, *AspenSinter User Manual*. National Energy Technology Laboratory, 0.2 ed., Nov. 2012.
- [74] *Aspen Plus v7.2*. Cambridge, MA: Aspen Technology Inc., 2010.
- [75] J. Davis and G. Rochelle, "Thermal Degradation of Monoethanolamine at Stripper Conditions," *Energy Procedia*, vol. 1, pp. 327–333, Feb. 2009.
- [76] W. D. Seider, J. D. Seader, D. R. Lewin, and S. Widagdo, *Product and Process Design Principles*. Synthesis, Analysis and Design, Wiley, Dec. 2008.
- [77] modeFRONTIER v4.4.2. Trieste, Italy: ESTECO, 2012.
- [78] J. F. Brennecke and B. E. Gurkan, "Ionic Liquids for CO₂ Capture and Emission Reduction," *The Journal of Physical Chemistry Letters*, vol. 1, pp. 3459–3464, Dec. 2010.
- [79] F. A. Chowdhury, H. Okabe, H. Yamada, M. Onoda, and Y. Fujioka, "Synthesis and selection of hindered new amine absorbents for CO₂ capture," *Energy Procedia*, vol. 4, no. C, pp. 201–208, 2011.
- [80] B. Metz, O. Davidson, H. de Coninck, M. Loos, and L. Meyer, "IPCC Special Report on Carbon Dioxide Capture and Storage," tech. rep., Intergovernmental Panel on Climate Change, Jan. 2005.

- [81] D. Driscoll, B. Morreale, and L. Headley, “NETL Test Protocol—Testing of Hydrogen Separation Membranes,” 2008.
- [82] GLOBAL CCS INSTITUTE, “CO₂ Capture Technologies,” tech. rep., Palo Alto, Jan. 2012.
- [83] M. B. Miller, D. R. Luebke, and R. M. Enick, “CO₂-philic Oligomers as Novel Solvents for CO₂ Absorption,” *Energy & Fuels*, vol. 24, pp. 6214–6219, Nov. 2010.
- [84] M. B. Miller, D.-L. Chen, H.-B. Xie, D. R. Luebke, J. Karl Johnson, and R. M. Enick, “Solubility of CO₂ In CO₂-Philic Oligomers; COSMOtherm Predictions and Experimental Results,” *Fluid Phase Equilibria*, vol. 287, pp. 26–32, Dec. 2009.
- [85] M. B. Miller, D.-L. Chen, D. R. Luebke, J. K. Johnson, and R. M. Enick, “Critical Assessment of CO₂ Solubility in Volatile Solvents at 298.15 K,” *Journal of Chemical & Engineering Data*, vol. 56, pp. 1565–1572, Apr. 2011.
- [86] T. Makino, “In Situ Raman Study of Dissolved Carbon-Dioxide Induced Changes of Imidazolium-Based Ionic Liquids,” *Journal of Physics: Conference Series*, vol. 215, p. 012068, Apr. 2010.
- [87] M. J. Muldoon, S. N. V. K. Aki, J. L. Anderson, J. K. Dixon, and J. F. Brennecke, “Improving Carbon Dioxide Solubility in Ionic Liquids,” *The Journal of Physical Chemistry B*, vol. 111, pp. 9001–9009, Aug. 2007.
- [88] A. L. Revelli, F. Mutelet, and J. N. Jaubert, “High Carbon Dioxide Solubilities in Imidazolium-Based Ionic Liquids and in Poly (Ethylene Glycol) Dimethyl Ether,” *The Journal of Physical Chemistry B*, vol. 114, no. 40, pp. 12908–12913, 2010.
- [89] L. A. Blanchard, D. Hancu, E. J. Beckman, and J. F. Brennecke, “Green Processing Using Ionic Liquids and CO₂,” *Nature*, vol. 399, no. 6731, pp. 28–29, 1999.
- [90] J. L. Anthony, J. L. Anderson, E. J. Maginn, and J. F. Brennecke, “Anion Effects on Gas Solubility in Ionic Liquids,” *The Journal of Physical Chemistry B*, vol. 109, pp. 6366–6374, Apr. 2005.
- [91] D. Camper, P. Scovazzo, C. Koval, and R. Noble, “Gas Solubilities in Room-Temperature Ionic Liquids,” *Industrial & Engineering Chemistry Research*, vol. 43, pp. 3049–3054, June 2004.
- [92] S. N. V. K. Aki, B. R. Mellein, E. M. Saurer, and J. F. Brennecke, “High-pressure Phase Behavior of Carbon Dioxide with Imidazolium-based Ionic Liquids,” *The Journal of Physical Chemistry B*, vol. 108, no. 52, pp. 20355–20365, 2004.

- [93] A. M. Schilderman, S. Raeissi, and C. J. Peters, "Solubility of Carbon Dioxide in the Ionic Liquid 1-Ethyl-3-Methylimidazolium Bis(Trifluoromethylsulfonyl)Imide," *Fluid Phase Equilibria*, vol. 260, pp. 19–22, Oct. 2007.
- [94] J. L. Anderson, J. K. Dixon, and J. F. Brennecke, "Solubility of CO₂, CH₄, C₂H₆, C₂H₄, O₂, and N₂ in 1-Hexyl-3-methylpyridinium Bis(trifluoromethylsulfonyl)imide: Comparison to Other Ionic Liquids," *Accounts of chemical research*, vol. 40, pp. 1208–1216, Nov. 2007.
- [95] C. Cadena, J. L. Anthony, J. K. Shah, T. I. Morrow, J. F. Brennecke, and E. J. Maginn, "Why Is CO₂ So Soluble in Imidazolium-Based Ionic Liquids?," *Journal of the American Chemical Society*, vol. 126, pp. 5300–5308, Apr. 2004.
- [96] M. Hasib-ur Rahman, M. Siaj, and F. Larachi, "Ionic Liquids for CO₂ Capture-Development and Progress," *Chemical Engineering & Processing: Process Intensification*, vol. 49, pp. 313–322, Apr. 2010.
- [97] S. G. Kazarian, B. J. Briscoe, and T. Welton, "Combining Ionic Liquids and Supercritical Fluids: in Situ ATR-IR Study of CO₂ Dissolved in Two Ionic Liquids at High Pressures," *Chemical Communications*, no. 20, pp. 2047–2048, 2000.
- [98] R. Jiménez-Gallegos, L. A. Galicia-Luna, and O. Elizalde-Solis, "Experimental Vapor–Equilibria for the Carbon Dioxide + Octane and Carbon Dioxide + Decane Systems," *Journal of Chemical & Engineering Data*, vol. 51, pp. 1624–1628, Sept. 2006.
- [99] X. Wang, I. Chou, W. Hu, R. C. Burruss, Q. Sun, and Y. Song, "Raman Spectroscopic Measurements of CO₂ Density: Experimental Calibration with High-Pressure Optical Cell (HPOC) and Fused Silica Capillary Capsule (FSCC) with Application to Fluid Inclusion Observations," *Geochimica et Cosmochimica Acta*, vol. 75, no. 14, pp. 4080–4093, 2011.
- [100] N. B. Colthup, L. H. Daly, and S. E. Wiberley, *Introduction to infrared and Raman spectroscopy*. Academic Pr, Aug. 1990.
- [101] M. J. Pelletier, "Quantitative Analysis Using Raman Spectrometry," *Applied Spectroscopy*, vol. 57, no. 1, pp. 20–20, 2003.
- [102] R. McCreery, "McCreery Group — Raman." <http://www.chem.ualberta.ca/~mccreery/index.html>, 2012.
- [103] G. Bondarenko, "The Raman Spectra of Carbon Dioxide at the Fermi Resonance, Under Pressures of 50 and 100 MPa, and at Temperatures of 20–600 °C," *Journal of Applied Spectroscopy*, vol. 45, no. 6, pp. 1285–1287, 1986.

- [104] H. R. Gordon and T. K. McCubbin, "The 2.8-Micron Bands of CO₂," *Journal of Molecular Spectroscopy*, vol. 19, no. 1, pp. 137–154, 1966.
- [105] Y. Garrabos, M. A. Echargui, and F. Marsault-Herail, "Comparison Between the Density Effects on the Levels of the Raman Spectra of the Fermi Resonance Doublet of the ¹²C¹⁶O₂ and ¹³C¹⁶O₂ Molecules," *Journal of Chemical Physics*, vol. 91, no. 10, pp. 5869–5880, 1989.
- [106] M. Besnard, M. I. Cabaço, S. Longelin, T. Tassaing, and Y. Danten, "Raman Investigation of the CO₂ Complex Formation in CO₂-Mixtures," *The Journal of Physical Chemistry A*, vol. 111, pp. 13371–13379, Dec. 2007.
- [107] M. Besnard, M. I. Cabaço, D. Talaga, and Y. Danten, "Raman Spectroscopy and Ab Initio Investigations of Transient Complex Formation in CO₂-Benzene Mixtures," *Journal of Chemical Physics*, vol. 129, no. 22, p. 224511, 2008.
- [108] M. I. Cabaço, Y. Danten, T. Tassaing, S. Longelin, and M. Besnard, "Raman Spectroscopy of CO₂-Acetone and CO₂-Ethanol Complexes," *Chemical Physics Letters*, vol. 413, pp. 258–262, Sept. 2005.
- [109] I. Pasquali, J.-M. Andanson, S. G. Kazarian, and R. Bettini, "Measurement of CO₂ Sorption and PEG 1500 Swelling by ATR-IR Spectroscopy," *The Journal of Supercritical Fluids*, vol. 45, pp. 384–390, July 2008.
- [110] S. G. Kazarian, M. F. Vincent, F. V. Bright, C. L. Liotta, and C. A. Eckert, "Specific Intermolecular Interaction of Carbon Dioxide with Polymers," *J. Am. Chem. Soc.*, vol. 118, no. 7, pp. 1729–1736, 1996.
- [111] S. P. Nalawade, F. Picchioni, J. H. Marsman, and L. P. B. M. Janssen, "The FT-IR Studies of the Interactions of CO₂ and Polymers Having Different Chain Groups," *The Journal of Supercritical Fluids*, vol. 36, pp. 236–244, Jan. 2006.
- [112] K. Machida and T. Miyazawa, "Infrared and Raman Spectra of Polyethyleneglycol Dimethylethers in the Liquid State," *Spectrochimica Acta*, vol. 20, no. 12, pp. 1865–1873, 1964.
- [113] H. Matuoura, K. Fukuhara, and H. Tamaoki, "Raman Spectra of Perdeuterated Ethylene Glycol Dimethyl Ether and Diethylene Glycol Dimethyl Ether and the Molecular Force Field of Oxyethylene Compounds," *Journal of Molecular Structure*, vol. 156, no. 3, pp. 293–301, 1987.
- [114] M. I. Cabaço, M. Besnard, Y. Danten, and J. A. P. Coutinho, "Solubility of CO₂ in 1-Butyl-3-methyl-imidazolium-trifluoro Acetate Ionic Liquid

Studied by Raman Spectroscopy and DFT Investigations,” *The Journal of Physical Chemistry B*, vol. 115, pp. 3538–3550, Apr. 2011.

- [115] M. Castriota, T. Caruso, R. G. Agostino, E. Cazzanelli, W. A. Henderson, and S. Passerini, “Raman Investigation of the Ionic Liquid *N*-Methyl-*N*-Propylpyrrolidinium Bis(Trifluoromethanesulfonyl)Imide and Its Mixture with $\text{LiN}(\text{SO}_2\text{CF}_3)_2$,” *The Journal of Physical Chemistry A*, vol. 109, pp. 92–96, Jan. 2005.
- [116] C. La Lau, “Solvent Effects in Infra-Red Spectra of Some Aromatic Compounds,” *Spectrochimica Acta*, 1959.
- [117] M. G. Giorgini, “Raman noncoincidence effect: A spectroscopic manifestation of the intermolecular vibrational coupling in dipolar molecular liquids,” *Pure and Applied Chemistry*, vol. 76, no. 1, pp. 157–169, 2004.
- [118] W. West and P. Arthur, “The Raman Spectra of Some Simple Molecules in Solution,” *Journal of Chemical Physics*, vol. 5, no. 1, p. 10, 1937.
- [119] J. R. Royer, J. M. DeSimone, and S. A. Khan, “Carbon Dioxide-Induced Swelling of Poly(dimethylsiloxane),” *Macromolecules*, vol. 32, pp. 8965–8973, Dec. 1999.
- [120] T. Singh and A. Kumar, “Static Dielectric Constant of Room Temperature Ionic Liquids: Internal Pressure and Cohesive Energy Density Approach,” *The Journal of Physical Chemistry B*, 2008.
- [121] J. X. Mao, A. S. Lee, J. R. Kitchin, and H. B. Nulwala, “Interactions in 1-Ethyl-3-Methyl Imidazolium Tetracyanoborate Ion Pair: Spectroscopic and Density Functional Study,” *Journal of Molecular Structure*, 2013.
- [122] A. J. Berger, Y. Wang, D. M. Sammeth, I. Itzkan, K. Kneipp, and M. S. Feld, “Aqueous Dissolved Gas Measurements Using Near-Infrared Raman Spectroscopy,” *Applied Spectroscopy*, vol. 49, no. 8, pp. 1164–1169, 1995.
- [123] A. Weber, *Raman Spectroscopy of Gases and Liquids*. Springer Verlag, July 2012.
- [124] P. Mirone, “Solvent Effects on Raman and Infra-Red Intensities in the “Continuous Dielectric” Model,” *Spectrochimica Acta*, vol. 22, no. 11, pp. 1897–1905, 1966.
- [125] G. Eckhardt and W. G. Wagner, “On the Calculation of Absolute Raman Scattering Cross Sections From Raman Scattering Coefficients,” *Journal of Molecular Spectroscopy*, vol. 19, no. 1, pp. 407–411, 1966.

- [126] G. Fini, P. Mirone, and P. Patella, "Solvent Effects on Raman Band Intensities," *Journal of Molecular Spectroscopy*, vol. 28, no. 2, pp. 144–160, 1968.
- [127] W. L. Weng and M. J. Lee, "Vapor-Liquid Equilibrium of the Octane/Carbon Dioxide, Octane/Ethane, and Octane/Ethylene Systems," *Journal of Chemical & Engineering Data*, vol. 37, no. 2, pp. 213–215, 1992.
- [128] H. Buxing, Y. Haike, and H. Riheng, "Solubility of CO₂ In a Mixed Solvent of n-Octane and i-Octane at Elevated Pressures," *Thermochimica Acta*, vol. 169, pp. 217–221, 1990.
- [129] K. Tochigi, T. Namae, T. Suga, H. Matsuda, K. Kurihara, M. C. dos Ramos, and C. McCabe, "Measurement and Prediction of High-Pressure Vapor–Liquid Equilibria for Binary Mixtures of Carbon Dioxide+n-Octane, Methanol, Ethanol, and Perfluorohexane," *The Journal of Supercritical Fluids*, vol. 55, pp. 682–689, Dec. 2010.
- [130] H. H. Reamer and B. H. Sage, "Phase Equilibria in Hydrocarbon Systems. Volumetric and Phase Behavior of the n-Decane-CO₂ System.," *Journal of Chemical & Engineering Data*, vol. 8, no. 4, pp. 508–513, 1963.
- [131] Y. Iwai, N. Hosotani, T. Morotomi, Y. Koga, and Y. Arai, "High-Pressure Vapor-Liquid Equilibria for Carbon Dioxide+ Linalool," *Journal of Chemical & Engineering Data*, vol. 39, no. 4, pp. 900–902, 1994.
- [132] G. F. Chou, R. R. Forbert, and J. M. Prausnitz, "High-Pressure Vapor-Liquid Equilibria for Carbon Dioxide/n-Decane, Carbon Dioxide/Tetralin, and Carbon Dioxide/N-Decane/Tetralin at 71.1 and 104.4. Degree. C," *Journal of Chemical & Engineering Data*, vol. 35, no. 1, pp. 26–29, 1990.
- [133] B. Han, D. Y. Peng, C. T. Fu, and G. Vilcsak, "An Apparatus for Phase Equilibrium Studies of Carbon Dioxide+ Heavy Hydrocarbon Systems," *The Canadian Journal of Chemical Engineering*, vol. 70, no. 6, pp. 1164–1171, 1992.

A Aspen Flow Sheets

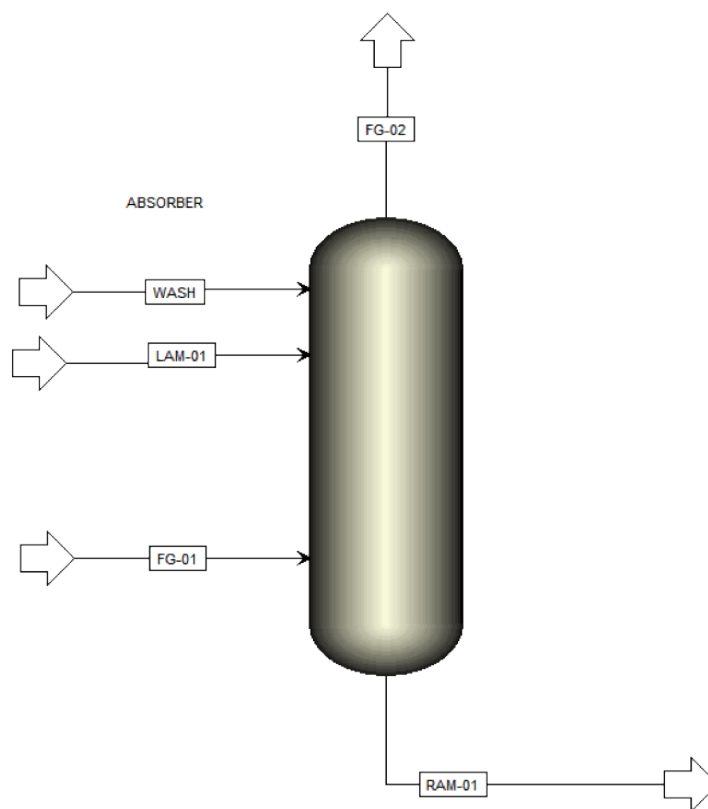


Figure A.1: Aspen flowsheet of post-combustion CO₂ capture absorption tower model.

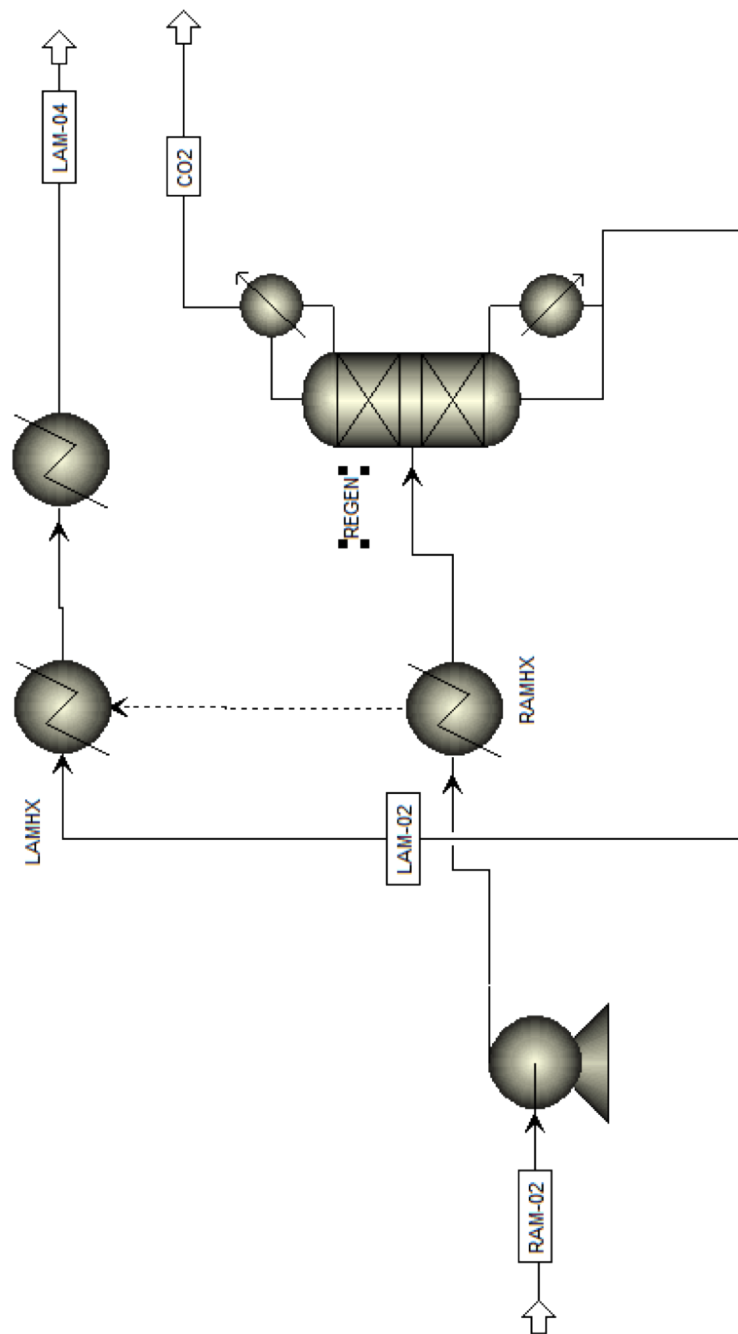


Figure A.2: Aspen flowsheet of post-combustion CO₂ capture amine regeneration tower model.

B Raman Spectra of CO₂-Solvent Systems

B.1 Oligomers

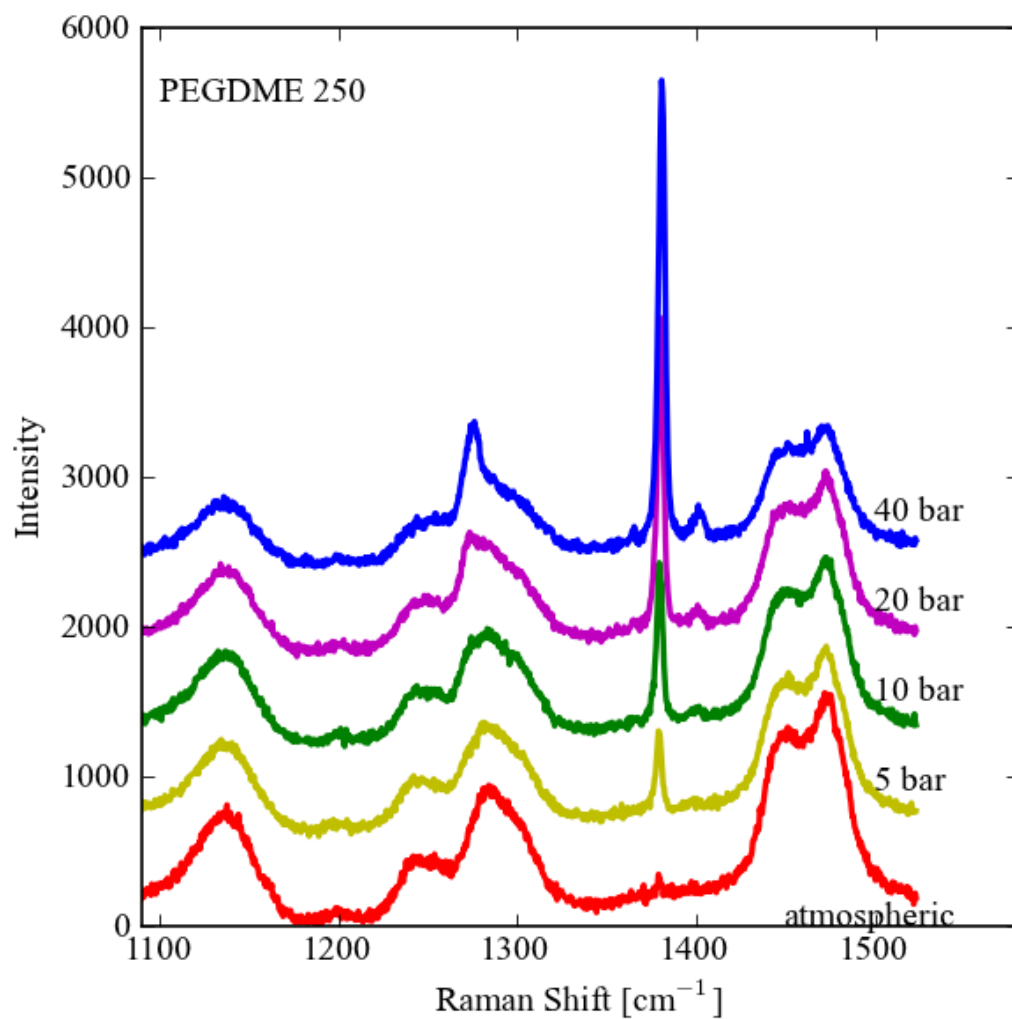


Figure B.1: Raman spectra of PEGDME, MW 250, at atmospheric conditions and equilibrium with 5 to 40 bar CO₂ at 295 K.

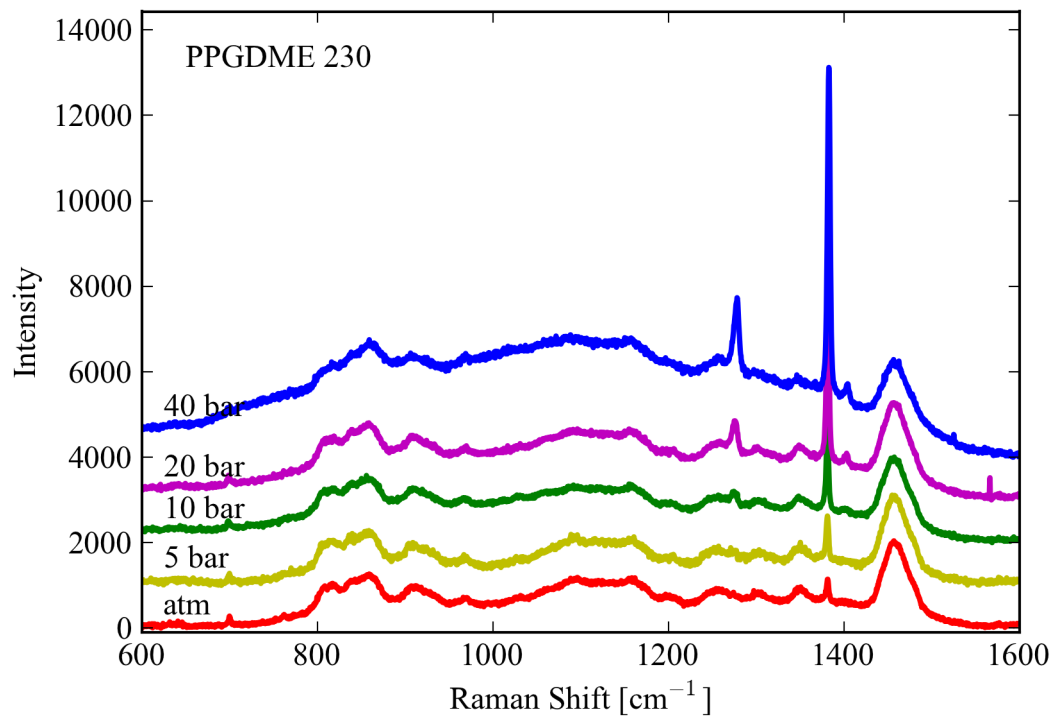


Figure B.2: Raman spectra of PPGDME, MW 230, at atmospheric conditions and equilibrium with 5 to 40 bar CO₂ at 295 K.

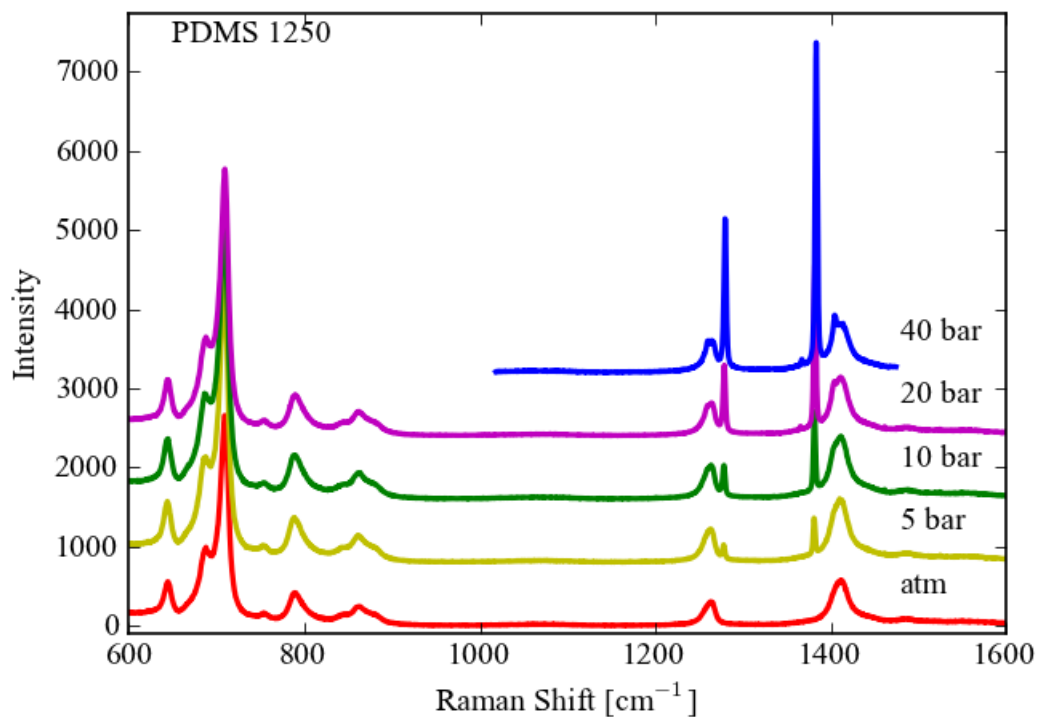


Figure B.3: Raman spectra of PDMS, MW 1250, at atmospheric conditions and equilibrium with 5 to 40 bar CO₂ at 295 K.

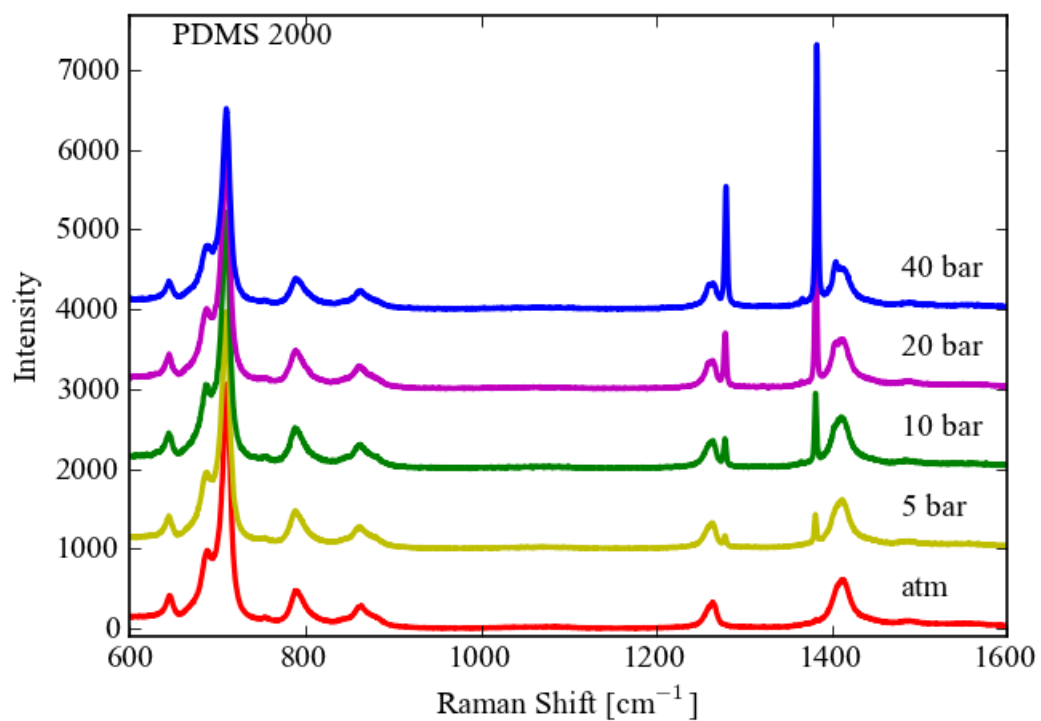


Figure B.4: Raman spectra of PDMS, MW 2000, at atmospheric conditions and equilibrium with 5 to 40 bar CO_2 at 295 K.

B.2 Ionic Liquids

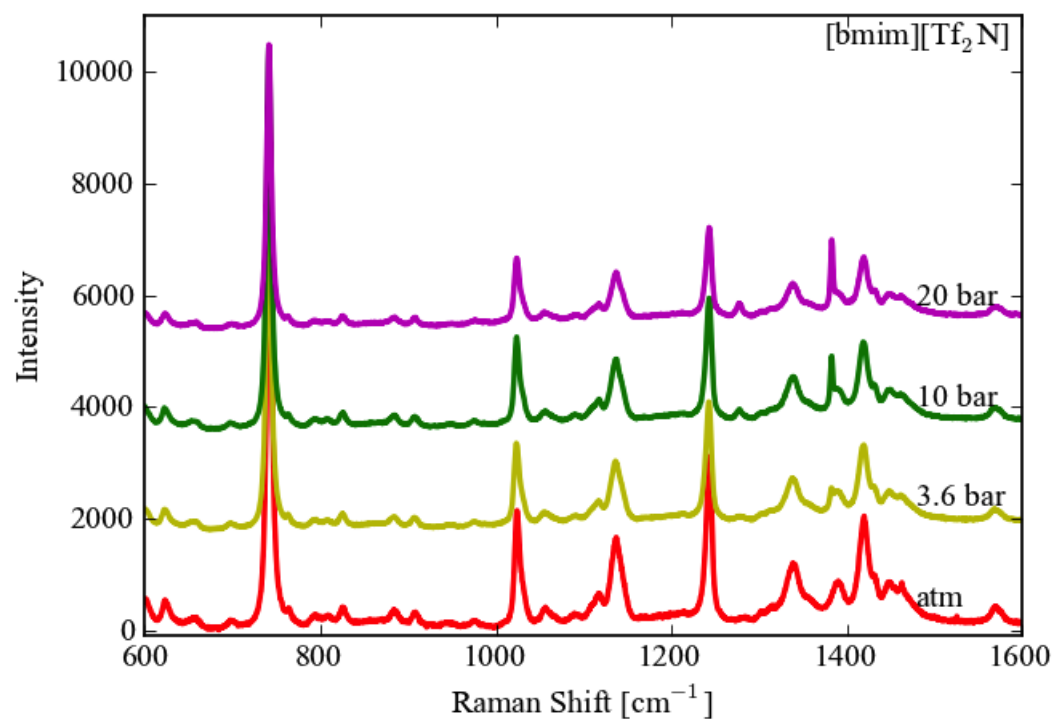


Figure B.5: Raman spectra of [bmim][Tf₂N] at atmospheric conditions and equilibrium with 5 to 40 bar CO₂ at 295 K.

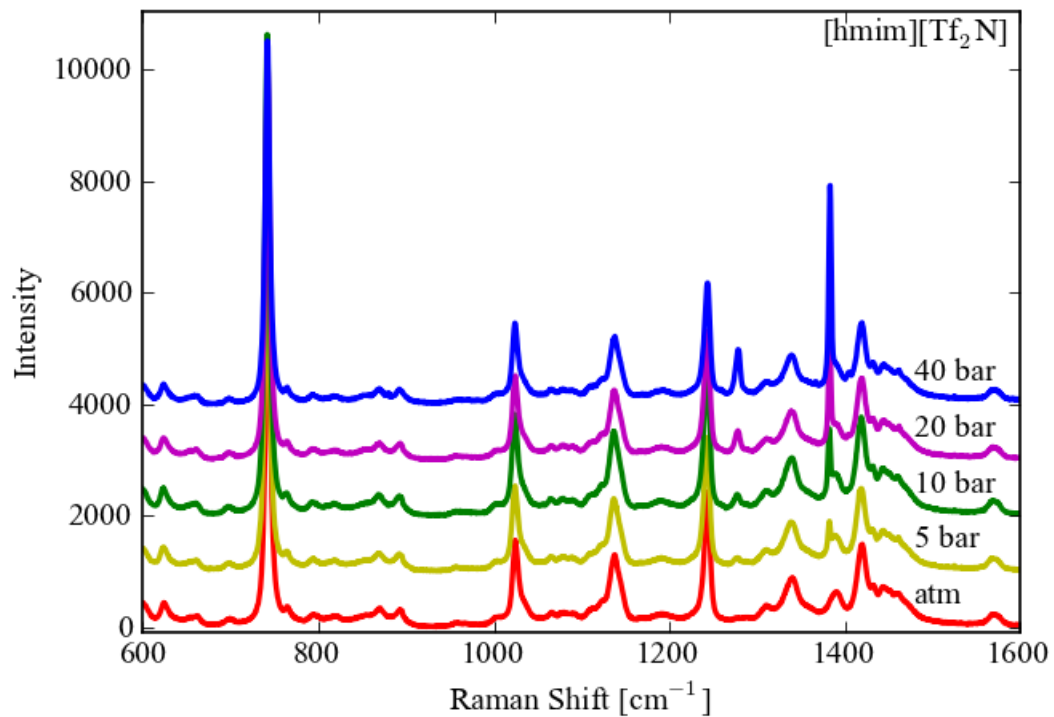


Figure B.6: Raman spectra of [hmim][Tf₂N] at atmospheric conditions and equilibrium with 5 to 40 bar CO₂ at 295 K.

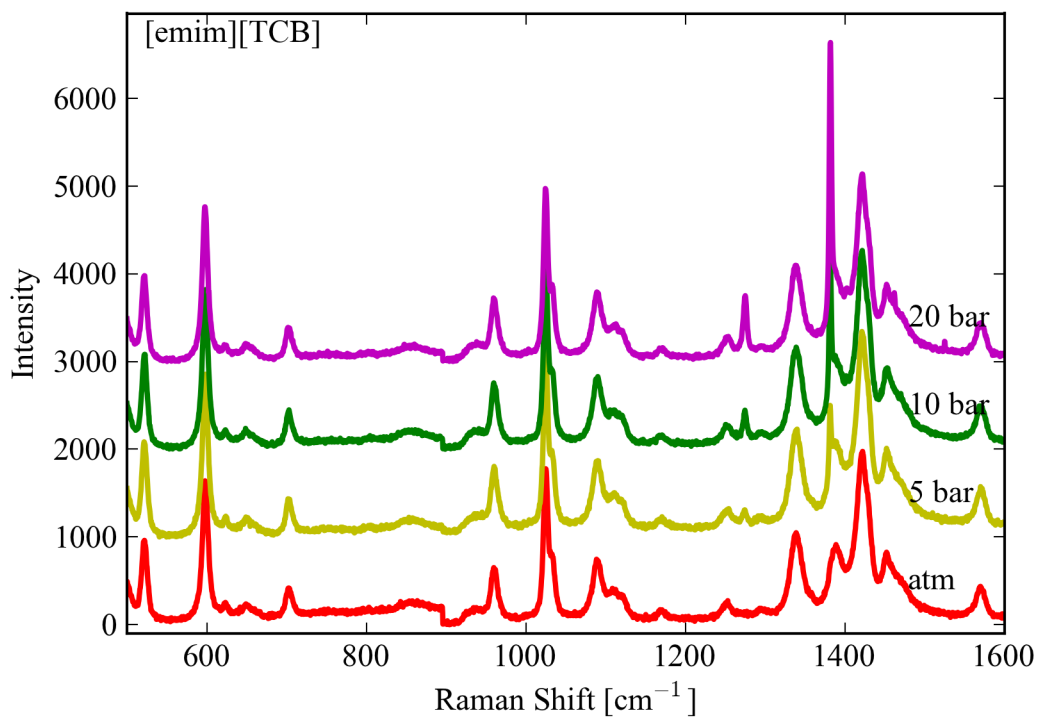


Figure B.7: Raman spectra of [emim][TCB] at atmospheric conditions and equilibrium with 5 to 40 bar CO₂ at 295 K.

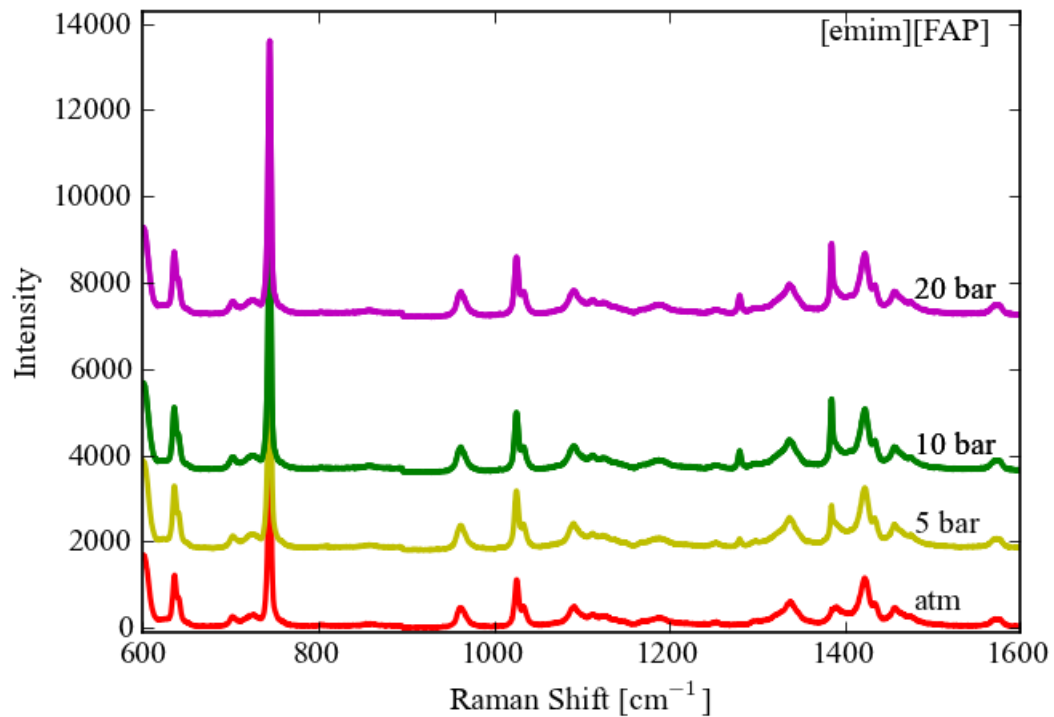


Figure B.8: Raman spectra of [emim][FAP] at atmospheric conditions and equilibrium with 5 to 40 bar CO_2 at 295 K.

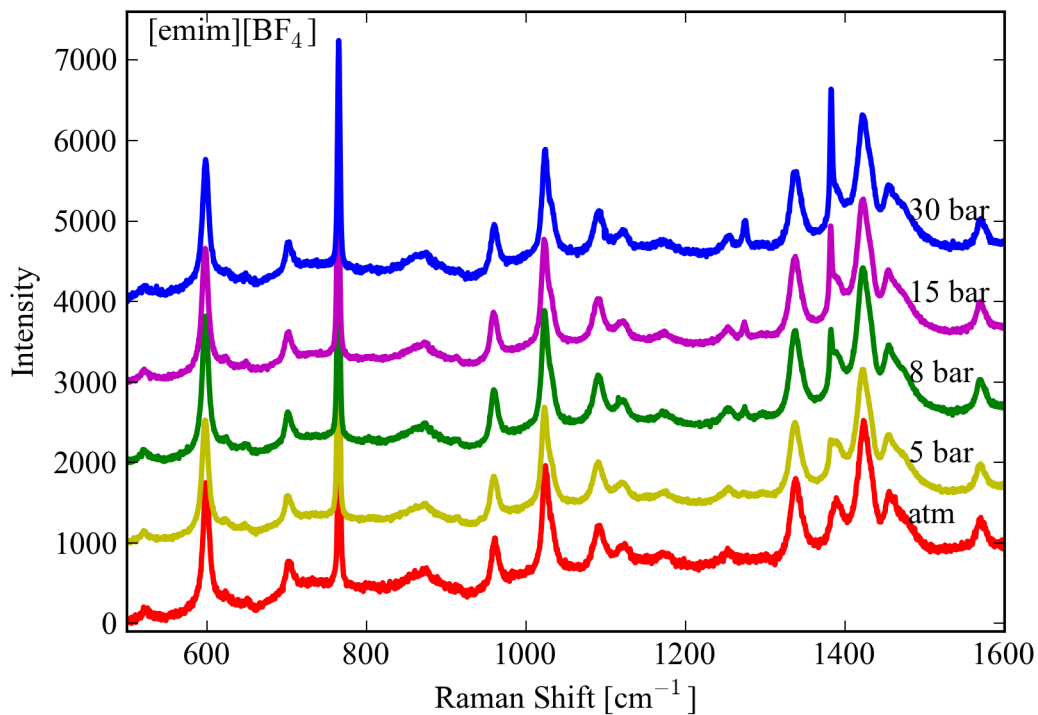


Figure B.9: Raman spectra of [emim][BF₄] at atmospheric conditions and equilibrium with 5 to 40 bar CO_2 at 295 K.